# Time-resolved synchrotron radiation circular dichroism spectroscopy

by

**François Auvray**

Thesis submitted to the University of Nottingham for the Degree of Doctor of Philosophy

School of Chemistry

November, 2019

# Acknowledgements

I would like to thank sincerely my supervisor Professor Jonathan D. Hirst. I am grateful for the support and the countless wise advices he gave me over the past years. His continuous support throughout the writing up of the thesis means a lot for me.

My PhD was based on a partnership with the synchrotron SOLEIL, in France. I would like to give a special thank to Matthieu Réfrégiers, who made this partnership and this PhD project possible. I also would like to thank the team of the DISCO beamline for having welcomed and supported me this way.

I would like to thank Franck Wien for sharing with me all the technical details concerning the SRCD endstation. I am also grateful for his availability over the past years.

I would like to give a special thanks to Frederic Jamme, the person who transmitted to me the passion of the experimental development. I will never forget the inspiring discussions we had in the office.

I would like to thank David Dennetière for being available when I needed to discuss about technical issues. Our fruitful discussions helped me a lot.

I would like to give special thanks to all the students from the university and from SOLEIL with who I spent unforgettable times, Pritesh, Jelena, Suzie, Bebe, Kasia, Ellen, Juliette, Céline, Steve, Adam, Josh and all the others.

My parents and my sisters have supported me a lot throughout my whole life in any circumstance. For that, I will be eternally grateful to all of you.

Only she knows what I felt over the last years because we went through it together. Thank you, Clémence.

# Abstract

Ultraviolet (UV) synchrotron radiation circular dichroism (SRCD) spectroscopy has made an important contribution to the determination and understanding of the structure of bio-molecules. In this thesis work, we demonstrate an innovative approach that we term time-resolved SRCD (tr-SRCD), overcoming limitations of current broadband UV SRCD setups, which could enable access to ultrafast (down to nanoseconds) time scales. The tr-SRCD setup takes advantage of the natural polarisation of the synchrotron radiation emitted by a bending magnet to record broadband UV CD faster than any current SRCD setup, improving the acquisition speed from 10 mHz to 130 Hz and the accessible temporal resolution by several orders of magnitude. I propose several acquisition protocols that use the two different configurations of the the tr-SRCD setup. They would allow one to follow dynamics occurring on a time range spanning from tens of nanoseconds to minutes. I present results on camphorsulfonic acid (CSA) that allowed us to validate our methodology and also to assess the performance of the tr-SRCD setup. I illustrate the potential of the new approach for biological applications by following the concentration changes of isomers of the FK-11-X peptide after photoisomerisation. I point out the limitations of this approach and I propose an alternative method that should limit them. I present the results of our first tests that use this method and we compare them with standard SRCD and tr-SRCD spectra. I dedicate the last part of this thesis to a complementary study of the FK-11-X peptide via the both theoretical and experimental approaches. I present some molecular dynamics simulations and show that using the combination of experimental data acquired with the tr-SRCD setup coupled to first principles calculations of CD could facilitate the determination of transient structures between two stable conformations.

**Publications arising from the thesis work**

Auvray, F., Dennetiere, D., Giuliani, A., Jamme, F., Wien, F., Nay, B., Zirah, S., Polack, F., Menneglier, C., Lagarde, B., Hirst, J. D., Réfrégiers, M. Time resolved transient circular dichroism spectroscopy using synchrotron natural polarization. *Struct. Dynam.* (6), 054307, 2019.

Auvray, F, Hirst J. D. Unfolding dynamics of a photo-switchable helical peptide *J. Phys. Chem. B*, (124), 5380–5392, 2020.

Rogers, D. M., Jasim, S. B., Dyer, N. T., Auvray, F., Réfrégiers, M., Hirst, J. D. Electronic circular dichroism spectroscopy of proteins. *Chem*, (5), 2751–2774, 2019.

# Contents

# List of Figures

# List of Tables

# List of abbreviations

| | |
|---|---|
| AWG | Arbitrary waveform generator |
| CD | Circular dichroism |
| CgenFF | CHARMM General Force Field |
| CMOS | Complementary Metal Oxide Semiconductor |
| CSA | Camphorsulfonic acid |
| DNA | Deoxyribonucleic acid |
| DUV | Deep-ultraviolet |
| FWHM | Full width half maximum |
| IR | Infrared radiation |
| LD | Linear dichroism |
| MCP | Micro-channels plate |
| MD | Molecular dynamics |
| MM | Molecular mechanical |
| ORD | Optical rotatory dispersion |
| PSF | Protein structure file |
| QM | Quantum mechanical |
| QWP | Quarter wave plate |
| RMSD | Root-mean-squared deviation |
| SNR | Signal-to-noise ratio |
| SR | Synchrotron radiation |
| SRCD | synchrotron radiation circular dichroism |
| tr-SRCD | Time-resolved synchrotron radiation circular dichroism |
| TTL | Transistor-transistor logic |
| UV | Ultraviolet |
| VUV | Vacuum-ultraviolet |

# 1 Introduction

## 1.1 Historical context

Optical activity was observed for the first time at the beginning of the 20th century by Francois Arago[1]. He observed that the orientation of the polarisation plane of the light can be affected when the light passes through a quartz crystal. He also noticed that the amplitude of the effect depends on the light wavelength. A few years later, Jean-Baptiste Biot[2][3] made further observations, notably on liquids, and started to formulate the laws behind the physical phenomenon. He established that some materials have the capacity to rotate the polarisation plane of the light passing through them, either right-handed rotation or left-handed rotation. The direction of the rotation is defined by the observer who faces the source of the light. He introduced the terminologies dextrorotatory and levorotatory, respectively, for the substance rotating the plane clockwise and anti-clockwise. He also found that the angle of the rotation is inversely proportional to the square of the wavelength of the light. Finally, he also noticed that the direction of the rotation does not depend of the propagation direction of the light. The notion of circular polarisation arrived in 1822 in a paper published by Augustin Fresnel[4]. He affirmed that the linear polarisation can be decomposed into two circularly polarised waves. He defended his hypothesis by explaining that the orientation of the linear polarisation is correlated to the phase shift between the two circular components. And so, he concluded that if a material changes the orientation of linearly polarised light, it would mean that it has two different refractive indices for right-handed and left-handed circularly polarised light. Thus, this difference induces a phase shift between the two circular components and so changes the polarisation orientation of linearly

polarised light as it goes through the material. In 1895, Aimé Cotton invented the concept of circular dichroism[5]. It was already established that in many crystals, polarised light is split into two beams, the ordinary beam and the extraordinary beam. These two beams propagate through the crystal at different speeds due to the difference of refractive index but they are also absorbed differently. The medium of propagation is said to be dichroic. Cotton made the connection between this phenomenon and the theory of Fresnel and he wondered if, in addition to having different refractive indices for circularly polarised light, optically active substances absorb left and right circularly polarised light differently. He developed an optical bench allowing him to observe simultaneously the transmitted intensity of a light beam split into two identical parts with opposite circular polarisation. He observed that when the beam was absorbed by some optically active substances, the transmitted intensities of the two parts were different. Moreover, he noticed that, in the case of chiral molecules (tartaric acid), this difference was inverted when an enantiomer was replaced by the other. These first experiments showed that the polarisation state can be affected by the structure of matter, and so one can get insights at a molecular scale by studying these interactions. Arago, Fresnel and Cotton paved the way for the development of a multitude of applications still in use today.

## 1.2 Definition of polarisation

Light consists of electromagnetic waves composed of an electric and a magnetic field. Its polarisation corresponds to the orientation of its electric field while it propagates through a medium. The electric field of a monochromatic light wave propagating along the $z$ axis in a Cartesian coordinate system in

an isotropic and homogeneous medium is described by Equation 1.1.

$$E(z,t) = E_0 e^{i(kz-\omega t+\phi)} \tag{1.1}$$

where $E_0$ is the initial wave amplitude, $k$ is the wavenumber, $\omega$ is the angular frequency, $t$ is the time, and $\phi$ the phase at the origin.

The polarisation state and so the orientation of $E$ while it propagates along z is defined by the amplitudes and the phases of its components $E_y$ and $E_x$. These two components are defined, at a fixed position along $z$, by Equations 1.2. The two components $E_x$ and $E_y$ are shown in Figure 1.1.

$$\begin{aligned} E_x(t) &= E_{0_x} e^{i(-\omega t+\phi_x)} \\ E_y(t) &= E_{0_y} e^{i(-\omega t+\phi_y)} \end{aligned} \tag{1.2}$$

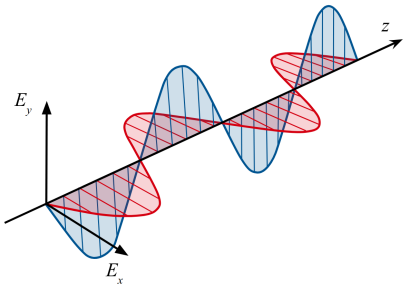


**Figure 1.1:** The two components of the electric field $E_x$ and $E_y$.

This is the relative difference between the phases that induces changes in the state polarisation. The two absolute phases $\phi_x$ and $\phi_y$ in the Equations 1.2 can be replace by the difference $\phi_y - \phi_x$ in one of the two components. Thus, Equation 1.2 may be written:

$$\begin{aligned} E_x(t) &= E_{0_x} e^{i(-\omega t)} \\ E_y(t) &= E_{0_y} e^{i(-\omega t+\phi_y-\phi_x)} \end{aligned} \tag{1.3}$$

The value of this phase difference coupled to the amplitude of the two components will directly determine the state of the light polarisation. The light is either linearly, circularly or elliptically polarised (Figure 1.2 ).

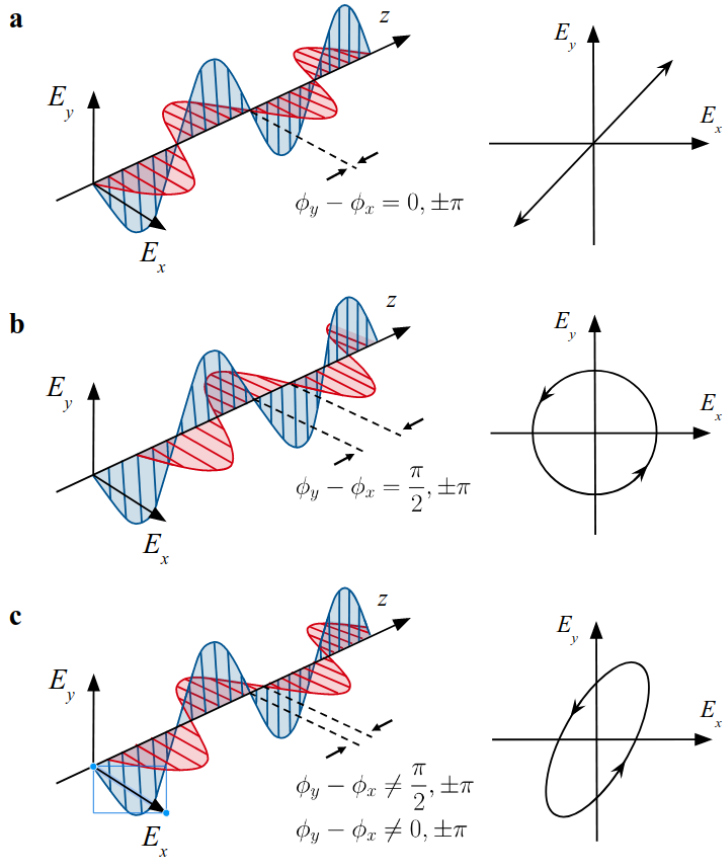


**Figure 1.2:** The components of the electric field for linearly, circularly and elliptically polarised light in Figure 1.2.a, 1.2.b and 1.2.c, respectively.

## 1.3 Polarisation formalisms

The polarisation state has been formalised mathematically using vectors to facilitate its characterisation. In this thesis, I will use the Jones vector formalism to illustrate the principle of the molar ellipticity measurements and the Stokes parameters formalism to characterise the polarisation state of the synchrotron radiation. These two formalisms will be presented in this Section.

### 1.3.1 Jones vector formalism

In 1941, Jones introduced a new formalism to describe the polarisation of a monochromatic light beam completely polarised, the Jones vector[6]. The Jones vector, $J$, is composed of the complex amplitude of the electric field components (Equation 1.4).

$$J = \begin{pmatrix} E_x \\ E_y \end{pmatrix} = \begin{pmatrix} E_{0x} \\ E_{0y} e^{i(\phi_y - \phi_x)} \end{pmatrix} \tag{1.4}$$

The Jones vector is usually normalized to 1. When the phase difference is proportional to $\pi$, $(\phi_y - \phi_x) = k\pi$, where $k$ is a natural number, the light polarisation is linear. The Jones vector $J$ can be written as a function of $\theta$, the angle between the horizontal plane and the vector of the electric field (Equation 1.5).

$$J = \begin{pmatrix} \cos\theta \\ \sin\theta \end{pmatrix} \tag{1.5}$$

In the particular case where $E_x = 0$ or $E_y = 0$, the linearly polarised light is respectively oriented vertically and horizontally. The light is right circularly polarised when $(\phi_y - \phi_x) = \frac{\pi}{2}$ and left circularly when $(\phi_y - \phi_x) = -\frac{\pi}{2}$. The complex amplitude $E_y$ is equal to $-i$ and $i$, when the circular polarisation is right-handed and left-handed, respectively. The Jones vector that describes circularly polarised light is:

$$J = \frac{1}{\sqrt{2}} \begin{pmatrix} 1 \\ \pm i \end{pmatrix} \tag{1.6}$$

This formalism allows us to confirm Fresnel's hypothesis that linearly polarised light can be decomposed into two circularly polarised waves, by

summing the Jones vector of right- (RH) and left-handed (LH) circularly polarised light:

$$RH + LH = \frac{1}{\sqrt{2}} \begin{pmatrix} 1 \\ -i \end{pmatrix} + \frac{1}{\sqrt{2}} \begin{pmatrix} 1 \\ i \end{pmatrix} = \frac{2}{\sqrt{2}} \begin{pmatrix} 1 \\ 0 \end{pmatrix} = H \tag{1.7}$$

This equation shows that superimposing two oppositely circularly polarised light waves having the same amplitude, one obtains a linearly polarised wave oriented along the horizontal plane (Figure 1.3).

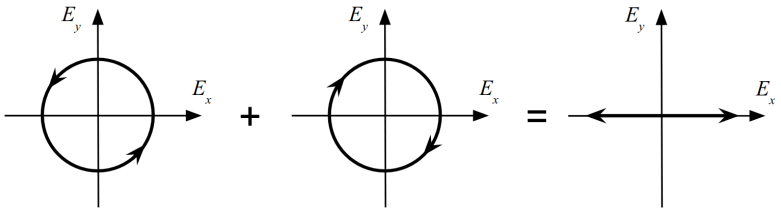


**Figure 1.3:** The sum of two circularly polarised waves having identical amplitudes and opposite rotation direction result in a linearly polarised wave that is oriented along the horizontal plane.

### 1.3.2 Stokes parameter formalism

In 1852, George Gabriel Stokes introduced a new formalism of polarised light using a vector representation [7]. Contrary to the Jones vector formalism, the Stokes parameters allow one to describe the polarisation of a light beam partially polarised. The polarisation state is fully described by the vector $S$ (Equation 1.8).

$$S = \begin{pmatrix} S_0 \\ S_1 \\ S_2 \\ S_3 \end{pmatrix} \tag{1.8}$$

where $S_0$ is the total intensity, $S_1$ is the difference of linear polarisation intensity between $(p)$ and $(s)$ direction, $S_2$ is the difference between linear polarisation intensity at 45° and 135° from $(p)$ and $S_3$ is the intensity difference between left and right circularly polarised light.

The normalised Stokes parameters can be determined with six intensity measurements:

$$\begin{aligned} S_0 &= I_p + I_s = I_{45^\circ} + I_{135^\circ} = I_R + I_L \\ S_1 &= \frac{I_p - I_s}{I_p + I_s} \\ S_2 &= \frac{I_{45^\circ} - I_{135^\circ}}{I_{45^\circ} + I_{135^\circ}} \\ S_3 &= \frac{I_R - I_L}{I_R + I_L} \end{aligned} \tag{1.9}$$

where $I_P$ and $I_S$ are, respectively, the intensity of the light linearly polarised along the horizontal and the vertical plane. $I_{45^\circ}$ and $I_{135^\circ}$ are, respectively, the intensity of the linearly polarised light at 45° and 135° from the horizontal plane. $I_R$ is the intensity of the circularly right polarised light and $I_L$ corresponds to the intensity of the circularly left polarised light.

## 1.4 Circular dichroism measurements

CD manifests as a difference in absorption of left- and right-circularly polarised light. The differential absorption of circularly polarised light induces changes in intensity of circularly polarised light and thus it transforms linearly polarised light into elliptically polarised light. These consequences make possible several ways to measure CD and so several measurable quantities (with different units). We will describe below the two most prominent methods.

### 1.4.1 Molar circular dichroism

By definition, the CD is the difference in absorption of left- and right-circularly polarised light expressed as $\Delta A$ (Equation 1.10), which is unitless.

$$\Delta A = A_L - A_R \tag{1.10}$$

CD can also be related to the molar extinction coefficient by applying Beer's law (Equation 1.11). The resulting quantity is the molar CD (Equation 1.12).

$$A = \epsilon C l \tag{1.11}$$

$$\Delta\epsilon = \frac{1}{Cl}\Delta A \tag{1.12}$$

where $C$ is the concentration of the attenuating species, $l$ is the optical path length and $\epsilon$ is the molar attenuation coefficient.

This difference is the normalised value of the CD and it varies as a function of the wavelength. For historical reasons, the molar ellipticity has preferentially been used by the scientific community.

### 1.4.2 Molar ellipticity

The second method consists of determining the polarisation modification of a linearly polarised beam passed through a dichroic sample. In order to illustrate this phenomenon, it is interesting to refer to the hypothesis proposed by Fresnel[4]. A linearly polarised wave can be seen as the superimposition of two coherent circularly polarised components. However, the amplitudes of the two components must be equal; if they are not, the resulting polarisation will be elliptical. In the case where the light passes through a dichroic sample, the amplitudes of the two components are modified and are different at the output

of the sample. We can determine the polarisation equation of the resulting wave using the Jones formalism (Section 1.3.1). Two opposite circularly polarised waves $E_L$ and $E_R$, respectively left and right-handed, with different amplitudes can be written as:

$$\begin{aligned} E_R &= a \begin{pmatrix} 1 \\ i \end{pmatrix} \\ E_L &= b \begin{pmatrix} 1 \\ -i \end{pmatrix} \end{aligned} \tag{1.13}$$

where $a$ and $b$ are the amplitudes of the two waves and $a \quad b$. By superposing the two waves, we obtain the Jones vector $E$:

$$E = E_R + E_L = \begin{pmatrix} a+b \\ i(a-b) \end{pmatrix} \tag{1.14}$$

Thus, using the Euler's formula, we can write the two complex amplitudes $E_x$ and $E_y$ of $E$:

$$\begin{aligned} E_x &= a + b \\ E_y &= (a-b)e^{t\frac{\pi}{2}} \end{aligned} \tag{1.15}$$

We now restore the propagator in the equation, where $\omega$ is the angular frequency, $k$ the wavenumber, $t$ the time and $z$ the position:

$$\begin{aligned} E_x(z,t) &= (a+b)e^{i(\omega t - kz)} \\ E_y(z,t) &= (a-b)e^{i(\omega t - kz + \frac{\pi}{2})} \end{aligned} \tag{1.16}$$

We now take the real part of $E_x$ and $E_y$:

$$\begin{aligned} E_x(z,t) &= \Re(E_x) = (a+b)\cos(\omega t - kz) \\ E_y(z,t) &= \Re(E_y) = (a-b)\sin(\omega t - kz) \end{aligned} \tag{1.17}$$

Thus, we have:

$$\begin{aligned} \frac{E_x(z,t)}{(a+b)} &= \cos(\omega t - kz) \\ \frac{E_y(z,t)}{(a-b)} &= \sin(\omega t - kz) \end{aligned} \tag{1.18}$$

Then, squaring and summing the two equations we obtain:

$$\frac{E_x^2(z,t)}{(a+b)^2} + \frac{E_y^2(z,t)}{(a-b)^2} = 1 \tag{1.19}$$

This equation is the equation of an ellipse which has $(a+b)$ as major axis length and $(a-b)$ as minor axis length. This demonstration shows that the superposition of two opposite circularly polarised light beams with different amplitudes gives rise to an elliptically polarised light beam. The ellipticity angle $\Psi$ is represented in Figure 1.4.

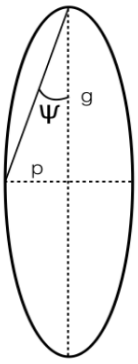


**Figure 1.4:** The minor axis length $p$, the major axis length $g$ and the ellipticity $\Psi$.

In the previous part, we demonstrated that $p = a+b$ and $g = a-b$, where $a$ and $b$ are the amplitude of the two components after the sample. We can

express $\Psi$ as a function of $a$ and $b$:

$$\Psi = \tan(\frac{p}{g}) \approx \frac{p}{g} = \frac{a-b}{a+b} \tag{1.20}$$

We can also write $\Psi$ as a function of the initial amplitude of the two circular components using the Beer-Lambert law:

$$\Psi = \frac{a-b}{a+b} = \frac{A^{-\alpha_l l} - A^{-\alpha_r l}}{A^{-\alpha_l l} + A^{-\alpha_r l}} \tag{1.21}$$

where $A$ is the initial amplitude of the two circularly polarised components, $l$ is the pathlength, $\alpha_l$ and $\alpha_r$ are the absorption coefficient of the left- and right-handed component, respectively.

In addition, $\alpha_{l,d} \ll 1$,we thus obtain:

$$|\Psi| = \frac{|\alpha_l - \alpha_r| l}{4} \tag{1.22}$$

To conclude, the polarisation of linearly polarised light is modified when it passes through a dichroic sample, and the polarisation ends up elliptical. As seen above, the ellipticity of the resulting ellipse is proportional to the difference between the absorption coefficient of left and right-handed circular polarisation and so, to the quantitative value of the CD.

### 1.4.3 Circular dichroism units

As explained previously, there are principally two methods to measure CD. The first is based on the difference of absorption between left- and right-handed circularly polarised light and the second determines CD from the ellipticity of the polarisation of a linearly polarised beam passed through a dichroic sample. Because the two methods determine the CD differently, their units are different.

For the absorption technique, the most used unit is the difference of molar extinction coefficient $\Delta\epsilon$ in $mol^{-1}.L.cm^{-1}$, where $L$ is the unit of volume. The CD is:

$$CD = \Delta\epsilon = \frac{1}{Cl}\Delta A \tag{1.23}$$

The absorption variation $\Delta A$ can be developed using Equation 1.24 to define $\Delta\epsilon$ as a function of the difference $\alpha_l - \alpha_r$ (Equation 1.25).

$$10^{-A} = e^{-\alpha l} \tag{1.24}$$

$$\Delta\epsilon = \frac{1}{\ln(10)C}(\alpha_l - \alpha_r) \tag{1.25}$$

In the second method, the CD corresponds to the molar ellipticity in $deg.mol^{-1}.L.m^{-1}$:

$$CD = [\Psi] = 100\frac{\Psi}{Cl} \tag{1.26}$$

Using Equation 1.25 and Equation 1.26, we can express the molar ellipticity as a function of $\Delta\epsilon$:

$$\begin{aligned} |\Psi| &= \frac{180}{\pi}\frac{(\alpha_l - \alpha_r)l}{4} \\ &= \frac{180}{\pi}\frac{\ln(10)Cl}{4}\Delta\epsilon \\ &\approx 3298\Delta\epsilon \end{aligned} \tag{1.27}$$

This direct relation between the ellipticity $\Psi$ and the difference of molar extinction coefficient $\Delta\epsilon$ allows one to compare measurements made using both techniques.

## 1.5 Introduction to circular dichroism

### 1.5.1 Definition

CD is an optical property of molecules having chiral structure(s) and/or spatially-oriented arrays of chromophores. A chiral molecule is defined as a molecule that cannot be superimposed with its mirror image. The chirality comes from a stereocentre that often corresponds to an asymmetric carbon. CD manifests as a difference in absorption of left- and right-circularly polarised light. At the molecular scale, it means that a molecular electronic transition is more likely to occur depending on the polarisation orientation of the exciting photon. CD is quantified as the difference of the molar extinction coefficient between left- and right circularly polarised light at a given wavelength. Indeed, this difference varies according to the molecular electronic transitions that are induced and so to the energy of the exciting photons. It gives information about the spatial arrangement of the atoms of the molecules, called the absolute configuration, and so it provides information related to their structure.

### 1.5.2 Application of UV circular dichroism

The main use of CD spectroscopy in the UV range is related to protein structure and conformation determination[8,9,10]. Protein secondary structures produce CD peaks in a range spanning from 130 nm to 240 nm. The spectral range accessible with commercial instruments allows one to study the electronic transitions of the amide group. The energy and intensity of these transitions depend of the dihedral angles of the peptide bonds and thus the secondary structure of the protein. In this range, the transitions are the n$\pi^*$ transition (at $\sim$215 nm) and the $\pi\pi^*$ transition (at $\sim$195 nm) in -sheet structures, and the n$\pi^*$ transition (at $\sim$225 nm) and the $\pi\pi^*$ transitions (at $\sim$208 nm and

~190 nm, polarised parallel and perpendicular, respectively, to the helix axis) in -helical structures[11]. The molecular orbitals are shown in Figure 1.5.

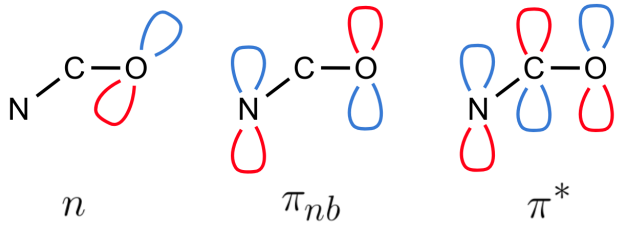


**Figure 1.5:** Scheme of the orbitals of the amide group which are involved in the transition in the 180 nm - 240 nm range. The lone pair on the oxygen atom $n$, the nonbonding orbital $\pi_{nb}$ and the antibonding orbital $\pi^*$.

In the near-UV range (240 - 300 nm), proteins exhibit CD that comes from aromatic chromophores in the protein side chains (tryptophan, phenylalanine and tyrosine)[12,13] (Figure 1.6). These chromophores do not have intrinsic CD individually. However, the location of one or more aromatic amino acids in a chiral environment may induce CD in their $\pi\pi^*$ electronic transitions of their aromatic ring in the near UV region. The CD signal also depend on the distance and the relative angle between these chromophores and thus depend on the protein conformation. It brings supplementary information that can help confirm protein identity and so help to distinguish mutants or mis-folded proteins[14,15].

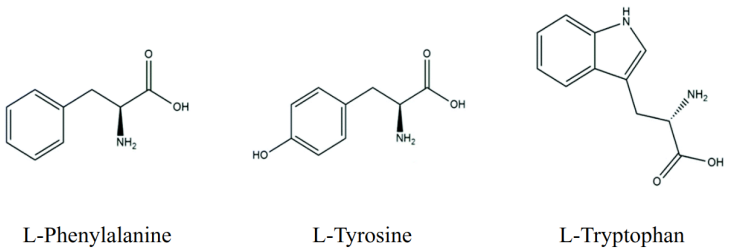


**Figure 1.6:** The three aromatic amino acids: phenylalanine, tyrosine and tryptophan.

UV CD spectroscopy has been exploited for many decades for characterisation of organic molecules and materials with supramolecular chirality, composed by molecules in a non-covalent assembly. It is an important

biophysical tool for characterising native and modified proteins. In the biomedical context, protein misfolding can have dramatic consequences on cell physiology, causing serious neurodegenerative diseases, as found in Alzheimer's and Parkinson's[16]. Structural and kinetics studies of protein folding, using time-resolved approaches, are providing crucial insights at the molecular level into the aetiology of these diseases.

## 1.6 Synchrotron radiation circular dichroism

The light source provided by a beamline in a synchrotron does not have spectral emission limits and can be optimised for any energy range between X-rays and infrared. A beamline optimised in the deep UV (DUV) range is a much brighter continuum light source than a Xenon arc lamp, usually used in conventional CD spectrometer (3 orders of magnitude or more[17]). The high brightness of the synchrotron radiation significantly improves the signal-to-noise ratio (SNR) of the measurements. It broadens the accessible spectral range and also allows the detection of smaller variations in the CD signal. In 1980, Snyder *et al.*[18] and Sutherland *et al.*[19] developed the first CD spectroscopy instruments that use synchrotron radiation. These first setups were built, respectively, in the Synchrotron Radiation Center (SRC), located in Stoughton, Wisconsin and at the SURF II facility at the National Bureau of Standards. They were optimised for the VUV range by using optical components made of magnesium fluoride, adapted mirrors coatings, gratings optimised for this range and the optical benches were vacuum. Snyder *et al.*[18] demonstrated that the use of synchrotron radiation significantly enhances the SNR ratio of the measurement as well as its spectral resolution by comparing CD and SRCD spectra of (+)-3-methylcyclo-pentanone. They used a photo-elastic modulator (PEM) to circularly-polarise the incoming linearly polarised

light. The polarisation varies alternately from circularly right- and circularly left- according to the stretching direction of the crystal of the retarder. The retardation induced by the PEM depends on the strength applied on the crystal. The intensity of the source varies according its polarisation state. Thus, the CD signal is determined from the intensity variation measured with a photomultiplier tube.

Current SRCD experimental stations in synchrotrons around the world still use the same method. The only difference is that Rochon-type polariser made of magnesium fluoride is usually added before the PEM, to polarise almost perfectly linearly the incoming light by separating horizontally and vertically polarised light. This approach gives good results for steady-state studies in which the conformation of the sample remains the same over the measurement. It allows one to obtain an acceptable SNR at a given wavelength by averaging the signal over 2 seconds. However, because the retardation induced by the PEM with a given setting varies according the wavelength, it is necessary to scan the spectral range and adapt the retardation of the modulator to obtain a complete spectrum. Thus, a spectrum from 180 nm to 260 nm with a 1 nm increment is recorded in about 2 minutes. Steady-state SRCD measurements are used in a wide range of applications, such as structure determination[20,21,22,23], the identification of structural changes of protein synthesised with mutated genes[24], study of the impact of the environment on protein structure[25] and the formation of molecular complexes[26].

## 1.7 Time-resolved circular dichroism

Many recent studies focus on system dynamics[27,28,29,30]. The speed of the processes studied generally spans between a few nanoseconds to seconds[31], which is too fast to be followed using conventional CD or standard SRCD. In

this section, we will present the different approaches that have been developed over the last decades to overcome this limitation.

### 1.7.1 Time-resolved circular dichroism

The first time-resolved CD techniques appeared in 1974[32,33]. Feronne *et al.* and Bayley *et al.* recorded, with millisecond temporal resolution, transient CD of photolysis processes in proteins and biomolecular interactions. The UV probe beam was generated by a mercury arc or a Xenon flash lamp, spectrally filtered with an interference filter and polarised alternately circularly left and right (50 kHz) by a quartz modulator. The CD signal was determined from the variation of intensity of the probe beam after passing through the sample. These first monochromatic techniques paved the way for further time-resolved CD spectroscopy developments and allowed the first studies of biomolecular dynamics. The technique was improved to reach 300 $\mu$s temporal resolution and coupled to a T-jump to study the relaxation of protein conformation after an increase in temperature[34]. Akiyama *et al.*[35] coupled a commercial CD spectrometer based on the same principle with a mixing microfluidic cell to obtain CD spectra sequentially with 400 $\mu$s time resolution. A significant enhancement of the time resolution was made in 1989 using a picosecond pulsed laser[36]. The quartz modulator was replaced by a Pockels cell, which circularly polarises the 80 ps pulses of the laser probe. A Pockels cell is a device that induce a tunable retardation using the Pockels effect, which produces birefringence in an optical medium induced by an electric field. The retardation depends on the intensity of the electric field. This novel approach was used to study the photo-dissociation of the CO ligand in carbonmonoxymyoglobin. With this setup, Xie and Simon made a breakthrough in CD spectroscopy by reaching sub-nanosecond temporal resolution but its spectral range was limited to 280 nm in the UV range and its use was limited for biological applications.

Dartigalongue *et al.*[37] improved this approach, enhancing the alignment of the Pockels cell. They also developed a novel technique based on the use of a Babinet–Soleil compensator[38]. This approach significantly enhances the CD measurement, because it removes the bias in the CD measurement arising from polarisation artifacts, and can achieve sub-picosecond temporal resolution. They demonstrated the strength of their method in the DUV range (>225 nm) with the measurement of binaphthol spectra and following the photo-dissociation of carbonmonoxymyoglobin[39].

Kliger's group developed a time-resolved CD setup able to access a spectral range down to 195 nm. It is still today the only setup built with commercial devices that reaches that wavelength. They first proposed a novel method, based on the measure of the ellipticity change of a highly eccentric elliptically polarised light after passing through a chiral sample. They also demonstrated the reliability of this new approach measuring the CD change of the photo-dissociation of the CO ligand in carbonmonoxymyoglobin with a 300 ns time resolution[40]. The method has been extended to higher energy[41] and higher time resolutions (∼10 ns)[42].

### 1.7.2 Broadband time-resolved circular dichroism

There are two main ways to measure CD spectra: the ellipsometric method and the direct absorption difference detection method. The former is based on quantifying the variations of the ellipticity and azimuth orientation of a highly elliptically polarised beam passing through a dichroic sample[41]. In 2012, Eom *et al.*[43] innovatively adapted the ellipsometric method to a heterodyne-detection technique, providing both the CD spectrum and the optical rotation dispersion spectrum, by analysis of the phase and the amplitude of the transmitted orthogonal electric field of the incident light polarisation.

More recently, Hiramatsu *et al.*[44] coupled the heterodyne detection technique to a singular value decomposition analysis. This improvement removes LD and linear birefringence artifacts, allowing accurate time-resolved CD (tr-CD) measurements in the visible range with sub-picosecond temporal resolution. The second way to acquire a CD spectrum is based on absorption difference measurement. The light is alternately right- and left-circularly polarised using an optical modulator. Then the detection system records intensity variations and allows CD determination. This method has been extensively refined, and can provide sub-picosecond resolution for monochromatic measurements. Hache and colleagues used this technique to probe ultra-fast kinetics in biomolecules[45] and achieved 800 fs temporal resolution[46]. Trifonov *et al.*[47] have developed a setup for picosecond transient broadband CD measurements in the visible range. They used a combination of a Pockels cell and a light continuum generator to obtain a pulsed white light source alternately circularly right- and left-polarised. Both ellipsometric and absorption difference broadband techniques have advantages and disadvantages, but they also share the same spectral restriction to the visible range, due to the lack of stable continuum light sources in the UV range. However, Oppermann *et al.*[48] recently proposed a novel approach using a doubled Ti:Sapphire amplifier that emits femtosecond pulsed light between 250 nm and 370 nm. They used a PEM to polarise circularly the broadband source and they demonstrated that the error brought by the wavelength dependence of the device was not significant if the spectral width of the source does not exceed 130 nm.

### 1.7.3 Broadband time-resolved synchrotron radiation circular dichroism

The acquisition duration of a standard SRCD setup precludes time-resolved broadband measurements in sub-second time range. For monochromatic measurement, the theoretical time resolution limitation of these setups is linked to the modulator frequency. This frequency is usually around 50 kHz, so the resolution limitation of monochromatic measurements is about 20 $\mu$s. This temporal resolution corresponds to the duration of one complete stretching time period of the crystal of the PEM. The usual way to follow dynamics with a SRCD setup in a wider spectral range is to use a microfluidic device and adapt the flow of the sample or to shift the probing beam to probe different moment after the reaction trigger[49,50]. However, this approach has some disadvantages. It consumes a lot of sample, it could have significant bias due to the heterogeneity of the sample at the measurement spot and it has a dead time inherent to the stop flow device (typically $\simeq$ 1 ms).

## 1.8 Project presentation

The synchrotron radiation is naturally polarised[51]; the polarisation state of the emitted photons depends on their propagation direction. Photons propagating in the same plane as the orbit of the electrons are linearly polarised, photons located at the edge of the emission cone are circularly polarised and finally photons emitted between these two planes are elliptically polarised. The polarisation ellipticity approaches unity as the angle between the plane of the electron orbit and the light emission direction increases. The polarisation ellipticity also depends on the wavelength of the emitted photons. Moreover, the direction of the polarisation depends on the emission angle; the polarisation is

elliptically right polarised above the plane of the electrons orbit and elliptically left polarised below it. So, the polarisation is not perfectly circularly polarised in the whole synchrotron radiation beam. However, elliptical polarisation can be used to determine CD if the left-handed and right-handed probe beams exhibit the same ellipticity. The only impact of the imperfect circular polarisation will be the decrease of the amplitude of the signal. Another important feature of the synchrotron radiation is its temporal distribution. Electrons are stored in the synchrotron storage ring by bunches. A pulse of light is emitted and collected every time an electron bunch is deviated by the bending magnet of the beamline. The light source provided by a beamline is thus pulsed. The repetition rate and the pulse width of the source depends, respectively, on the number of electron bunches in the storage ring and the bunches length.

The aim of this thesis work is to demonstrate whether one can use the natural polarisation of the synchrotron radiation to measure CD signals and whether it can be used to enhance the temporal resolution of the current SRCD method. The beam provided by the DISCO beamline is a continuum (120 nm to 600 nm) separated in two parts, the upper and the lower parts, which have opposite directions of polarisation. Our approach consists of sending this continuum directly through the sample and then measuring the intensity of the light using a spectrograph. The 2D detector of the spectrograph measures simultaneously the intensity of the probing light from the two oppositely polarised parts of the beam at each wavelength in the whole range of interest. Thus, this setup records the light intensities needed to acquire a CD spectrum in a single measurement. In this thesis, I will present the different aspects of the tr-SRCD setup development, the synchrotron radiation polarisation characterisation, the identification of the artefact sources and some preliminary results. I calibrated and I assessed the performance of the tr-SRCD setup via

measurements of CD spectra of the camphorsulfonic acid (CSA). I recorded photoinduced dynamics of a sample, the FK-11-X peptide[52], which allows me to show the capacity of the setup to record transient spectra of biomolecules. Finally, I recorded spectra of a G-quadruplex structure[53] to compare the reliability of the different approaches that I propose in this thesis.

This novel approach might have great potential for the study of the dynamics of biomolecules or molecules exhibiting CD in the UV spectral range. At SOLEIL, this setup has an ultimate temporal resolution of 82 ps that might give access to ultra-fast dynamics occurring during protein folding and unfolding processes. These dynamics can already be studied with molecular dynamics (MD) simulations. So it could be possible in the future to use experimental data measured with tr-SRCD to assess the reliability of theoretical models. The second part of this thesis is dedicated to the study of the unfolding process of the FK-11-X model via a computational approach. I will present the methodology that I used to develop a force field for the azo-moiety of the FK-11-X peptide. A force field is a set of parameters which is necessary to perform MD simulations. I will present the analysis of 40 trajectories simulating the unfolding process of the FK-11-X peptide within the first 120 ns after its photo-isomerisation. Finally, I will test the reliability of the force field by comparing the rate of the process with experimental data. I will also compare computed CD spectra with experimental SRCD spectra to estimate whether the unfolding process is complete in the simulation.

# 2 Material and Methods

The aim of my work is to demonstrate that the features of synchrotron radiation can be used to acquire time-resolved CD spectra. I tested and optimized different approaches to calibrate the features of the beam provided by the DISCO beamline and to process data from measurements. I will first present the synchrotron SOLEIL, the DISCO beamline and the tr-SRCD setup. Then, I will describe the techniques I have used in this work and how I adapted existing methods to make them applicable to this innovative approach. Finally, I will summarise the technical advantages of the method we propose and its limitations.

## 2.1 Technical information

### 2.1.1 The synchrotron SOLEIL

The synchrotron SOLEIL is a facility dedicated to the worldwide research community. SOLEIL is a third generation synchrotron that was inaugurated on 18th December 2006. SOLEIL hosts 29 beamlines (Figure 2.1) which provide light sources having their own specific features (spectral range, intensity, coherence, spatial distribution, etc).

Synchrotron radiation principles are based on phenomena described in the Maxwell-Lorentz electromagnetic theory. The theory shows that a charged particle, such as an electron or an ion, moving in a non-uniform way at a relativistic speed in a magnetic field emits a radiation called synchrotron radiation. This radiation has an exceptional brightness (high photon flux, low divergence) and has a spectral range spanning from the far-infrared region (1 mm $\geq \lambda \geq$ 15 $\mu$m) to hard X-rays (0.1 nm $\geq \lambda \geq$ 0.01 nm). At SOLEIL,

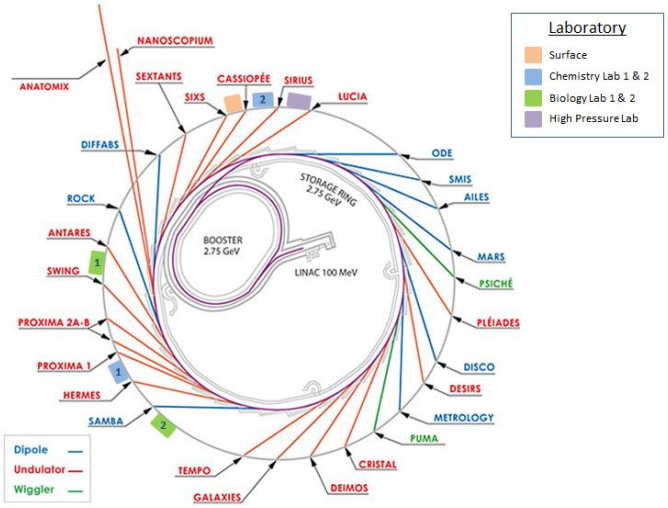


**Figure 2.1:** The synchrotron SOLEIL beamlines (source: www.synchrotron-soleil.fr).

electrons are emitted by an electron gun and accelerated to reach a speed close to the speed of light, so called relativistic speed. They are first accelerated by a LINAC (Linear particle Accelerator) over approximately 10 metres and then they enter in a booster, where they will be continuously accelerated to reach the relativistic speed. Finally, the relativistic electrons are injected and stored in the storage ring (Figure 2.1). The storage ring of SOLEIL is 354 metres long. The electrons are stored in the storage ring by bunches. The three running modes of the synchrotron I used in this project were the uniform mode, the hybrid mode and the 8 bunch mode. In the uniform mode, the storage ring is filled by 416 electrons bunches of 47 ps width and spaced 2.8 ns apart. In the hybrid mode, three quarters of the storage ring are filled the same way as in the uniform mode and there is only one isolated bunch in the empty quarter spaced 148 ns apart from other bunches. In the 8 bunch mode, the storage ring is filled by 8 bunches of 82 ps width spaced 148 ns apart. I will present the purposes of the use of these three modes in Section 2.2.1. Electromagnets and undulators are located around the storage ring. They cause the electron beam to deviate and so trigger the synchrotron radiation emission.

### 2.1.2 The DISCO beamline

The DISCO beamline was inaugurated in 2009[54]. It is optimised for the DUV region. It provides a continuum light source spanning from 60 nm to 700 nm. There are three working stations in the beamline: a SRCD platform[55], a microscopy platform[56] that uses the UV to excite aromatic amino acids and a mass spectroscopy platform[57] that uses the SR as an ionising source. The available spectral range varies according the workstation. At the SRCD endstation the range spans between 120 nm and 650 nm. The DISCO beamline is coupled with a bending magnet that only triggers the synchrotron radiation emission while an electron bunch passes through its magnetic field. It means that the temporal distribution and the pulse width of the source depends, respectively, on the distribution of the electrons bunches and their width. For example, in the 8 bunch mode, the repetition rate of the source is 6.75 MHz and its pulse width is 82 ps. The high energies are cut by a cooled spatial filter at the beginning of the beamline which removes the central part of the beam representing 99.15% of the emitted energy. Thus the available source is composed of two separated beams which are above and below the plane of the accelerated electron orbit in the synchrotron storage ring. The two parts are elliptically polarised. The degree of circular polarisation varies according the angle between the horizontal plane and the light direction. The degree of circular polarisation increases when this angle increases[51,58].

### 2.1.3 The tr-SRCD setup

The tr-SRCD setup[i] is annexed to the existing SRCD endstation. Its optical layout is shown Figure 2.2. The spectral range of the incoming light

[i]Auvray, F.; Dennetiere, D.; Giuliani, A.; Jamme, F.; Wien, F.; Nay, B.; Zirah, S.; Polack, F.; Menneglier, C.; Lagarde, B.; Hirst, J. D.; Réfrégiers, M. Time resolved transient circular dichroism spectroscopy using synchrotron natural polarization. *Struct. Dynam.* (6):054307, 2019.

is selected by the monochromator of the beamline. We can either orient the grating to collect its zero order and thus obtain the complete broadband source provided by the beamline or filter spatially a small part of its first order to select a specific wavelength. The broadband source is used for the tr-SRCD measurement and the monochromatic source is used for the wavelength calibration. When I started this project, another version of the setup was already developed and available. It was composed of the spectrograph (M5, M6, S2, M7 and the grating in Figure 2.2), an intensifier (LAVISION) and a different camera (SHIMADZU). The sample was located in a box, located between S1 and M1. Even if this setup allowed one to record images of the beam projection, the specification (pixels well depth, noise level, dynamic range) of the camera were not sufficient to hope to be able to measure a CD signal. Thus, this configuration of the tr-SRCD was not working at this point. I contributed to its enhancement through the change of the detection chain (detailed below), the modification of the localisation of the sample and the spot size of the probing beam. I also placed all the components on an optical table dedicated to this experimental setup, which brought the flexibility necessary to assess the efficiency of different approaches and also allowed me to easily implement different types of laser to trigger reactions. The beam is

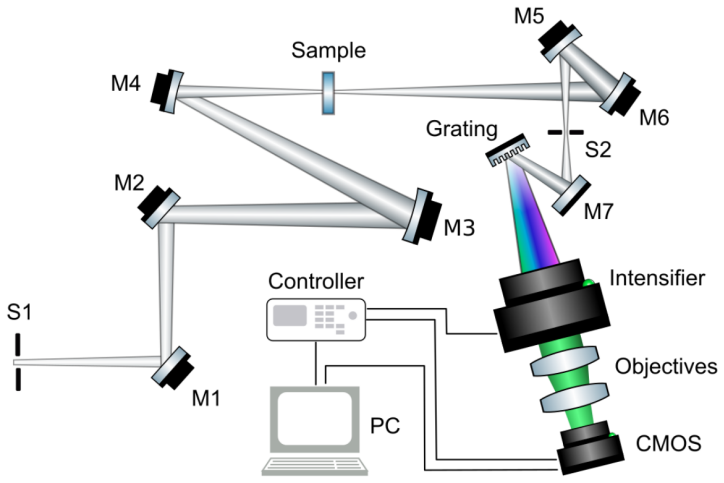


**Figure 2.2:** Optical layout of the tr-SRCD setup.

first spatially defined by a spatial filter (labelled S1 in the figure), then centred by the two plane mirrors (M1, M2) before being refocused on the sample. This optical system was designed to allow variation of the illuminated area on the sample in order to limit, if necessary, damages from beam irradiation. The spherical mirror M3 and the cylindrical mirror M4 refocused the beam 2975 mm after the monochromator slits; the calculated beam diameter at the focal plane is about 300 $\mu$m (FWHM). By moving the sample cell by 200 mm along the optical axis, we get a controllable probe beam diameter from 300 $\mu$m up to 3 mm. Adjustment of the beam diameter to the exposure time helps to minimize the sample irradiation dose. Beyond the sample, the cylindrical mirror M5 and the spherical mirror M6 horizontally focused the beam on a secondary slit (S2). This secondary slit at 3900 mm is used to define the final spectral resolution of the setup. The flat M7 mirror reflected the beam on a spherical flat field grating with 580 grooves per mm (HORIBA JOBIN-YVON) that diffracts and focuses the incident UV/vis light horizontally onto the 2D detector. An image of the projection of the beam is shown in Figure 2.3. I tested two different

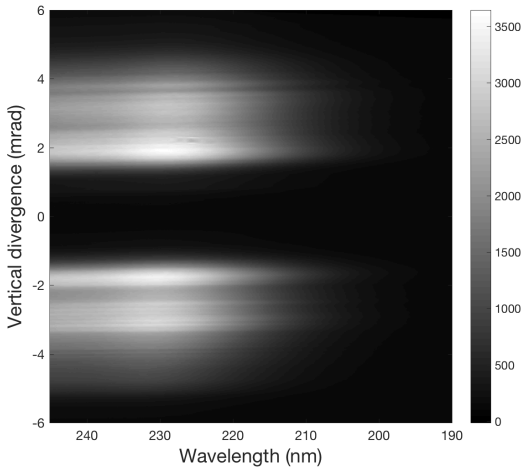


**Figure 2.3:** Image of the projected synchrotron radiation white beam recorded with the CMOS. The grayscale (12 bits) corresponds to the intensity of the light.

complementary configurations for the detection chain. In the first configuration,

I use a sCMOS detector (Prime 95-B, PHOTOMETRICS) that is built with a back illuminated chip. The back illumination technology emerged a few years ago and it significantly improves the sensitivity of the detectors in the DUV range. This new type of detector allowed me to directly detect the light in the whole range of interest of this project. However, the electronic shutter of the camera only allows one to decrease the exposure time down to 40 $\mu$s. I previously said (Section 2.1.2) that the repetition rate of the SR at DISCO depends of the running mode of the synchrotron. The lowest repetition rate of the source is provided by the single bunch mode. In this mode, two pulses are spaced 1.15 $\mu$s apart. Thus, the Prime 95-B does not allow single pulse measurements and so the temporal resolution of the tr-SRCD setup with this detector is limited to 40 $\mu$s. For the applications that need higher temporal resolution, a combination of an image intensifier and a camera can be used. The tr-SRCD setup is equipped with an HS-IRO (LAVISION) coupled to an ORCA-Flash4.0 V3 (HAMAMATSU) using a combination of two 50 mm focal length infinity corrected objectives. This intensifier has three roles: it detects the light with a photocathode (S20), amplifies the signal with a micro-channels plate (MCP) and finally emits a monochromatic version of the incoming image with a phosphor surface. The different stages of the device are shown in Figure 2.4.

Despite the lower sensitivity of the S20 photocathode compared to the PRIME 95-B chip, the intensifier has advantages. The MCP stage significantly amplifies the number of electrons generated by the photocathode (up to a factor of 10000 for the HS-IRO model) so the lack of sensitivity is compensated through this process. This amplification is turned on when a voltage of $Vk = 200V$ is applied on the photocathode and the potential of the MCP-in fixed. These amplification periods are called gates. The electrons are accelerated between the photocathode and the MCP and produce secondary

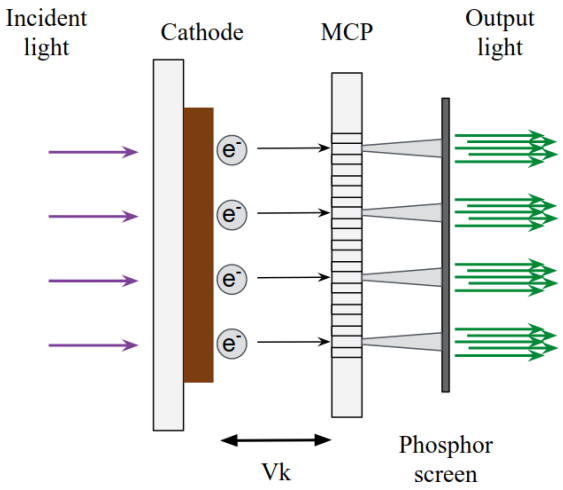


**Figure 2.4:** Scheme of the image intensifier operation principle. The device is made of three parts, the photocathode, the micro-channel plate (MCP) and the phosphor screen. The photocathode detects the incident light, the MCP amplifies the electrons generated by the photocathode and the phosphor screen emits the amplified image. $Vk$ corresponds to the voltage between the cathode and the MCP

electrons at the input surface of the MCP. These electrons are multiplied when passing through the MCP channels, and finally, they hit the phosphor screen, generating an amplified image of the incident light. The amplification gates are monitored by a signal generator, which produces short pulses. The length of these pulses depends on the model of the image intensifier. The shortest accessible gate is 100 ns for the HS-IRO model but some models (Quantum Leap E, STANFORD COMPUTER OPTICS) can amplify the light in only 200 ps. The image emitted by the phosphor screen is then recorded by the CMOS camera. This gated detection allows the CMOS camera to measure the intensity of the incoming light during an extremely brief period of time, much shorter than its minimum integration time. The shortest detection gate of the image intensifier is 100 ns. So we can detect and amplify the light from only one pulse in the single bunch and the 8 bunch mode. The temporal resolution of the measurement corresponds then to the width of the light pulse, which is 82 ps in these modes. Thus, the use of the temporal distribution of the SR might allow one to study sub-microsecond dynamics using the tr-SRCD setup.

The acquisition protocols that can be used for the two configurations will be described in Section 2.2.1.

## 2.2 Method

### 2.2.1 Acquisition protocols

The tr-SRCD setup has been developed to follow dynamics of bio-molecules. Depending on the system, their kinetics occur in a range from tens of nanoseconds to hours. In order to cover this wide range, I developed two setup configurations running with different detection chains. The slowest motions can be discerned using the Prime 95-B which has a minimum integration time of 40 $\mu$s and a repetition rate that can be set up to 300 Hz. Using an adapted protocol, this detector allows one to probe dynamics occurring in a range between tens of microseconds to hours. The fastest dynamics can be studied using the configuration that is based on the combination of the ORCA-Flash4.0 V3 and the HS-IRO image intensifier. The adapted protocols are described in the next sections.

#### 2.2.1.1 Real time acquisition protocol

The first approach consists of measuring in real time the intensity of the probe beam and so recording all the spectra over an unique reaction triggered by an external device. This protocol is limited by the acquisition speed of the camera, so there is no motivation for using the intensifier for this approach. The maximal repetition rate of the PRIME camera (300 Hz) allows one to measure one spectrum every 3.3 ms. If we consider arbitrarily that we need about 10 measurements to describe the features of the dynamics adequately, it means that we can use the real time acquisition protocol to follow dynamics on a timescale of 33 ms or longer. The temporal resolution

of each measurement depends of the integration time, which can be set as short as 40 $\mu$s. In the case of the studies presented in this thesis work, I adjusted this value to accumulate enough light to fill the pixel wells and so maximise the signal-to-noise ratio (SNR) of the measurement. The acquisition timing is managed by an external arbitrary waveform generator (AWG). The device generates transistor-transistor logic (TTL) signals with specific phases, which trigger the camera recording and the other electronic parts of the setup. For real time acquisition, the AWG first triggers the device used to induce a variation in the sample structure and then manages the detector with a periodic TTL signal (Figure 2.5).

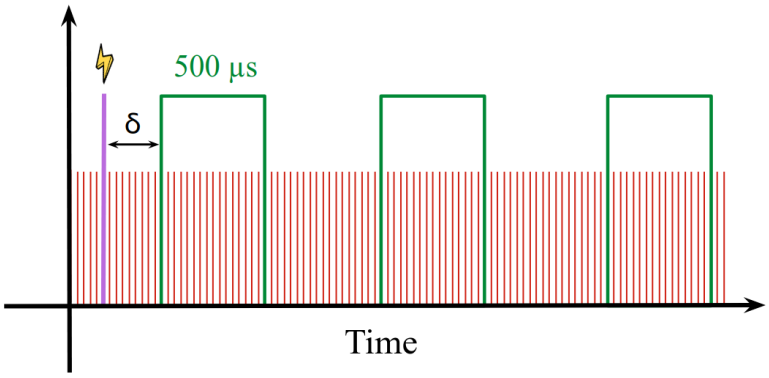


**Figure 2.5:** Sequence diagram of a real time acquisition acquired at 300 Hz with an integration period of 500 $\mu$s (green). In this example, the reaction catalyst (purple) is triggered first and a delay $\delta$ is set before the first recorded frame of the camera.

Depending of the requirements of the experiment, the triggering order of the camera and the reaction catalyst can be changed and the delay between the two signals can also be adapted. However, if one need to increase the sampling of the acquisition, a different protocol must be used to reduce the delay of 3.3 ms between two measurements. This sequential protocol is described in the next section.

#### 2.2.1.2 Sequential acquisition protocols

The sequential acquisition approach can be used for both the configuration with the PRIME to enhance the sampling capability and the configuration with the combination of the ORCA-Flash4.0 V3 and the image intensifier to probe ultrafast dynamics with sub-nanosecond temporal resolution. The reaction is repeated several times with a different delay between the reaction trigger and the measurement. The dynamics are reconstituted through post-processing. The following paragraphs explain this approach in detail and highlight the differences if it is used with only a camera or with the image intensifier.

##### 2.2.1.2.a PRIME configuration

The sequential acquisition protocol using the PRIME camera aims to remove the sampling limitation arising from the pixel readout time of the detector. Previously, we noted that the real time protocol cannot probe efficiently dynamics faster than 33 ms, because of the delay between two recorded frames. The idea of this protocol is to repeat the acquisition but with different delays to cover the time period with desired sampling. In the example shown in Figure 2.6, we increase the sampling of a 10 ms dynamics by a factor of three and so we reach the ten measurements necessary to describe the kinetics adequately. The acquisition is repeated three times with different delays ($\delta_1 = 0$ ms, $\delta_2 = 1.1$ ms, $\delta_3 = 2.2$ ms).

Thus, following this protocol, we are able to probe and study fast dynamics which are not attainable with the frame rate of the detector. The disadvantage of this approach is that we must refresh the sample for each acquisition. So the sample consumption is higher than the real time protocol. However, some biological systems reactions are reversible. So it is possible to perform all the required acquisitions using only one sample loading.

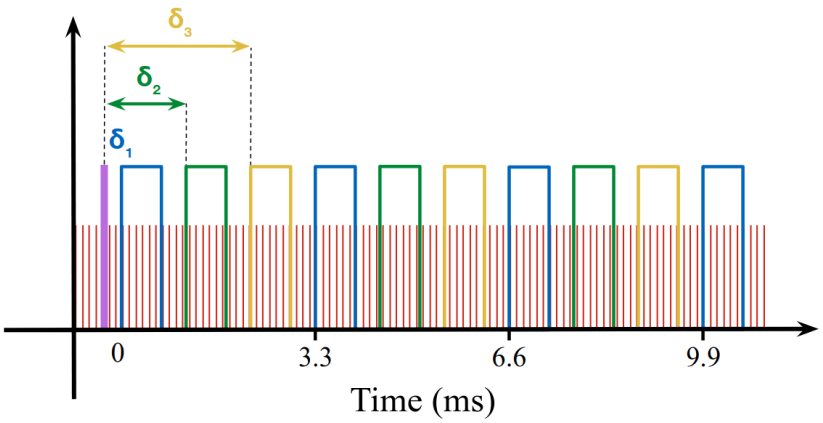


**Figure 2.6:** Sequence diagram of an acquisition using the sequential protocol acquired at 300 Hz. In this example, the reaction catalyst (purple) is triggered first and three separated acquisitions are performed, with three different delays: $\delta_1 = 0$ ms (blue), $\delta_2 = 1.1$ ms (green) and $\delta_3 = 2.2$ ms (yellow).

#### 2.2.1.2.b ORCA + image intensifier configuration

In the previous section, I have shown that we can overcome the sampling of a study through temporally shifted acquisitions. I will now show that we can also avoid the temporal resolution limitation of the CMOS detector by adding an image intensifier to the detection chain. In this configuration, the camera integrates a longer period of time than the length of intensifier gate but it only measures light arising from one intensifying gate. This combination might give access to faster dynamics even in the uniform mode of the synchrotron. The adapted approach consists of progressively increasing the delay $\delta$ between the reaction trigger and the detection gate for each sequential acquisition. This delay can be tuned using the controller of the image intensifier. Then, the dynamics can be constructed with post processing. A diagram of this protocol using this configuration is shown in Figure 2.7. I previously said (Section 2.1.3) that the detection gate length can be reduced to 100 ns, so keeping a sampling at 10 measurements. This approach might allow one to probe faster reactions, down to 1 $\mu$s.

As I have shown previously, the intensifier allows me to measure only one

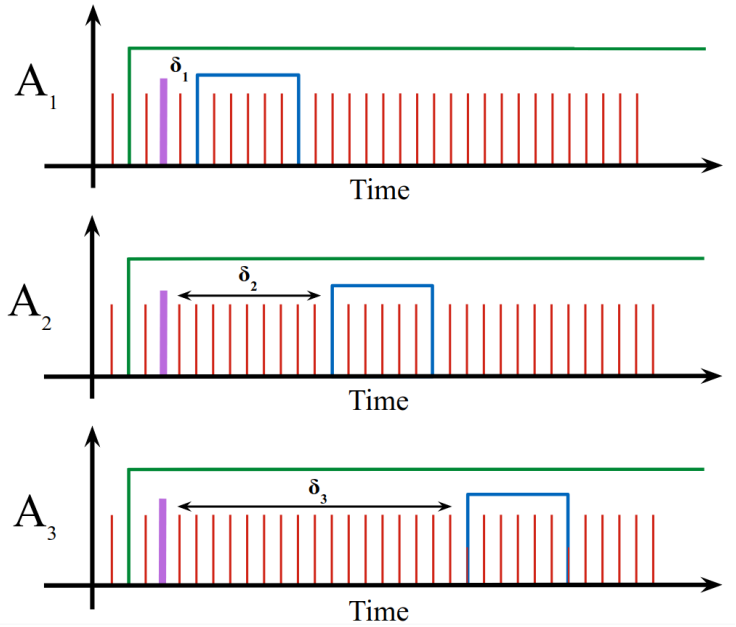


**Figure 2.7:** Sequence diagram of the acquisition protocol using the combination of the image intensifier and a CMOS. The dynamics are probed sequentially, through separated acquisitions (A1, A2, A3,...). The reaction trigger (purple) is synchronised with the camera and the detection gate (blue) of the image intensifier is progressively delayed according the acquisition number. The CMOS (green) integrates one or several detection gates.

pulse of the SR in the hybrid mode, the 8 bunch mode and the single bunch mode. However, the repetition rate of the source in these modes are above 800 kHz, so the camera is not fast enough to record all the detection gates. Moreover, because of the low number of photons in one pulse, it is necessary to integrate several gates to obtain an acceptable SNR in the frame measured by the CMOS. Thus, the use of a sequential protocol is mandatory, for both the SNR and the dynamics reconstruction. This protocol differs from the one previously presented. In this case, the detection and the trigger device must be synchronised with the synchrotron clock. I would have access to two options to shift the delay between the pulses and the trigger. I could use the intensifier controller and an AWG, that allow one to delay the detection gate and the trigger from the synchrotron clock and/or an optical delay line for smaller time steps, down to 0.67 fs (*e.g* ODL600 Thorlabs). A diagram of this protocol is shown in Figure 2.8.

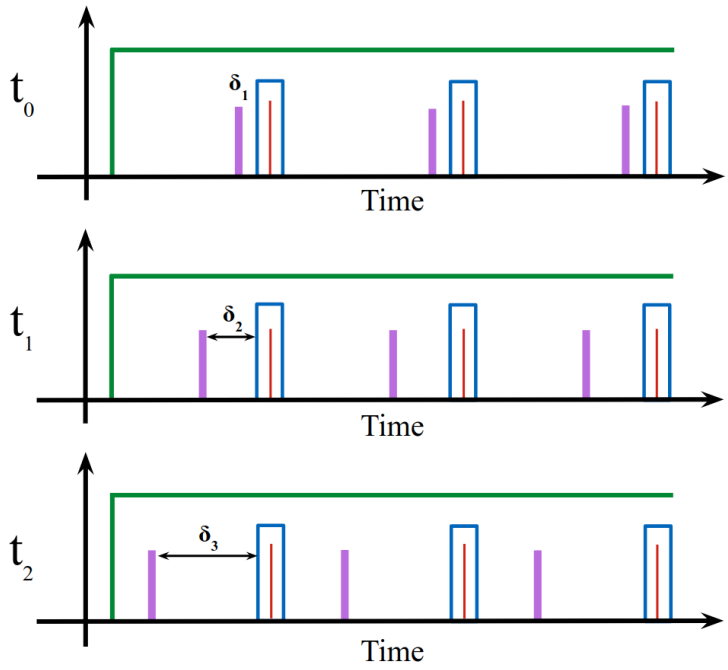


**Figure 2.8:** Sequence diagram of an acquisition protocol using the combination of the image intensifier and a CMOS. The dynamics are probed sequentially, through separated acquisitions ($t_0$, $t_1$, $t_2$,...). The detection gate (blue) of the image intensifier is synchronised with the synchrotron radiation pulses (red). The reaction trigger (purple) is progressively delayed from the measured pulse according the acquisition number. The CMOS (green) integrates several detection gates

The different approaches described in this chapter show that we can cover a wide range of dynamics spanning from nanoseconds to hours. However, the configuration of the setup must be adapted for each protocol and the format of the generated data set changes as well. The sample loading method must be also adapted and globally. The higher the temporal resolution is, the greater the amount of sample required. The duration of the acquisition set will also vary according the protocol that is used. It is faster for lower temporal resolutions. The duration of the acquisitions, which use sequential protocols directly, depends on the repetition rate of the reaction trigger and the dead time of the sample refresh.

### 2.2.2 Polarisation characterisation

As explained above, an asymmetry in the probe polarisation state can cause significant artifacts in the CD measurement. In this setup, the polarisation state of the beam cannot be tuned and adapted. So I must characterise it along the vertical and horizontal axes of the detector to select pixels which will reduce the impact of the artifacts. In chapter 1, I presented the Stokes parameters formalism that is used to describe the polarisation state of the light. I explained that the parameters can be determined using six intensity measurements. I made these measurements using the polarimetry setups shown in Figure 2.9.

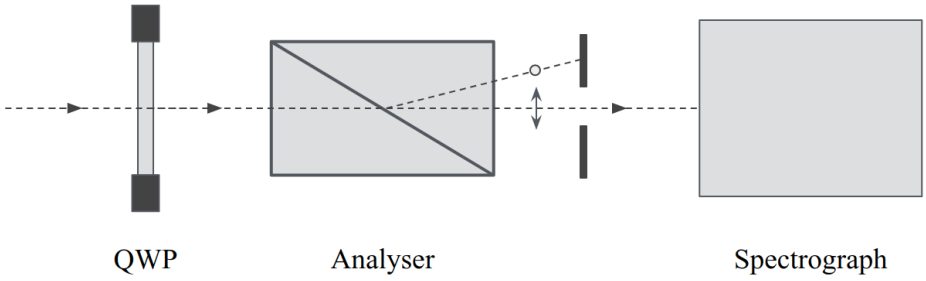


**Figure 2.9:** Polarimetry setup composed by a quarter wave plate (Bernhard Halle) and a Rochon polariser (Bernhard Halle). The extraordinary ray outgoing from the polariser is blocked by a diaphragm.

The six intensity measurements are made with different orientations of the two polarising components. $\alpha$ is the angle of the quarter wave plate (QWP) and $\phi$ is the angle of the polariser (Equation 2.1).

$$
\begin{aligned}
S_0 &= I_{\phi=0^\circ} + I_{\phi=90^\circ} = I_{\phi=45^\circ} + I_{\phi=135^\circ} = I_{\phi=0^\circ,\alpha=45^\circ} + I_{\phi=0^\circ,\alpha=135^\circ} \\
S_1 &= \frac{I_{\phi=0^\circ} - I_{\phi=90^\circ}}{I_{\phi=0^\circ} + I_{\phi=90^\circ}} \\
S_2 &= \frac{I_{\phi=45^\circ} - I_{\phi=135^\circ}}{I_{\phi=45^\circ} + I_{\phi=135^\circ}} \\
S_3 &= \frac{I_{\phi=0^\circ,\alpha=45^\circ} - I_{\phi=0^\circ,\alpha=135^\circ}}{I_{\phi=0^\circ,\alpha=45^\circ} + I_{\phi=0^\circ,\alpha=135^\circ}}
\end{aligned}
\tag{2.1}
$$

The determination of S1 and S2 require the intensity measurement of the component oriented in four specific directions (0°, 45°, 90°, 135°) analysing the light with the polariser. For the S3 parameter, I measure the intensity of the circularly polarised light by converting it to linear with the QWP and analysing it with the polariser. The QWP is only necessary for the measurements of S3 and was removed for the other measurements.

A polarisation state can be plotted in three-dimensional spherical coordinates, *i.e.*, it can be represented on the surface of the Poincaré sphere (Figure 2.10). A point located at the poles ($S_3 = \pm 1$) corresponds to a circularly polarised light; a point located on the equatorial plane corresponds to linearly polarised light. The rest are elliptically polarised with different azimuth orientation angles. Equation 2.2 describes the three Stokes parameters as a function of the spherical coordinates.

$$\begin{aligned} S_1 &= \cos 2\psi \cos 2\chi \\ S_2 &= \sin 2\psi \cos 2\chi \\ S_3 &= \sin 2\chi \end{aligned} \tag{2.2}$$

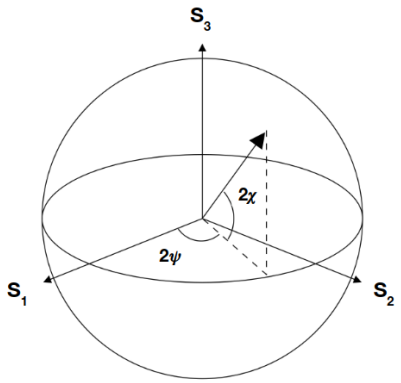


**Figure 2.10:** Poincaré sphere allows one to represent all the polarisation states in a three dimensional space.

This Poincaré sphere allows one to visualise the Stokes parameters of the measured light at each wavelength and so obtain an overview of the polarisation

distribution of the probe beam. We use this polarimetry measurement to select pixel clusters for each wavelength having a similar polarisation state for both parts of the beam. As explained previously, elliptical polarisation can bring two types of artifact in CD measurements. One comes from the circularity of the polarisation and the other from the orientation of the ellipse azimuth. If the two parts of the probing beam have a similar degree of circular polarisation, the artifact effect is limited to the amplitude of the signal. However, if there is a difference in the circularity rate of the two parts of the beam, then more complicated artifacts might arise. In addition, a difference between the angle of the ellipse azimuths of the upper and lower beams might involve a convolution of the CD measurement by a linear dichroism measurement. Thus, during the selection of pixel clusters, I focused on keeping the difference between the azimuth orientation and the absolute $S_3$ of the two parts of the beam value as small as possible.

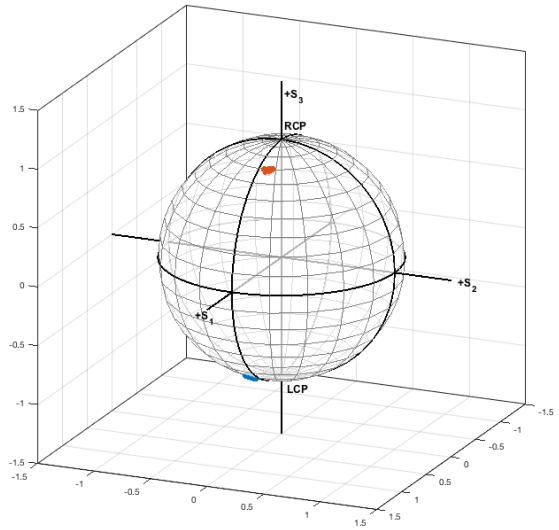


**Figure 2.11:** The polarisation state of the upper beam (red) and of the lower beam (blue) plotted on a Poincaré sphere. Each point corresponds to one cluster containing pixels measuring light at the same wavelength. The $S_3$ values of all the clusters are approximately equal to 0.8 and -0.8, respectively for the upper and the lower beam. We also note that the orientation of the azimuth is close to 0° for all the pixel clusters.

The data plotted on the Poincaré sphere shown in Figure 2.11 corresponds to the polarisation state of the pixel clusters we keep for CD measurements. It shows that the orientation of the azimuth of the light polarisation is similar at each wavelength; it is close to 0°. The $S_3$ value is around 0.8 and -0.8 for the clusters from the upper and the lower beam, respectively. The opposite signs of the $S_3$ values show that the orientation of the elliptical polarisation is opposite for the two parts of the beam, elliptically right for the upper beam and elliptically left for the lower part.

In order to select the clusters, I applied a mask created "by hand" on the data to minimise the average difference of the $S_3$ value of the two parts of the beam. The plots of the absolute $S_3$ values and their differences as a function of the wavelength are shown in Figure 2.12a and Figure 2.12b. The $S_3$ value varies over the spectral range. It ranges between 0.81 and 0.90 and the relative $S_3$ difference between the two parts of the beam is kept below approximately 1. In parallel, the pixel selection also minimises the average difference between the azimuth of the polarisation ellipse of the two parts of the beam. The absolute angles of the azimuths and their absolute differences in the range of interest are shown, respectively, in Figure 2.12c and Figure 2.12d. The angle of the azimuth remains below 7° and the relative difference is kept below 2.5°.

This process allows me to obtain an average difference over the spectral range of $\Delta S_3 \approx 0.0022$ for the $S_3$ absolute values and an average difference $\Delta\beta \approx 0.8571°$ for the orientation of the azimuths. This calibration limits, as much as possible, the sources of artifacts from both the difference of circularity and the difference orientation of the azimuth between the two parts of the beam. Only the ellipticity of the probes may change the measured CD, reducing the amplitude of the signal, but this effect can be easily anticipated and corrected if necessary.

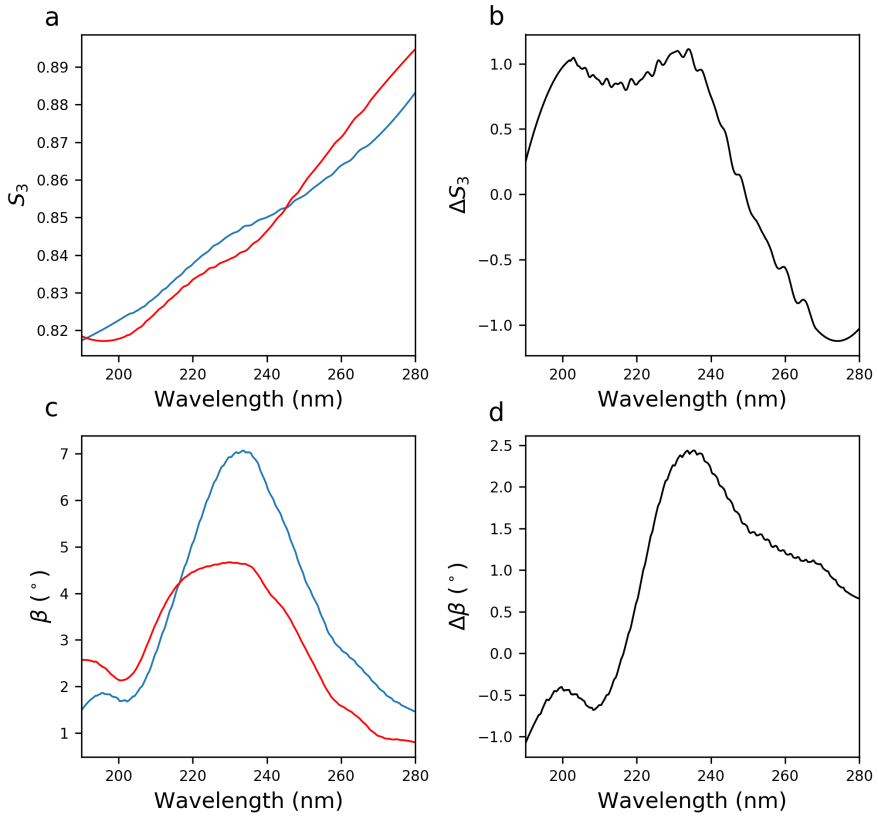


**Figure 2.12: a.** $S_3$ absolute value of the upper (red) and lower (blue) selected clusters as a function of the wavelength.**b.** Relative difference between the absolute $S_3$ values of the cluster from the upper and the lower parts of the beam. **c.** Azimuth orientation angle ($\beta$) of the upper (red) and lower (blue) selected clusters as a function of the wavelength. **d.** Relative difference between the azimuth orientation angle ($\beta$) values of the cluster from the upper and the lower parts of the beam.

### 2.2.3 Spectral calibration

I used the beamline monochromator to obtain a spectrally tunable monochromatic beam in order to perform the spectral calibration. I recorded an image for nine given wavelengths, from 190 nm to 270 nm with a 10 nm step. The concatenation of the nine normalized images is shown in Figure 2.13a. The high energies are on the right side of the image. We can observe that the rays are slightly tilted, i.e, they are not perfectly parallel with the vertical axis of the image. For the CD determination, I will compare the absorbance of the upper beam to the absorbance of the lower beam, for each wavelength. This

comparison would be facilitated if a given wavelength would correspond to the same column of pixels for both the two parts of the beam. In order to visualize this misalignment, I can plot the normalised intensity profile of the two parts of the beam at a given wavelength. The intensity profile of 60 pixels of the two parts of the beam, centered on the 250 nm ray, are represented in the Figure 2.13b.

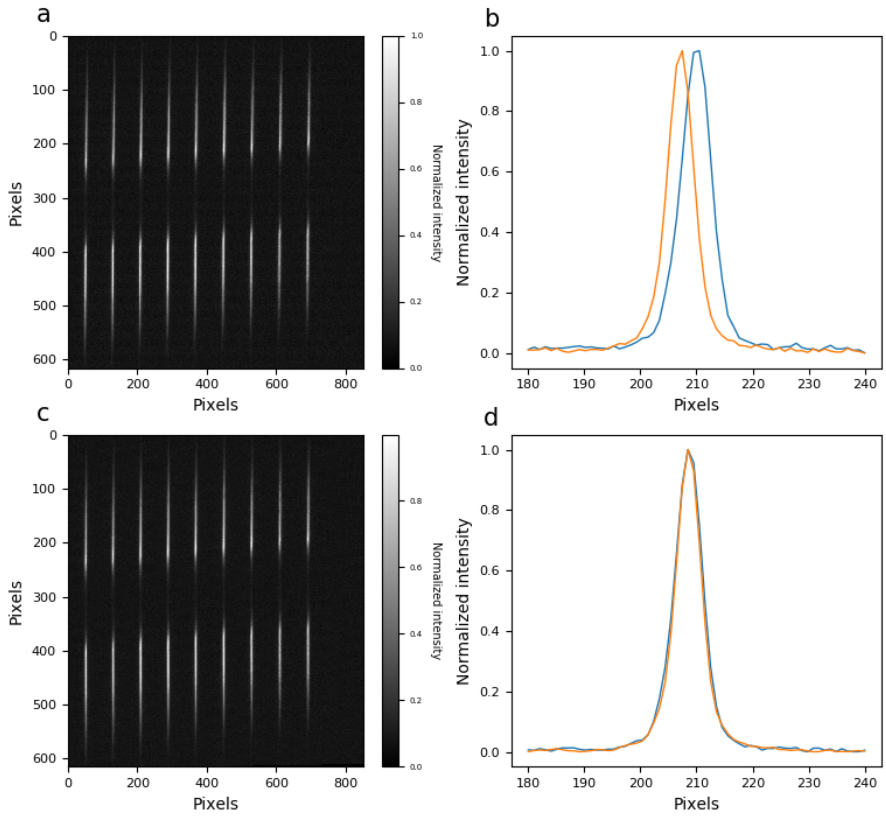


**Figure 2.13: a.** Spectral rays of the SR from 190 nm (right) to 270 nm (left), with a 10 nm step. The grayscale of the image corresponds to the normalised intensity. **b.** Normalised intensity profile of the lower (red) and the upper (blue) parts of the beam calculated from the image a. **c.** Image of the spectral rays rotated by 0.6° clockwise. **d.** Normalised intensity profile calculated from the image c.

The amplitudes correspond to the normalised sum of the pixels intensity of the rows from 0 to 315 for the upper part and from 315 to 615 for the lower part. This representation allows me to estimate the shift in the wavelength induced by the the small tilt in the imaging grating projection. The shift of three pixels corresponds to a wavelength mismatch of less than 0.5 nm, but it

is significant for determining a signal as small as CD.

In order to correct it, I rotate all the recorded images by 0.6° clockwise. The corrected image is shown in Figure 2.13c and the corresponding intensity profiles are plotted in Figure 2.13d. We can see that the rotation of the image completely corrects the shift between the upper and the lower parts and so all the pixels in a column correspond exactly to the same wavelength. I use then an intensity profile of the corrected image to attribute a wavelength to each column of the camera array by using a linear interpolation between two extremum values attributed to the first and the last column.

The plot in Figure 2.14 represents the horizontal intensity profile of the image as a function of the calculated spectral scale. It shows that a linear interpolation is suitable for the spectral calibration. All the vertical dashed lines match correctly with the peak of the corresponding spectral ray.

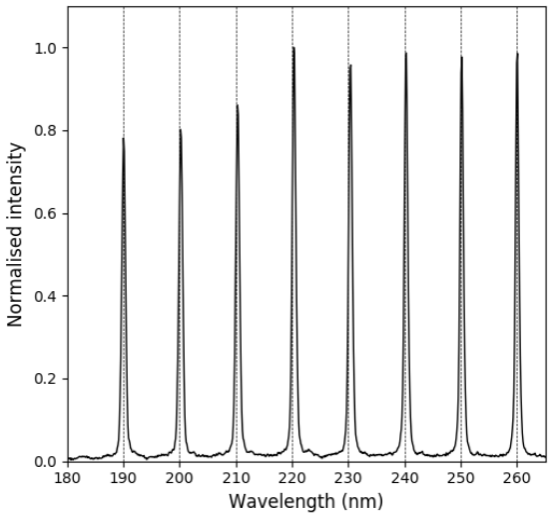


**Figure 2.14:** Horizontal normalised intensity profile of the image used for wavelength calibration. The intensity is plotted as a function of the calculated spectral scale. Vertical dashed line are plotted every 10 nm.

### 2.2.4 Spectrograph resolving power determination

The capacity of a spectrograph to separate wavelengths is called the resolving power. It is denoted $R$ and is related to the spectral resolution $\Delta\lambda$ and the wavelength $\lambda$ (Equation 2.3).

$$R = \frac{\lambda}{\Delta\lambda} \tag{2.3}$$

In order to measure the resolving power of the spectrograph at 250 nm, I estimated its spectral resolution at this wavelength using the monochromatic intensity measurements. The spectral resolution is defined by the full width half maximum (FWHM) of the monochromatic ray profile. The measurement (Figure 2.15) shows a spectral resolution of 0.66 nm at 250 nm and the resolving power at this wavelength is $\approx 379$.

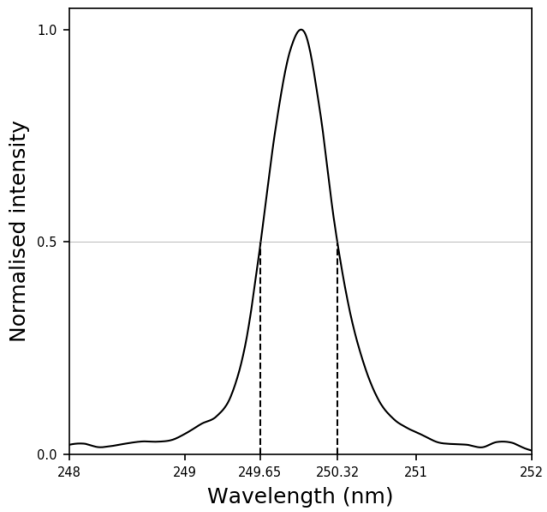


**Figure 2.15:** Spectral ray intensity profile at 250 nm, the full width at half maximum (FWHM) abscissa coordinates are 249.65 nm and 250.32 nm, which corresponds to a spectral resolution of 0.66 nm.

.

### 2.2.5 Circular dichroism determination

CD is determined by calculating the difference in absorption for left- and right-circularly polarised light expressed as $\Delta A$ (equation 2.4).

$$\Delta A = A_L - A_R \tag{2.4}$$

I obtain this value experimentally by measuring the transmitted intensity $I_0$ with the solvent, which is the intensity reference and the transmitted intensity $I$ with the diluted sample. The intensity reference and the intensity with the sample are measured from the same clusters of pixels. I obtain $\Delta A$ from this intensity measurements using the following Equation 2.5.

$$\Delta A = \log_{10} \frac{I_{0L}}{I_L} - \log_{10} \frac{I_{0R}}{I_R} \tag{2.5}$$

### 2.2.6 Sources of artifact

I encountered three principal sources of artifacts during this development. They come from the beam position, the difference of ellipticity between the two parts of the beam and the light scattering. In the following, I will describe their effect and explain how we limited their consequences.

#### 2.2.6.1 Elliptical polarisation difference

As described in the Introduction, the SR beam is divided in two parts which are elliptically polarised with opposite directions. In Section 2.2, I presented our approach to characterise the polarisation of the beam and our method to select pixels with which detect light with similar circularity. CD can be expressed with only the transmitted intensities[59] if the probe source has the same intensity for left and right-handed polarisation and if CD $\ll 1$

(Equation 2.6).

$$CD = \frac{I_R - I_L}{I_R + I_L} \tag{2.6}$$

The effect of using symmetrical elliptically polarised light for the CD measurements can be demonstrated straightforwardly using equation 2.6. As shown in Section 1.3.1, polarised light can be decomposed and expressed as the sum of linearly and circularly polarised light. We can express the intensity of elliptically polarised light as the sum of the intensities of the linearly and circularly polarised components. We have $I_{ell} = (I_{circ} + I_{lin})$, where $I_{lin}$ and $I_{circ}$ are the intensity of the linear and circular component of the elliptically polarised light, respectively. Thus, we obtain Equation 2.7 by substituting the intensities of circularly polarised light with elliptically polarised light in Equation 2.6.

$$CD = \frac{I_R - I_L}{2I_{lin} + I_R + I_L} \tag{2.7}$$

The intensity of the linearly polarised component only contributes to the denominator and thus only affects the amplitude of CD signals. It means that the use of elliptically polarised light does not affect the shape of the CD spectrum but only its amplitude, which can be anticipated and corrected. However, the CD signal is not proportional to the CD measured with circular polarisation if the circularity of the polarisation of the right and left-handed probes are different. Equation 2.8 corresponds to the expression of CD in the case that we have right-handed circularly polarised and left-handed elliptically polarised probes.

$$CD = \frac{I_{lin} + I_R - I_L}{I_{lin} + I_R + I_L} \tag{2.8}$$

We see in Equation 2.8 that the intensity of the linearly polarised component contributes to both the numerator and the denominator and thus its impact is not limited to the amplitude of the CD but it also convolutes the CD value. I tried to limit the impact of this artifact by following the procedure described in Section 2.2.

One of the main advantages of the absorbance difference method over the ellipsometry method is that this approach is less sensitive to LD contribution in CD measurement. However, this advantage is significantly reduced if the method uses elliptically polarised source. Indeed, the linearly polarized component will be absorbed differently than the circular component if the sample exhibits LD. The LD signal amplitude is generally several fold higher than CD amplitude. Thus, even if the intensity of the linearly polarised component is much smaller than the intensity of the circular component, it can convolute significantly the CD signal. We see in Figure 2.12 that after the pixel selection, the azimuth of the polarisation ellipse is almost the same for the upper and the lower beam. We expect that if the orientations of the ellipses are collinear, the contribution of the LD for the two parts of the beam will be the same and thus it will not induce a convolution in CD measurements.

#### 2.2.6.2 Beam optical path

Usually, for conventional spectrography setups, it is not necessary to filter the recorded image and so all the pixels can be used for the measurement of the signal. I explained in the sections above that in this case, I must select pixels according the polarisation state of the light they detect. However, two phenomena interfere with this approach, arising from the refractive index of

the sample and also from the orientation of the sample cell. A light beam is refracted at the interface between two media. The direction of propagation of the light changes if the refractive indices of the media are different and if the incidence angle is not equal to zero (Figure 2.16).

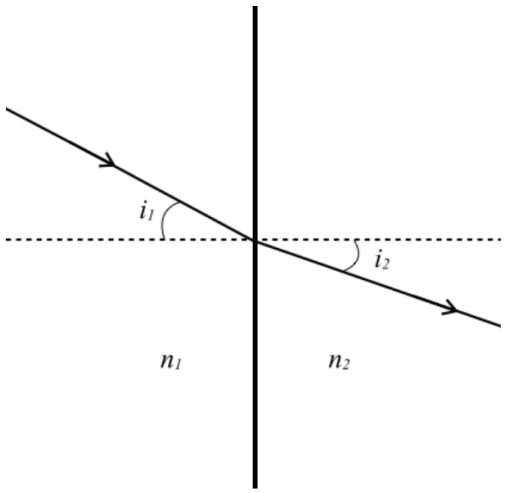


**Figure 2.16:** Scheme of a light beam refraction. $i_1$ and $i_2$ correspond to the angle between the beam and the normal before and after the interface, respectively. The direction of the light changes if the refractive indices of the media ($n_1$, $n_2$) are different and if the propagation direction is not orthogonal with the interface.

The relation that links the angle of the incident beam, the angle of the outgoing beam and the refractive indices of the media is given by Snell-Descartes law (Equation 2.9).

$$n_1 \sin i_1 = n_2 \sin i_2 \tag{2.9}$$

The direction and the diameter of the beam are modified each time it goes through a medium having a different refractive index than the medium that surrounds the optical bench, which is gaseous nitrogen in this case. The modification of the shape and the propagation direction of the beam induced by fixed optical components (*e.g* $CaF_2$ windows ) do not disturb the measurement. However, even though the design of the sample cell is optimised, its orientation changes after each sample loading. We need two intensity measurements to

determine the CD, a first with water, for the reference and a second with the sample of interest. It is near impossible to have exactly the same positioning of the sample cell for the two measurements. The slight difference in its orientation changes the incidence angle of the beam and so its direction after the sample cell. In addition, the beam provided by the DISCO beamline is not collimated, which means that it is either convergent or divergent along the beamline optical path, including the tr-SRCD setup. It means that the angle of incidence of the beam at interfaces is different to zero for the main part of the beam. Even if the orientation of the sample cell is the same for the intensity measurements with water and with the sample, the difference of refractive index of the two solutions induces slight changes in the beam shape as well. The modifications in the beam trajectory and/or in its shape change the position and the size of the beam projection on the detector. Thus, the image recorded with the water does not match the image recorded with the sample, and so it makes the measurement of the absorbance inaccurate. In this work, I use a flow cell as sample holder for the affordable samples to remove errors in positioning coming from the sample loading. In the case that the amount of available sample is limited, I hold it in a standard sample cell, which limits the study to relative CD measurements.

#### 2.2.6.3 Light scattering

Light scattering is a well known source of artifact in spectroscopy. The Rayleigh scattering is an elastic scattering of electromagnetic radiation by particle having a size smaller than the wavelength of the radiation. The magnitude of this phenomenon is inversely proportional to the wavelength and is more likely to occur at shorter wavelengths. The trajectory of the photons changes since they are scattered. If the deviation angle is too large, the photons are not collected and do not reach the detectors. For absorbance

measurements, the scattered photons will be counted as absorbed and will influence the absorbance value. Experimentally, it usually manifests as a baseline having an amplitude inversely proportional to the wavelength. The scattered light is not detected by the detector and so it is counted as absorbed in the absorption calculation. Thus, it induces an artifact in the resulting signal by increasing the value of the absorption. In the DUV/VUV range, this baseline amplitude can even be larger than the signal itself. In common spectrography setups that use one dimension detectors, this phenomenon induces an artifact that only affects the amplitude of the absorbance and can be partially corrected by fitting and subtracting the baseline of the spectrum. In our case, we detect the light using a 2D detector to be able to select the appropriate polarisation for CD measurements (Section 2.2). Thus, the scattered photons which have been deviated by a small angle can be detected by another pixel, belonging to the same column, rather than by the pixel that detects it for the reference intensity measurement. The initial pixel will show an higher absorbance and the second will show a lower absorbance because it detected a scattered photon. This phenomenon would not have a major impact if it were not necessary to select pixel of interest and if we could just integrate all the pixels within the same column. However, because we need this pixel selection, it induces a significant bias in the absorption determination.

In this section, I presented the main sources of artifacts I encountered during the development of the tr-SRCD setup. I first developed a methodology (Section 2.2) to limit the artifact that might be induced by a difference in the polarisation circularity between the two parts of the beam (Section 2.6.1). I found that the pixel selection generates two other sources of artifact which come from the beam deviation (Section 2.6.2) and the light scattering (Section 2.6.3). I limited significantly the beam deviation by using a flow cell as the sample holder. Concerning the bias induced by the light scattering, I did limit

it by focusing on relative CD measurement experiments. Thus, the scattered light is part of the reference and does not induce major bias. We can notice that all these biases could be avoided if the pixel selection was not necessary. This limitation comes from the use of the natural polarisation of the synchrotron radiation. I will present in the next section an approach that might be an alternative to performing absolute CD measurements.

### 2.2.7 Controlled polarisation configuration

I explained previously that the use of the natural polarisation makes the measurements of absolute CD difficult. In order to find a way to avoid this limitation, I performed first tests with an alternative configuration of the tr-SRCD setup. I used a combination of an achromatic quarter wave plate (Bernhard Halle) and a Rochon polariser (Bernhard Halle) made of $MgF_2$ to circularly polarise the whole beam (Figure 2.17).

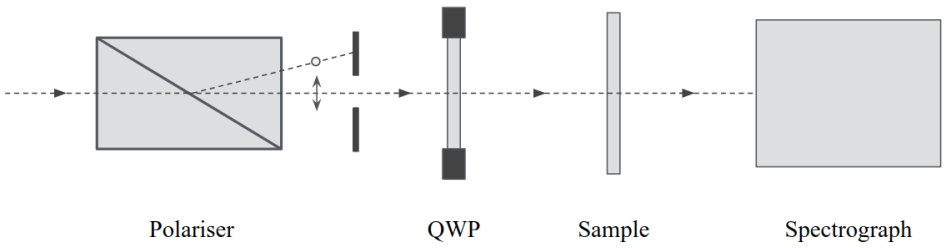


**Figure 2.17:** The combination of a Rochon polariser and an achromatic QWP to polarise circularly the synchrotron radiation. The extraordinary ray outgoing from the polariser is blocked by a diaphragm.

The polariser splits the beam into two rays linearly polarised with perpendicular orientation. The diaphragm filters the ray with the vertical linear polarisation. It passes through the QWP and the sample and it is analysed by the spectrograph. The polarisation state of the beam at the sample changes according the orientation of the QWP. The beam will be left- and right-circularly polarised when the QWP is oriented at -45° and 45° from

the orientation of the incoming polarisation, respectively. The light can be alternatively circularly right-handed to left-handed polarised by rotating the QWP by 90°. The transmitted intensity of the two polarisation states cannot be measured simultaneously but this approach ensures that the whole beam is almost perfectly circularly polarised. The specifications sheet of the QWP show that the deviation of the retardation remains below 8% between 180 nm and 300 nm. The curve of the deviation is available and thus the errors induced can be anticipated and corrected easily. Ideally, the two rays outgoing from the polariser could be circularly polarised separately with two different QWPs and then analysed simultaneously with the spectrograph. Thus, it would be possible to record CD spectra in the whole range of interest (180-300 nm) in only one measurement. If the projections of the two rays are far enough apart on the 2D detector, the light scattering and the beam deviation would not be an issue anymore, as well as the polarisation state. I performed a first test with the configuration shown in Figure 2.17. The results are presented in Chapter 3.

# 3 Experimental results

The main goal of this thesis work is the demonstration that the polarisation of synchrotron radiation can be used to measure CD signals. This objective was reached a few months after the beginning of the project by performing monochromatic measurements sequentially. However, as presented in Chapter 1, the potential of this approach comes from the capacity to measure the CD signal in a wide spectral range with only one intensity measurement. Thus it was necessary to use directly the broadband source provided by the DISCO beamline. First, we developed the methodology for the data processing and we calibrated the setup with camphorsulfonic acid (CSA), a well known calibration sample that exhibits a strong CD signal in the DUV range[60]. The results of this first development phase are presented in Section 3.1. Then we tested the capacity of the setup to follow reactions in real time by studying photocontrolled and reversible systems. The first system is the azobenzene crosslinked peptide FK-11-X[61]. It is composed of a 16 amino acid peptide cross-linked to a photoswitchable molecule, the azobenzene. This ligand can be isomerised from the *trans* to *cis* and *cis* to *trans* conformation using a 370 nm and a visible light source (460 nm), respectively. Its isomerisation triggers the unfolding/folding process of the peptide and thus induces changes in its CD signal[61,52]. I chose this sample for several reasons. It is a reversible system and thus the measured signal can be averaged over several cycles with the same sample loading which eases the enhancement of the SNR of the measurements. Moreover, the speed of the change in concentration of the two enantiomers depends on the intensity of the light sources used as a trigger for the isomerisation. Thus, it allowed me to adjust the speed of the process to assess the limits of the tr-SRCD setup. The results of this experiment are presented in Section 3.2. The second system is a solution of

DNA structures called G-quadruplex and azobenzene derivatives molecules. However, in this case the azobenzene molecule is not linked to the sample of interest. The azobenzenes are partially located inside the DNA structure and their isomerisation induces changes in the G-quadruplex structures and so in its CD signal. I chose this sample to complement the assessment of the capability of the tr-SRCD setup because the system is also reversible and because its CD spectrum shows a peak centered 260 nm. The absorption of the sample in this region is much lower than in the 180 nm to 210 nm range and thus the sources of artefact (light scattering and high absorption) are partially avoided, facilitating the comparison between different approaches to determine the CD signal. The results are presented in Section 3.3.

## 3.1 Camphorsulfonic acid

We chose CSA as our calibration sample, as it has two strong peaks in the VUV/deep UV range: the first at 290 nm and the second at 192 nm. It is commonly used as a calibration standard for CD spectrometers[55,60]. To validate that the recorded signal is CD, the two enantiomers must exhibit opposite signed spectra. We used CSA to calibrate the setup and evaluate the effectiveness of our approach. We first recorded steady-state spectra to estimate the SNR of the measurement and to confirm that our data processing is correctly calibrated (Section 3.1.1). Then we followed our first dynamic process consisting of the replacement of an CSA enantiomer by the other (Section 3.1.2). And finally we performed steady-state single pulse measurements to estimate the amount of light necessary to keep an acceptable SNR while having an high temporal resolution (Section 3.1.3).

### 3.1.1 CSA calibration

We elaborated and refined our data processing method using steady-state CD measurement of both CSA enantiomers, purchased from Sigma-Aldrich. We used the two peaks at 192 nm and 290 nm to validate the spectral calibration performed using the beamline monochromator. We also used these samples to test the reliability of the clusters of pixels used for CD determination pre-determined with the polarimetry. Some slight modifications on the pixel selection were necessary to enhance the proportion of the spectra, notably to obtain a ratio between the amplitude of the two peaks close to 2, as presented in the literature[60]. Because CD is orders of magnitude lower than the absorption, the CD signal is often convoluted by other phenomenon such as light scattering. With conventional SRCD spectrometers, the CD signal is directly determined from transmitted intensities measured for left- and right-circularly polarised light. It means that it is not necessary to measure the absorbance of the sample to determine its CD. It is also possible to measure the CD of the sample solvent to obtain the baseline of the measurement and thus be able to deconvolute any CD measurement by subtracting this baseline from the CD spectrum. This approach is only applicable if the intensity of the beam is the same for the two polarisation states. In our case, the two parts of the beam have different intensities, and we cannot determine the baseline of the measurement. However, in order to remove the baseline of the measurement, we can subtract the CD spectrum of the CSA racemic mixture. Indeed, the CD spectrum of the racemic mixture is flat and it only exhibits the baseline of the measurement. For this experiment, we subtracted the CD spectrum of the racemic mixture to correct the CD spectrum of the two CSA enantiomers. The resulting corrected spectra for D-CSA and L-CSA, measured between 190 nm and 315 nm for 30 mg/mL solution concentration, are shown in Figure

3.1. The PRIME CMOS detector has been used without the image intensifier. It integrated the light for 500 $\mu$s and the images were acquired at 20 Hz. As expected, we observe two oppositely signed spectra with identical amplitudes. The ratio of the amplitude of the two peaks is 1.98 $\pm$ 0.09 in the tr-SRCD spectra (curve (d) of Figure 3.1). The error bounds correspond to standard deviation of the ratio calculated using 6 values of CD at 192$\pm$0.5 nm and 6 others at 290$\pm$0.5 nm. The SNRs at 190 nm for the D-CSA spectra (a), (b), (c) and (d) in Figure 3.1 are 6.6, 12.7, 39.8 and 44.40, respectively.

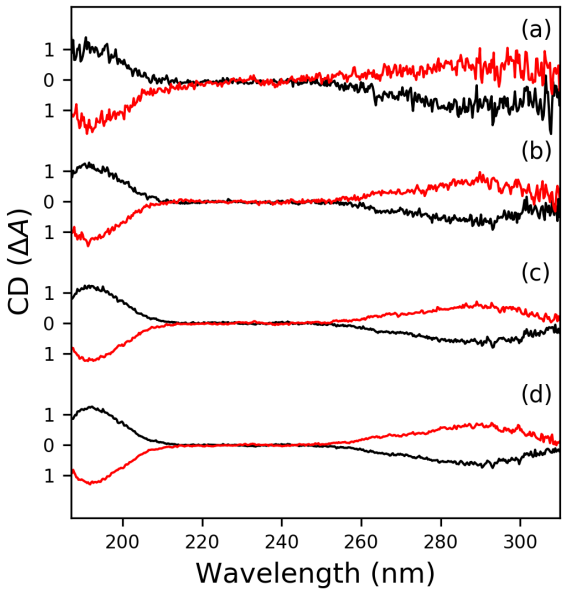


**Figure 3.1:** CD spectra of D-CSA (black) and L-CSA (red) acquired with the tr-SRCD setup at 20 Hz with 500 $\mu$s integration time. 1, 10, 50 and 100 measurements were integrated to obtain the data shown in curves (a), (b), (c) and (d) respectively.

### 3.1.2 Time resolved experiment

I used CSA in a second experiment aiming to test the capacity of the setup to record CD spectra in real time and to validate the acquisition protocol described in Section 2.2.1.1. I induced change in CD using a flow cell as the sample holder. I determined with preliminary work that we must inject a solution continuously for 1 minute to replace totally the solution initially

located in the flow cell. This estimation was performed by replacing water with a solution of CSA and assessed by monitoring the change in absorption. This experiment is divided into three phases. The flow cell initially contains a solution of L-CSA, after 1 minute of measurement, a solution of D-CSA is injected for 1 minute, and finally, images are recorded for 1 minute after the end of the injection. I expected that the signal would be inverted progressively during the injection of the D-CSA. The combination of the image intensifier and the ORCA-Flash4.0 V3 was used to record images. The images were recorded at 1 Hz and the width of the detection gate of the intensifier was set at 800 ns. In order to facilitate visualisation of the CD signal changes, I used the average of the 180 images as an intensity reference frame. It allows me to show the relative transient CD spectra of the solution. The results are presented in Figure 3.2.

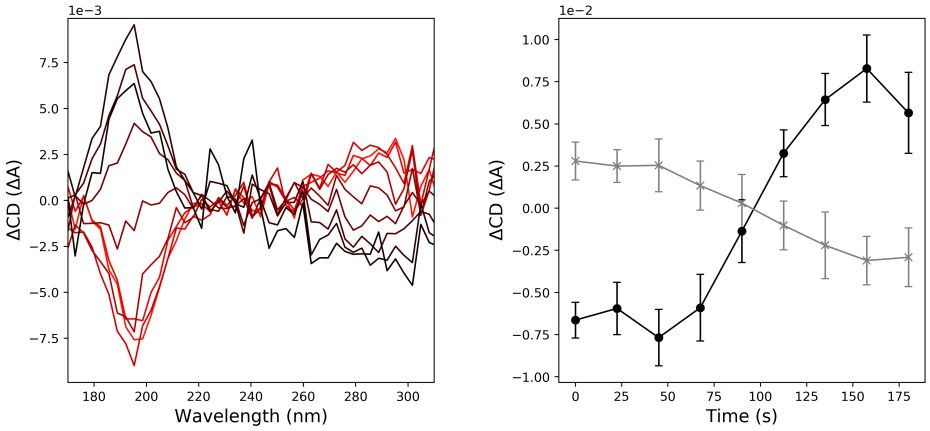


**Figure 3.2: a**. Transient CD spectra of the solution over time. Each plotted spectrum corresponds to the average of 20 spectra. The first (red) and the last (black) spectra are the relative CD spectrum of the initial solution (L-CSA) and the final solution (D-CSA) in the flow cell, respectively. **b.** Evolution of the relative CD signal at 190 nm (o) and at 290 nm (x). Each plotted data point corresponds to the average of 20 data points. The error bars represent one standard deviation.

As expected, the spectra in Figure 3.2a show the two peaks of the CSA at 190 nm and 290 nm. The first spectra (red) were measured when the flow cell was filled with the L-CSA. The sign of its peaks (negative at 190 nm

and positive at 290 nm) corresponds to the sign of the L-CSA CD spectrum peaks. The spectrum progressively reverses and finally becomes the same as the initial one but oppositely signed. It shows that the flow cell is filled by a solution of pure D-CSA at the end of the third phase. Based on the data of the Figure 3.2b, the ratio between the two peaks is 2.55±0.47. The difference from the expected value may comes from the disturbances brought by the flow and the variation of pressure in the flow cell. In Figure 3.2b, we observe that, as expected, the signal at 190 nm and 290 nm remains stable over one minute and then it changes to reach the same amplitude but oppositely signed after 2 minutes. The signal is stable during the last minute of the experiment, which shows that the solution in the flow cell only contains D-CSA during the last minute. The result matches with our expectations. It demonstrates that the tr-SRCD setup allows one to record broadband CD spectra in only one measurement and thus follow dynamics in real time. In this experiment, the temporal resolution of each measurement corresponds to the width of the detection gate of the intensifier, which is 800 ns. In this case we did not need an high temporal resolution so we concatenate the data to enhance the SNR. However, this experiment shows that the setup allows one to perform measurements having a 800 ns temporal resolution and having a SNR similar to that of the data in Figure 3.2a by averaging over approximately 20 cycles.

### 3.1.3 CSA single pulse measurements

We showed in the two previous Sections that we can record CD spectra with 520 $\mu$s and 800 ns temporal resolution using a CMOS detector and the combination of the CMOS detector with the image intensifier, respectively. We presented in Section 2.2.1.2 a method that might allow one to avoid the temporal resolution limitation of both the CMOS detector and the image intensifier by using the temporal distribution of the synchrotron radiation. We

used this acquisition protocol to establish the highest theoretical temporal resolution of the setup that is attainable experimentally. We performed a steady state experiment on the CSA with the maximal temporal resolution as a proof-of-principle. The intensifier was triggered with an external trigger and its detection gate width was reduced to its shortest value, 100 ns. The measurements were made using the 8 bunch mode of the synchrotron SOLEIL which provides 89 ps pulses at 7.14 MHz. The intensifier amplified only one pulse per gate. So its temporal resolution corresponds to the pulse length, which, in this case, is 89 ps. In Figure 3.3, each spectrum comes from ten images; 500 separated pulses were integrated for each image. The spectral range was reduced to between 255 nm and 300 nm, in order to optimize the setup for the detection of the peak at 290 nm. The signal-to-noise ratio at 290 nm for the D-CSA spectrum is 10.33.

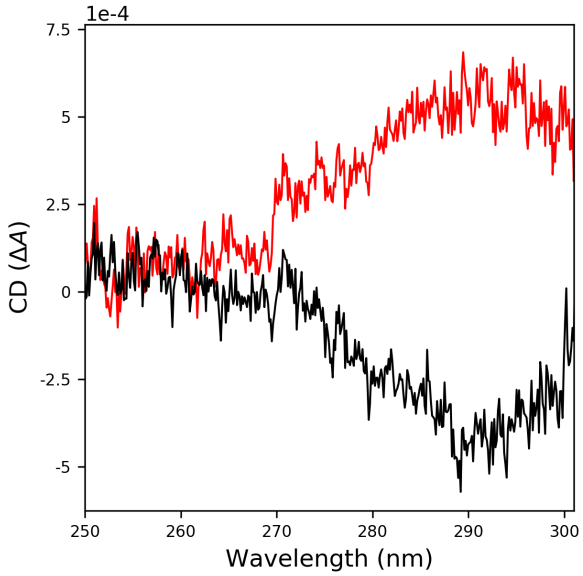


**Figure 3.3:** CD spectra of D-CSA (black) and L-CSA (red) from single pulse measurements acquired with the tr-SRCD setup at 500 Hz with 89 ps intensifier gate duration; 5000 measurements were integrated.

## 3.2 FK-11-X

We tested the capacity of the setup to follow reactions in real time by studying a photocontrolled and reversible system, the azobenzene crosslinked peptide FK-11-X[52,62]. It is composed of a 16 amino acid peptide cross-linked to a photoswitchable molecule, the azobenzene (Figure 3.4).

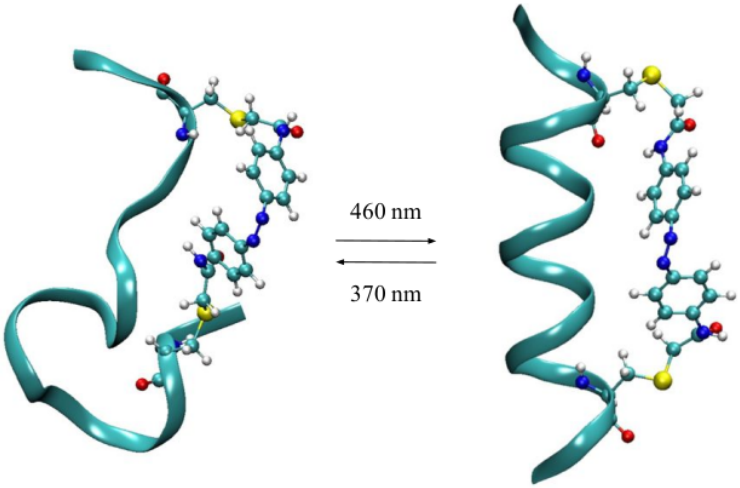


**Figure 3.4:** Schematic representation of the FK-11-X molecular system for both *cis* and *trans* conformations. Its amino acid sequence is Ac-Glu-Ala-Cys$^{AZO}$-Ala-Arg-Glu-Ala-Ala-Ala-Arg-Glu-Ala-Ala-Cys$^{AZO}$-Arg-Gln-$NH_2$.

This ligand can be isomerised from the *trans* to *cis* and *cis* to *trans* conformation using a 370 nm and a visible light source (460 nm), respectively. Several groups have studied the dynamics of this photo-induced reaction and the isomerisation of the azobenzene appears to occur within one picosecond[63,64,65,66]. This conformational change constrains the peptide structure and triggers its folding and unfolding processes. Theoretical[52,67,61], and experimental[68] studies agree that, following the azobenzene isomerisation, peptide conformational changes occur on the microsecond scale. The aim of our study was to follow the change in concentration of the unfolded (*cis* azobenzene) and folded (*trans* azobenzene, ground state) FK-11-X peptide. We triggered the isomerisation with two continuous diodes, at 370 nm (5W) and at 460 nm (5W). The concentration of FK-11-X solution was 10 mg/mL

in phosphate buffer (70 mM, pH 7). The sample has been synthesized by Nay *et al.* from the Laboratoire de Synthèse Organique of the Ecole Polytechnique. The azobenzene cross-linked peptide was synthesized as described previously [52]. The purification procedure is presented in Appendix A1.

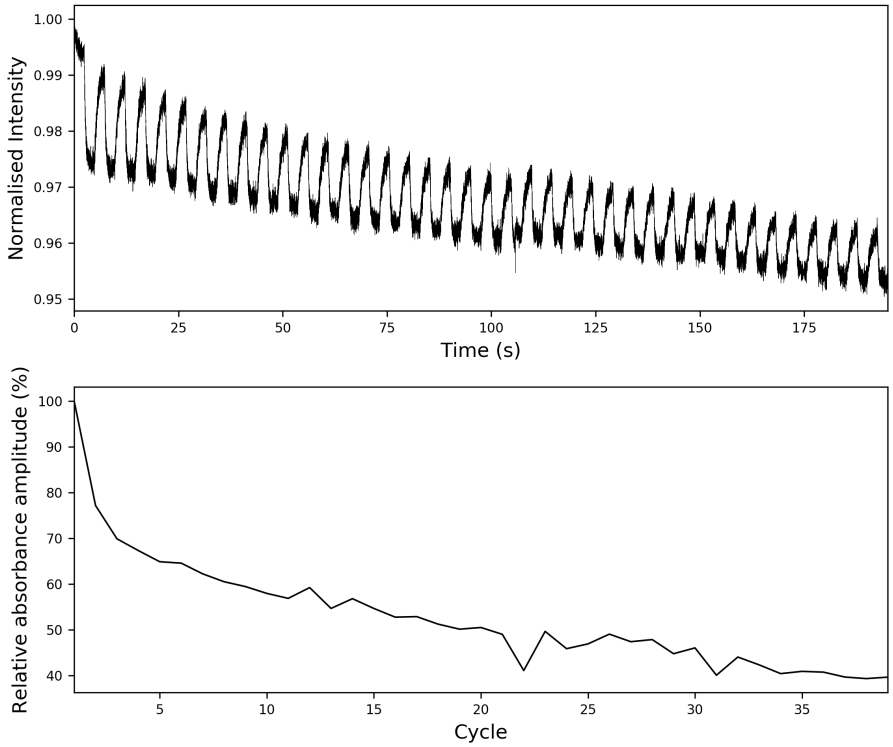


**Figure 3.5: a.** Normalized sum of all the pixels of the recorded image over the 40 cycles. **b.** The normalized absorbance variation for each cycle. The values are normalised by the absorbance variation of the first cycle and represented as a percentage.

The sample was alternately irradiated with the two diodes. The sample was first irradiated 2.5 seconds with the 460 nm diode to trigger the *trans* to *cis* isomerisation and then 2.5 seconds with the 370 nm diode to trigger the *cis* to *trans* isomerisation. The transient CD and absorption spectra of the concentration changes of the isomers were followed, measuring spectra at 130 Hz with a 520 $\mu$s temporal resolution; the measurement has been integrated over 40 cycles of alternate irradiations. The variations in the total intensity and absorbance are shown in Figure 3.5. The variation of the

sum of the pixels intensity over the 40 cycles (Figure 3.5a) shows that the alternate irradiations lead to changes in the beam intensity. It means that, as expected, a modification of the FK-11-X conformation occurs when the solution is irradiated. These structure modifications induce a change in the molecule absorption. The amplitude of the intensity variation during a cycle decreases progressively over time. In order to facilitate the quantification of this effect, I represented in Figure 3.5b the normalised variation in absorbance for each cycle. The absorbance variation is determined using the maximum and the minimum intensity value for each cycle. The values are normalised by the absorbance variation of the first cycle. The absorbance variation decreases after each cycle and reaches approximately 43% at the end of the experiment. I believe that this phenomenon comes from the photo-degradation of the sample due to its sensitivity to UV light. When a molecule is degraded, the azobenzene isomerisation does not trigger the change in conformation of the peptide anymore and thus its absorption becomes stable. The absorption and its variation are proportional to the concentration of the chemical species. Thus, it would mean that 57% of the FK-11-X molecules in the solution are degraded after 40 cycles. This could be an issue if it were necessary to compare experiments that were averaged over different number of cycles but in our case, it only leads to a decrease in the averaged CD signal amplitude. So I averaged the intensity over 39 cycles and looked at the absorption and CD variations. The first half of the first cycle is not taken into account for the averaging because the azobenzene configuration is *cis* and so the first 2.5 second of irradiation with the 460 nm diode does not affect its configuration. Thus, the first 2.5 seconds of the average cycle correspond to the 370 nm irradiation and the last 2.5 seconds to the 460 nm irradiation. The results are presented in Figure 3.6. The concentration change of the isomers induces a variation in the absorption of the sample and so in the measured intensity. The evolution

of the total intensity measured by the detector is shown in Figure 3.6a. The intensity decreases from the first milliseconds after the beginning of the 370 nm irradiation. The measured intensity stabilizes after 1 second of irradiation. The irradiation at 460 nm that triggers the *cis* to *trans* isomerisation starts at 2.5 seconds. The measured intensity increases progressively over the next 2.5 seconds to reach approximately the initial value measured at $t_0$. The slight difference comes from the global decrease in intensity shown in Figure 3.5a that might come from the degradation of the FK-11-X. This plot shows that the solution contains principally *cis* FK-11-X after 1 second of irradiation with the 370 nm diode.

This plateau does not correspond to an equilibrium between the diode flux and the lifetime of the *cis*-isomer.The FK-11-X peptide is relatively stable in its *cis* configuration and it needs tens of minutes to naturally switch from the *cis* to the *trans* configuration[68]. It also shows the complete reversibility of the concentration ratio because the normalised intensity returns to its initial value at the end of the cycle. The intensity reference $I_0$ for the determination of the absorbance variation and so for the CD calculation corresponds to the average of the intensity measured between 1 and 2.5 seconds. In this time range, almost all the molecules are in their *cis* configuration. Thus, the absorbance and CD variation measurements shown in Figure 3.6c, d , e and f correspond to the variation from the absorbance and CD spectrum of a solution of *cis* FK-11-X peptides. The absorption variation (Figures 3.6.c and 3.6.d) shows two peaks, at 198 nm and 212 nm. The absorption variation naturally follows the same dynamics as the normalised intensity. It decreases progressively and reaches a plateau where $\Delta A \approx 0$ in the whole range of interest because the intensity reference is measured from these time frames. The CD variation spectra (Figure 3.6e) are close to the signal of the $\alpha$-helical structure and the decreasing amplitude reflects the change of the species concentration. The first

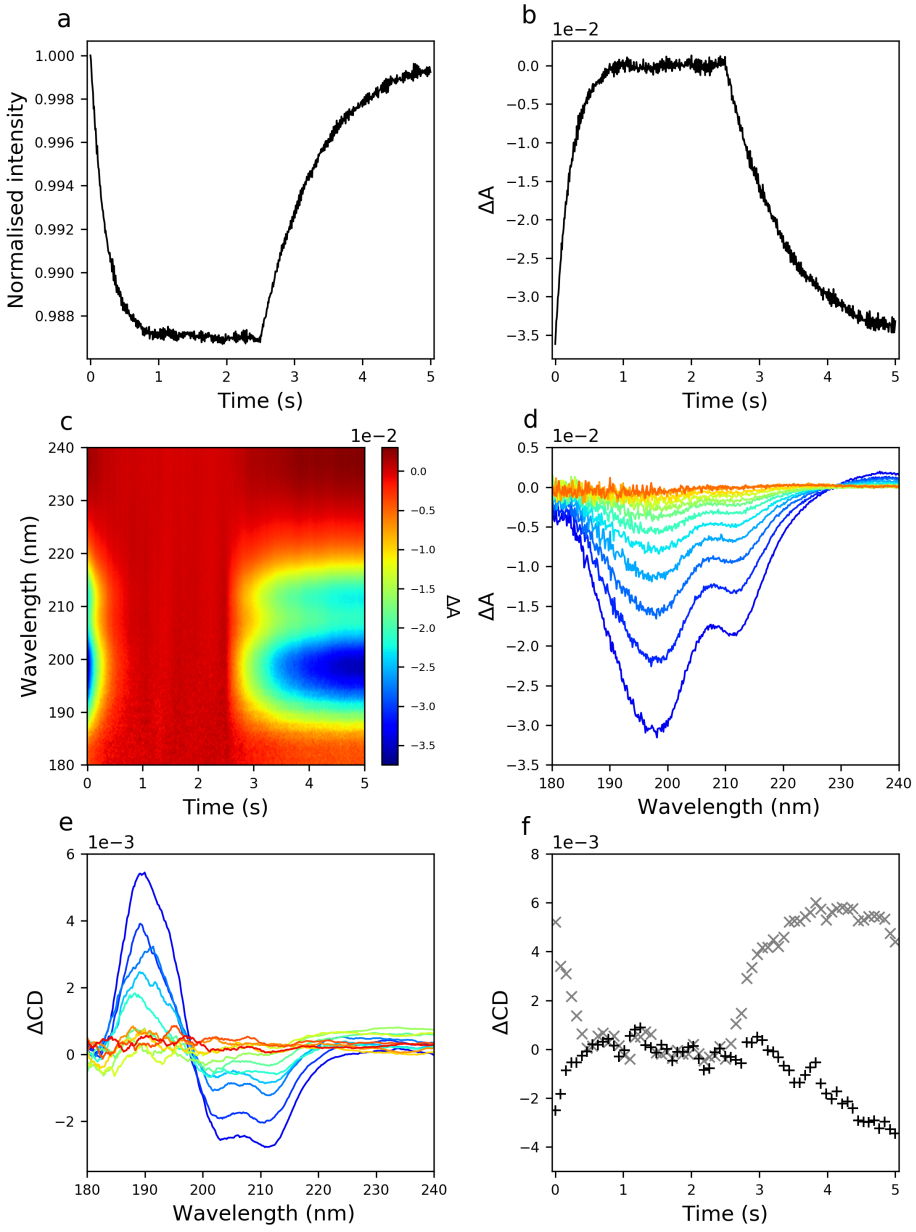


**Figure 3.6:** **a.** Evolution of the normalised sum of the pixels intensity over time.**b.** Evolution of the absorbance at 200 nm over time. **c.** 2D representation of the evolution of the global absorbance over the cycle; 650 spectra are shown. **d.** Evolution of the absorption during the 370 nm irradiation. Each represented spectrum corresponds to the concatenation of 10 spectra resulting in a 77 ms time step. The 12 spectra show the evolution of the absorption over the first 923 ms after the trigger. **e.** Evolution of the CD during the 370 nm irradiation. The concatenation is the same as the Figure d. **f.** Evolution of the CD at 190 nm (x) and 204 nm (+) over the cycle.

spectrum (blue) corresponds to the total difference between the CD spectrum of the unfolded (*cis*) FK-11-X peptide and its folded (*trans*) configuration. Then the concentration of the *trans* configuration decreases progressively during the 370 nm irradiation and so the amplitude of the CD difference decreases as well until it reaches approximately zero before the first second of irradiation. The CD variations at 204 nm and 190 nm (Figure 3.6f) also confirm the reversibility of the system. The CD difference returns to its initial value at $t_0$ after the 2.5 seconds of irradiation with the 460 nm diode.

I presented in this Section my first study on a system that partially consists of a biological molecule. The reversibility of the system allowed me to average the signal easily and follow the change in concentration of the two configurations of the FK-11-X over time. The dynamics of the structural change occur within a microsecond after the isomerisation of the azobenzene. This is too fast to be followed with this configuration of the tr-SRCD setup which only uses the CMOS detector for intensity measurements. This first limitation can be avoided by using the configuration and the protocol presented in Section 2.2.1.2.b. We demonstrated the reliability of this approach in Section 3.1.3. The second limitation comes from the intensity of the 370 nm irradiation. It is necessary to isomerise all the azobenzene molecules within a time range shorter than the duration of the unfolding process. In this experiment, we irradiated 3 $mm^2$ of the sample holder aperture with a 5 W laser diode. We see in Figure 3.6a that approximately 500 ms of irradiation are necessary to isomerise more than 90% of the azobenzenes. It means that more than 2.5 Joules are necessary to isomerise all the molecules inside the sample holder. I performed the first tests using a high energy pulsed laser (NT342B, EKSPLA). The duration of the pulses provided by the laser is 6 ns (FWHM) which is suitable for this application. The energy of each pulse is about 5 mJ and the repetition rate of the laser can be set either at 10 Hz or 20 Hz. The energy

of one pulse is 500 times lower than the energy necessary for the complete isomerisation with a spot size of 3 $mm^2$. There are two ways to reduce this difference. The spot size can be reduced to increase the energy density of the irradiation and decrease the concentration of the sample to reduce the number of azobenzene. I said in Section 1.3 that the diameter of the probe beam can be decreased down to 300 $\mu$m. In order to keep an homogeneous irradiation, the spot diameter of the irradiation beam can be reduced to twice the diameter of the probe beam, so around 600 $\mu$m. The energy density can be increased by a factor 6 through this way. I then diluted the concentration of the sample but we did not manage to isomerise more than 10% of the sample with one pulse, which was not enough to obtain the CD signal. The dilution of the sample enhance the effectiveness of the irradiation but it also reduces the amplitude of the CD signal. It would be preferable to increase the power of the irradiation source rather than dilute the sample. A tripled high energy Q-switched Nd:YAG laser would be the right choice. It provides a pulsed beam at 355 nm, which is less efficient than irradiation at 370 nm but it would be compensated by the high pulse energy. Some products provide pulses having an energy above 1 J (*e.g* NL310 Series, EKSPLA). This kind of product would isomerise all the molecules with only one pulse without diluting the solution.

## 3.3 G-quadruplex

I proposed in Section 2.7 a different approach that gives a full control of the beam polarisation by using polarising optical components. The complete setup necessary to have a fully operational device would require many changes in the tr-SRCD setup but I can perform a first test to assess the reliability of this approach. I expected that this method would avoid all the sources of artifact described in Section 2.6 and thus would allow one to perform absolute

measurements. I showed in Section 3.2 that a system based on the azobenzene isomerisation is convenient for experimentation. The reversibility of the system significantly facilitates the measurements of the CD signal by allowing cycles averaging. I used the same configuration to trigger conformation changes in another system. A mixture of a DNA G-quadruplex structure and azobenzene derivative molecules was used to assess the reliability of the method presented in Section 2.6.

A G-quadruplex is a folded structure of DNA having a guanine rich sequence[69,70] that is formed in the presence of $Na^+$ or $K^+$ ions. Recently, these structures have been found in vivo in human cells in the telomeres[71]. The G-quadruplex structure is formed by the association of four guanines that constitute a planar tetrad (Figure 3.7a). It can be formed by guanines that belong to the same DNA strand (Figure 3.7b) or by four individual strands. The G-quadruplex we studied is formed by the Tel21 sequence (GGGTTAGGGTTAGGGTTAGGG). They are encountered in

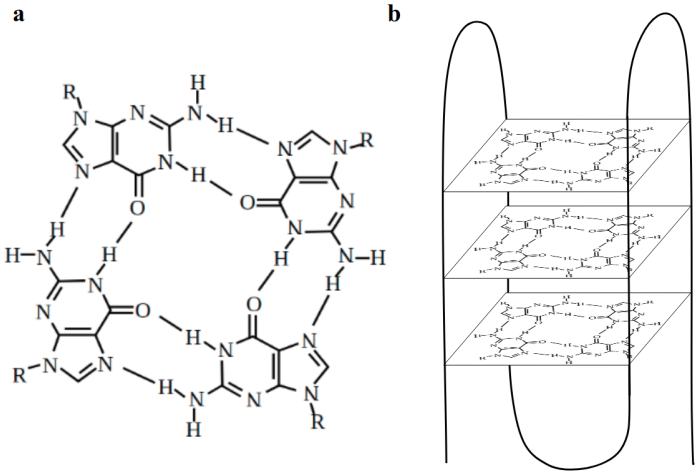


**Figure 3.7: a.** A guanine tetrad structure. **b.** Single strand G-quadruplex.

human telomeres. In our system, the azobenzene derivatives are not linked to the DNA structure and their concentration is seven times higher than the concentration of G-quadruplex. Systems based on the non-bonded association of azobenzene derivatives and G-quadruplexes were recently studied. Xing *et*

*al.*[53] and Wang *et al.*[72] demonstrated that the *trans* configuration of the azobenzene derivative can play the role of cation and allow the folding of a guanine-rich DNA strand into a G-quadruplex structure. Moreover, they recorded CD and absorption spectra of the solution before and after the isomerisation of the azobenzene derivative and they showed that it triggers the unfolding process of the G-quadruplex. They also showed that the reaction is fully reversible.

I followed a similar protocol to the one we used for the experiment of the section 3.2. I irradiated the sample with 370 nm and 460 nm diodes. However, in this case I optimized the setup to increase the speed of the azobenzene isomerisation to compensate for the higher azobenzene derivative concentration. I placed the sample holder at the waist of the probe beam, resulting in a spot diameter of approximately 300 $\mu$m. I used two 370 nm diode lasers of 5 W for the *trans* to *cis* isomerisation and one at 460 nm of 5 W for the *trans* to *cis* isomerisation. The laser beams are focused on the sample cell to obtain a spot diameter of approximately 600 $\mu$m for the 3 lasers. Thus the energy density of the 370 nm irradiation in the sample cell is increased by approximately a factor 25 compared to the experiment in the previous section. I also doubled it by adding a second laser at 370 nm. Thus, at similar concentration, the speed of the azobenzene isomerisation should be 50 times faster than the experiment presented in the previous section. The sample is irradiated for 3 seconds with the 460 nm laser and for 2 seconds with the two 370 nm lasers. I repeated the measurements three times, with three different approaches. I recorded a steady state spectrum after each irradiation with the standard SRCD setup, with the tr-SRCD using the method of the experiments in the previous sections and with the tr-SRCD setup using the method presented in Section 2.7. For the SRCD spectra, the signal was measured with a 1 nm step and with an integration time of one second. For the two acquisitions that

use the natural polarisation of the synchrotron radiation, 350 images were recorded and averaged with an integration time of 520 $\mu$s. For the acquisition of the method presented in Section 2.7, I needed to record two sets of images with the QWP orientated at -45° and 45° from the vertical. I acquired these two sets after the two irradiations, with an integration time of 520 $\mu$s for each image. For the two acquisitions with the tr-SRCD setup, I determined the absolute CD with Equation 2.6. $I_L$ and $I_R$ correspond to the intensities of the upper and the lower beam for the method that uses the natural polarisation and to the intensity of the whole beam with the QWP oriented at -45° and 45° for the method that uses the polarising components. The concentration of the DNA and the concentration of the azobenzene was, respectively, 0.9 mM and 6.3 mM. The path length of the sample cell was 20 $\mu$m. The sample has been synthesized by Changenet *et al.* from the Laboratoire d'Optique et Bioscience and Nay *et al.* from the Laboratoire de Synthèse Organique of the Ecole Polytechnique. The results are shown in Figure 3.8. The SRCD spectra in Figure 3.8a exhibit a positive peak at 265 nm and a negative peak at 241 nm. The spectra recorded with the polarising components shown in Figure 3.8b also exhibit a positive peak around 265 nm but it seems that the baseline of the measurement convolves the shape of the spectra and has a more important impact on the smaller negative peak at 241 nm because it is only negative for the spectrum of the solution with the folded structure. I explained in Section 2.6.1 that Equation 2.6 only applies if the elliptically right and left-handed beam have the same intensity. For this experiment, the difference of intensity between the upper and the lower beam was approximately 30%. We see in Figure 3.8e that this difference induces a large baseline in the spectra. The amplitude of the baseline is approximately two orders of magnitude larger than the amplitude of the signal. However, there is still a difference between the two spectra around 260 nm and 240 nm. I plotted in Figure 3.8b, 3.8d and 3.8f the

difference of the two spectra shown in Figure 3.8a, 3.8c and 3.8e, respectively. The baseline of the two spectra is removed with this subtraction and we can objectively compare the signals measured with the different approaches. The difference between the two SRCD spectra and the difference between the two spectra from the measurements with the polarising optical components are (Figure 3.8a and 3.8c, respectively) similar. They both exhibit a positive peak around 260 nm and a negative peak at 240 nm.

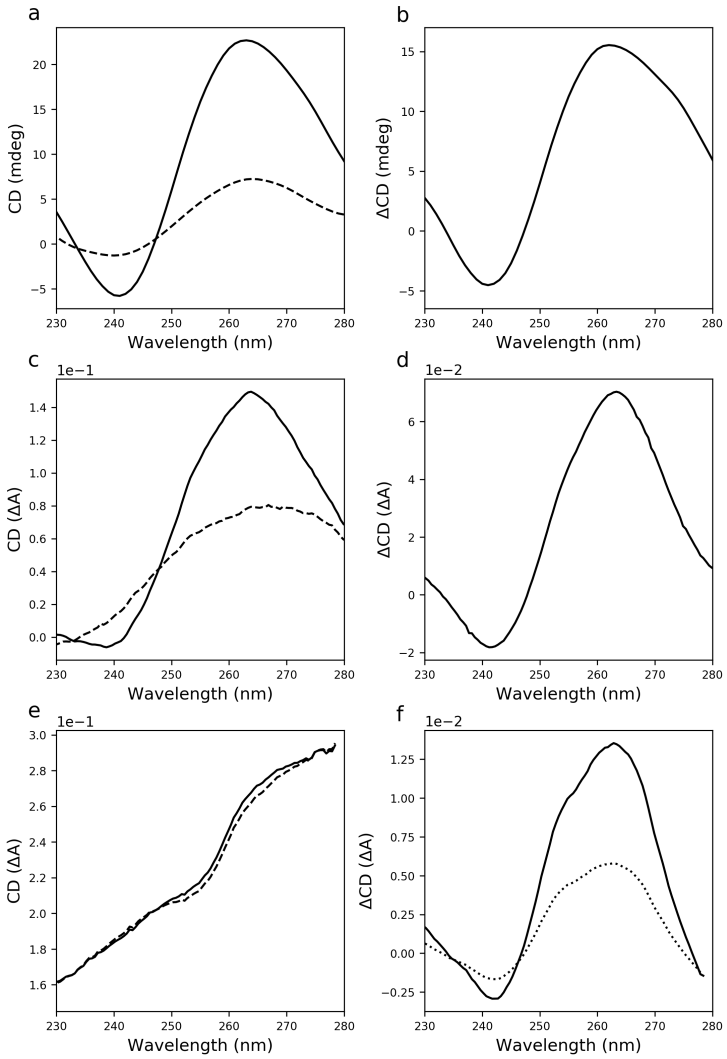


**Figure 3.8: a.**, **c.** and **d.** Steady state absolute CD spectra of the solution with *cis* (dashed) and *trans* (solid) azobenzene derivative recorded with the standard SRCD setup, the polarising components setup and the tr-SRCD setup, respectively. **b.**, **d.** and **f.** The solid lines correspond to the difference between the CD spectra plotted in Figure 3.8a, c and e respectively. The dotted line in Figure f. corresponds to the relative CD spectra determined by the relative absorbance method used for the results in Section 3.1 and 3.2.

The ratio between the two peaks is also around -3 in both cases. It means that the CD signal measured with the SRCD setup and using the tr-SRCD setup with polarising optical components are nearly identical. However, it would be necessary to extract the baseline of the measurements by recording the CD spectrum of the solution buffer and then subtracting it from the CD spectrum. In Figure 3.8f, the spectrum plotted with the dotted line corresponds to the relative CD determined using Equation 2.5 and the spectrum represented with the solid line is the difference between the two spectra shown in Figure 3.8e. Thus, the comparison between the relative CD obtained from the same data set and the same method but using two different equations is possible. As expected, the two relative CD spectra measured with the natural polarisation correspond to the difference between the SRCD spectra (Figure 3.8b). However, there is a slight difference between 260 nm and 280 nm. The slope of the peak is different. The CD difference reaches zero at 275 nm while the difference between the SRCD spectra is still positive. In addition, the amplitude of the signal is about twice as large when it is determined using Equation 2.5 compared to the difference computed with Equation 2.6. It confirms that Equation 2.6 induces a bias in the measurement of CD if the intensity of the two parts of the beam are different. There is also a significant difference between the peak to peak amplitude of the CD variation measured with the natural polarisation and with the polarisation from polarising optical components. Indeed, their peak to peak amplitudes are approximately 0.015 and 0.09, respectively. It means that the amplitude of CD signals measured with the tr-SRCD setup are about six-fold larger using polarising optical components than using synchrotron radiation natural polarisation.

The aim of this experiment was to test whether the use of polarising optical components can enhance the capability of the tr-SRCD setup. I compared absolute CD spectra measured with standard SRCD setup to spectra measured

with tr-SRCD setup using both the natural polarisation and polarising optical components. The results of the absolute CD measurement show that the amplitude of the baseline is much smaller with the polarising optical components. In addition, the equation I use for absolute CD determination does not depend on a reference intensity. It means that an estimation of the baseline can be obtained by measuring the CD of the solution buffer. This baseline determination is not possible with the natural polarisation method because it uses Equation 2.5 which depends on an intensity reference $I_0$. The results also show that the amplitude of the CD signal is approximately six times larger using the almost perfectly circular polarisation provided by the polarising optical components than using the natural polarisation of the synchrotron radiation. These results are promising and show that the potential of the tr-SRCD setup could be enhanced by controlling the polarisation of the beam with polarising optical components. This modification would allow one to perform accurate absolute CD measurement and it would significantly increase the amplitude of the measured signals.

## 3.4 Conclusions

I organised the experimentation chapter of the thesis in three parts. I first focused on the development and the calibration of the tr-SRCD setup by performing the first acquisitions on CSA. In Section 3.1.1, I first presented a proof of principle, which validates experimentally that the natural polarisation of the synchrotron radiation is suitable for CD measurements. I demonstrated that balanced CD spectra can be obtained by using an appropriate selection of pixels. I also used this experiment to assess the performance of the setup by estimating the signal to noise ratio of the measurements according the number of averaged images. I showed that the exceptional brilliance of the

synchrotron radiation allows one to record CD spectra in only one measurement with an acceptable SNR. I tested several detectors with different protocols to find the optimum configuration for each type of application. I selected two complementary configurations for the detection chain that would allow one to follow dynamics occurring within a wide time range spanning from nanoseconds to seconds time scales. The combination of the ORCA-Flash4.0 V3 with the image intensifier will be dedicated to the high speed dynamics occurring on the nanoseconds and microseconds time scale and the PRIME camera will be used for slower dynamics or steady state measurements. I presented in Section 3.1.2 a first time-resolved experiment using the combination of the image intensifier and the camera. This experiments shows that this configuration gives access to a sub-microsecond temporal resolution. Despite a lower signal to noise ratio compared to the PRIME configuration, this approach provides a significant advantage. Indeed, it overcomes the limitation brought by the minimal exposure time of the CMOS camera. I also used CSA to demonstrate the capacity of the tr-SRCD to perform single pulse measurements. The results are shown in Section 3.1.3, we measured the CD spectrum of L-CSA and D-CSA from single pulse intensity measurements. In the second phase of the experimentation part, I used the tr-SRCD setup to measure relative transient CD spectra of a biological sample, the FK-11-X. I used lasers to trigger a change in concentration of the *cis* and *trans* configurations in the sample. We observed the concentration variation dynamics through time-resolved measurements with 520 $\mu$s temporal resolution. This experiment demonstrates the capacity of the tr-SRCD setup to measure time-resolved CD spectra of biological sample. It also shows the efficiency of the nitrogen purge with the measurement of the CD signal down to 180 nm. The spectra presented in Section 3.1 and 3.2 cannot be considered as absolute spectra. In section 3.1, I had to subtract the CD spectrum of the racemic mixture from the

spectra of the enantiomers to remove the baseline. They show the relative CD signal between the racemic mixture and one of the enantiomers. The results presented in Figure 3.6 also correspond to relative measurements. I considered the initial intensities as the references and I recorded the variation from these initial states. I used this methodology to avoid the artifacts described in Section 2.6. Relative measurements are suitable to study dynamics by recording transient spectra but they are limited for studies that aim to analyse spectra for structure determination. I dedicated the last part of the chapter to the assessment of an alternative approach that would facilitate absolute CD measurements. I presented in Section 2.2.6 the different sources of artifacts we identified arising from the use of the natural polarisation. I proposed in Section 2.2.7 a method in which we use polarising optical component to control the polarisation state of the synchrotron radiation. The results of the first test are presented in Section 3.3. We observed that the amplitude of the CD signal is several times higher than with the use of the natural polarisation. I also shown that this method allows one to measure absolute CD spectra and the associated baselines. These promising preliminary results in the development of a synchrotron radiation spectrography setup show that this method might allow one to study ultrafast dynamics occurring on the nanoseconds time scale with broadband measurements without using microfluidic devices. I will present in Chapter 4 a study of the FK-11-X molecule based on molecular dynamics simulations that may complement experimental results.

# 4 Theoretical study of FK-11-X

In Section 3.2, I presented a preliminary investigation on the FK-11-X. I used the natural polarisation of the synchrotron radiation to record transient CD spectra of a FK-11-X solution which allowed me to observe the concentration changes of the enantiomers. I also showed in Section 3.1.3 that a combination of an image intensifier and a CMOS detector allows single pulse measurement. It means that with an appropriate pulsed laser for the FK-11-X isomerisation with the acquisition protocol presented in Section 2.1.2.b one might be able to follow the unfolding process of the FK-11-X with 82 ps temporal resolution using the tr-SRCD setup. Recently, Hildebrand *et al.* studied the structure of the C-terminal $\alpha$-helix of chymotrypsin[73]. They compared computed CD spectra calculated from MD simulation snapshots to experimental CD spectra. Their results show a good agreement between experimental and calculated spectra. It means that combining experimental and theoretical approaches can provide valuable information about partially folded $\alpha$-helix structures. In addition, Michaelis *et al.* demonstrated that an appropriate sampling of $\alpha$-helix structures between a folded and unfolded state allows one to generate reliable computed spectra of transient states[74]. In this chapter, I propose a structural study of FK-11-X based on molecular dynamics (MD) simulations to show how a theoretical approach would complement experimental tr-SRCD measurements. I will describe the methodology for the system set up and parameterisation and for the isomerisation. I will analyse the structural changes induced by the isomerisation. Finally, I will present an analysis based on experimental and computed CD spectra.

## 4.1 Method

### 4.1.1 System set up

I built the peptide and the azo-moiety with the Avogadro software[75] (version 1.2.0), using the feature that allows one to generate an $\alpha$-helix structure from an amino acid sequence. I constructed the azo-moiety in its *trans* configuration, placed it close to the position where it should be when it is linked to the peptide. I created the bonds between the azo-moiety and the two sulfur atoms of the cysteines with the creation of the protein structure file (.psf). I added the two bonds and I generated the PSF file using the PSF builder extension provided by VMD[76]. The resulting molecule after minimisation is shown in Figure 4.1. All the molecular visualisations presented in this thesis were rendered using the Tachyon extension in VMD.

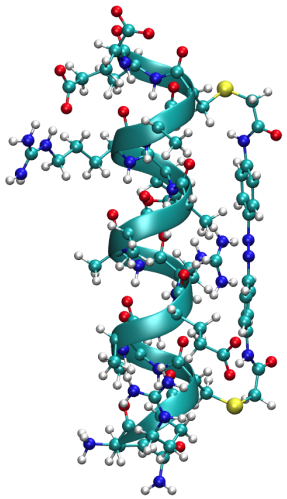

**Figure 4.1:** Structure of the FK-11-X peptide. Its amino acid sequence is Ac-Glu-Ala-Cys$^{AZO}$-Ala-Arg-Glu-Ala-Ala-Ala-Arg-Glu-Ala-Ala-Cys$^{AZO}$-Arg-Gln-$NH_2$.

The molecule is solvated using a box of TIP3P water.[77] I determined the appropriate size of the water box from the length of the peptide and the cutoff distance of the non-bonded interaction I used for the simulation. I performed

a preliminary MD simulation with the unfolded peptide to estimate of the maximum length of the peptide. The distance between the C- and N-termini never exceeded 35 Å. The cutoff distance for the non-bonded interactions is 12 Å, so I set the edge of the cubic water box at 50 Å. The solvated system (Figure 4.2) comprises 15570 atoms.

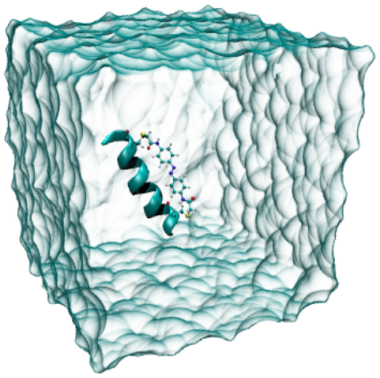

**Figure 4.2:** Representation of the solvated FK-11-X peptide.

### 4.1.2 System parameterisation

I performed the simulation presented in this thesis work using NAMD[78]. NAMD models the bonded and non-bonded interactions of each atom with all the other atoms of the system with a potential energy function (Equation 4.1). The first three terms describe the bonded interaction, comprising stretching, bending, and torsional, respectively. The last two terms correspond to the non-bonded interactions, the van der Waals and the electrostatic interactions, respectively.

$$U_{total} = U_{bond} + U_{angle} + U_{dihedral} + U_{vdW} + U_{Coulomb} \tag{4.1}$$

The expression of the bonded interaction are shown in Equations 4.2, 4.3 and 4.4.

$$U_{bond} = \sum_{bonds\ i} k_i^{bond}(r_i - r_{0i})^2 \tag{4.2}$$

$$U_{angle} = \sum_{angles\ i} k_i^{angle}(\theta_i - \theta_{0i})^2 \tag{4.3}$$

$$U_{dihedral} = \sum_{dihedrals\ i} k_i^{dihedral}[1 + \cos(n_i\phi_i - \gamma_i)] \tag{4.4}$$

where $k$, $r_0$, $\theta_0$, $\gamma$ and $n$ are the force field parameters of the bonded interaction. $r$, $\theta$ and $\phi$ corresponds respectively to the distance between two atoms, an angle formed by three bonded atoms and the angle between two planes defined by four bonded atoms.

The equations that describe the van der Waals (approximated by a Lennard–Jones 6 –12 potential) and the electrostatic interactions are shown in Equations 4.5 and 4.6, respectively.

$$U_{vdW} = \sum_i \sum_{j>i} 4\varepsilon_{ij} \left[ \left( \frac{\sigma_{ij}}{r_{ij}} \right)^{12} - \left( \frac{\sigma_{ij}}{r_{ij}} \right)^{6} \right] \tag{4.5}$$

$$U_{Coulomb} = \sum_i \sum_{j>it]} \frac{q_i q_j}{4\pi\varepsilon_0 r_{ij}} \tag{4.6}$$

where $\epsilon$ is the potential well depth, $\sigma$ is the distance where the potential equals zero, $r$ is the distance between the two atoms, $q$ is the charge of the particle and $\epsilon_0$ is the vacuum electric permittivity.

The parameters of each atom, bond, angle and dihedral angle are stored in a force field parameter file. In this thesis work, I used the CHARMM36 All-Hydrogen force field[79,80,81] for the parameterisation of the peptide. For the azo-moiety, Carstens[82] developed parameters that have been used in some

studies[52,68]; and Böckmann *et al.*[83] proposed a set of force field parameters for an azobenzene derivative. However, even if I could use the same parameters for the azobenzene, I would still need parameters for the atoms that link the peptide to the azobenzene. I used the online interface[84] of the CHARMM General Force Field[85] (CgenFF) to determine the required parameters of these atoms by analogy with existing parameters of small organic molecules. This tool provides a penalty score for each attributed parameter. If this score is higher than 50, the parameters do not suit the molecule and so it is necessary to develop a customized force field for the corresponding bonds/angles. In the case of the azo-moiety, this score remains below 50 except for the parameters of the dihedral angles. These dihedral angles have a relatively low contribution to the total potential energy function. So I performed some preliminary tests using the CHARMM36 All-Hydrogen force field for the parameterisation of the peptide, the parameters proposed by Böckmann *et al.*[83] for the azobenzene and the parameters generated by CGenFF for the atoms between the azobenzene and the peptide. However, the FK-11-X did not behave as expected. The strain applied by the *cis* azobenzene did not induce a decrease in the helical content of the peptide structure even after 25 ns of simulation. Time-resolved IR spectroscopy[86,87] and optical rotatory dispersion spectroscopy[68] (ORD) experiments shown that the first changes in conformation appear within a few nanoseconds after the isomerisation of the azobenzene. I concluded that the force field parameters given by CGenFF were not adequate. I developed a force field for the whole molecule, rather than use Böckmann *et al.*'s parameters[83] for the azobenzene, to ensure internal consistency. The methodology and the results are presented in Section 4.1.3.

### 4.1.3 Development of the azo-moiety force field

I followed the procedure proposed by Vanommeslaeghe *et al.*[85]. It consists of optimising the parameters to obtain similar potential energy profiles calculated from geometries minimized with quantum mechanical (QM) and molecular mechanical (MM) approaches. The geometries and energy profiles from QM are the target of the optimisation process. I considered the azo-moiety as comprising two smaller molecules to reduce the number of degrees of freedom of the system. I optimized separately the parameters of the azobenzene (Figure 4.3a) and the atom chain that links the azobenzene to the peptide (4.3b). I added a sulfur and a methyl to the carbon $C_4$ to determine the parameters of the link between the cysteines of the peptide and the azo-moiety.

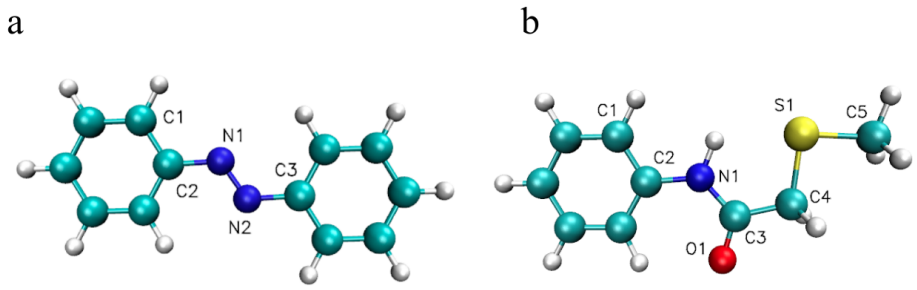


**Figure 4.3: a.** Azobenzene **b.** Structures used for the force field parameter optimisation of the linker between the azobenzene and the peptide.

The first step of the procedure is the partial atomic charge determination to attribute a charge to each atom. I generated the initial guesses with CGenFF. The penalty scores were below ten for all the atoms except four atoms of the azobenzene ($C_2$, $N_1$, $N_2$ and $C_3$). However, for these four atoms, differences between the charges generated by CGenFF and the charges proposed by Böckmann *et al.*[83] were below 5%. So we kept the initial guess of the partial atomic charges generated by CGenFF for the optimisation and for the simulations. We computed the QM geometries with Q-Chem[88] at the MP2/6-31G* level of theory. We calculated the energy profile for all the

bonds, the angles and the dihedral angles involving atoms that are indexed in Figure 4.3. The parameters of the benzene rings and the parameters of the bonds/angles involving hydrogens are generated by CGenFF.

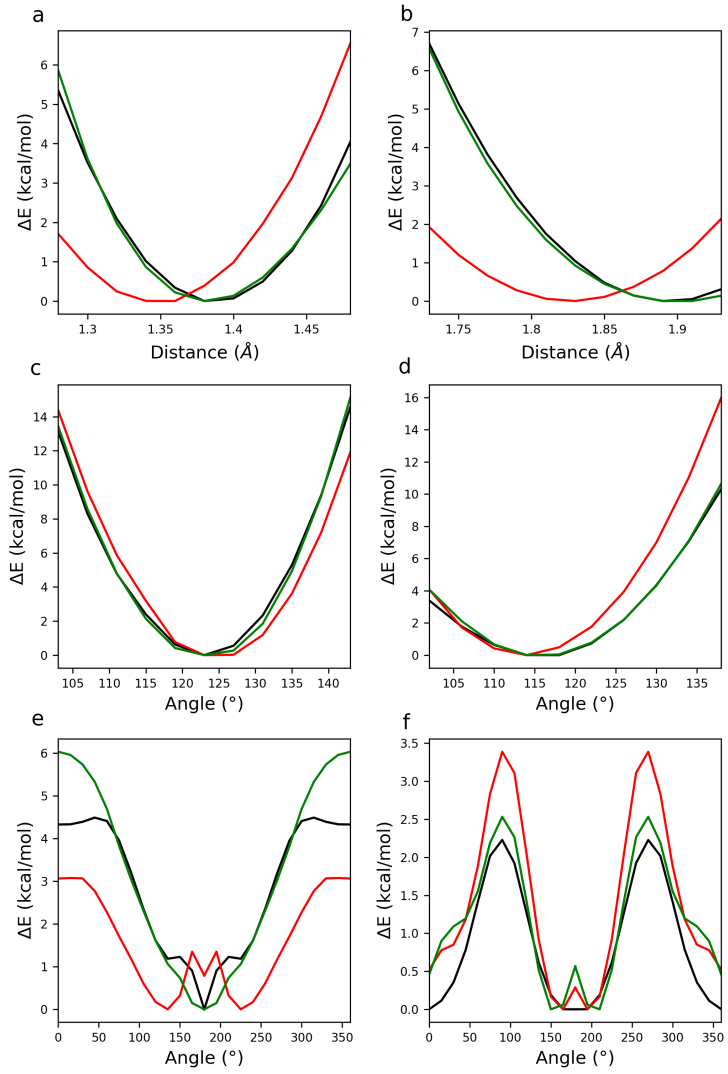


**Figure 4.4:** Examples of potential energy profiles of the structure shown in Figure 4.3b. The profile from MP2/6-31G* geometries are plotted in black. The profile from MM geometries minimised using initial guess and optimised parameters are plotted in red and green, respectively. **a.** $N_1C_3$ bond **b.** $C_4S_1$ bond **c.** $C_1C_2N_1$ angle **d.** $C_3C_4S_1$ angle **e.** $O_1C_3C_4S_1$ dihedral angle **f.** $C_1C_2N_1C_3$ dihedral angle.

I computed the MM minimisation of the structures with NAMD. I adjusted the parameters 'by hand' until the energy profiles from MM fit with the profile from QM. I first optimised the parameters of the bonds, then the parameters of the angles and finally the parameters of the dihedral angles.

Examples of the potential energy surfaces are shown in Figure 4.4. Both the MM geometries computed with initial guess and optimised parameters are represented. The energy profiles calculated with the initial guess from CGenFF are significantly different compared to the profiles based on QM calculations. These differences may be responsible for the qualitatively incorrect behaviour we observed in the preliminary simulations using the initial guess. The profiles obtained with the optimised parameters are closer to the target and should improve the fidelity of the simulation. The optimised parameters are presented in Tables 4.1, and are compared in Appendix (Tables A2.1 and A2.2).

**a.**

| **Dihedral angle** | $k$ (kcal/mol) | $n$ | $\delta$ (°) |
|---|---|---|---|
| $C_1C_2N_1C_3$ | 1.20 | 2 | 180 |
| $C_2N_1C_3O_1$ | 2.65 | 2 | 180 |
| $C_2N_1C_3C_4$ | 2.00 | 2 | 180 |
| $N_1C_3C_4S_1$ | 0.50 | 1 | 180 |
| $O_1C_3C_4S_1$ | 0.50 | 1 | 0 |
| $C_3C_4S_1C_5$ | 0.24 | 1 | 180 |
| **Angle** | $k$ (kcal/mol) | $\theta_0$ (°) | |
| $C_1C_2N_1$ | 70 | 115.2 | |
| $C_2N_1C_3$ | 60 | 120.8 | |
| $N_1C_3O_1$ | 92 | 124.5 | |
| $N_1C_3C_4$ | 68 | 118.0 | |
| $O_1C_3C_4$ | 78 | 122.0 | |
| $C_3C_4S_1$ | 40 | 115.3 | |
| $C_4S_1C_5$ | 58 | 99.0 | |
| **Bond** | $k$ (kcal/mol) | $b_0$ (Å) | |
| $C_2N_1$ | 380 | 1.420 | |
| $N_1C_3$ | 460 | 1.385 | |
| $C_3O_1$ | 830 | 1.275 | |
| $C_3C_4$ | 250 | 1.542 | |
| $C_4S_1$ | 225 | 1.893 | |
| $S_1C_5$ | 225 | 1.893 | |

**b.**

| **Dihedral angle** | $k$ (kcal/mol) | $n$ | $\delta$ (°) |
|---|---|---|---|
| $C_1C_2N_1N_2$ | 2.5 | 2 | 180 |
| $C_2N_1N_2C_3$ | 23.0 | 2 | 180 |
| **Angle** | $k$ (kcal/mol) | $\theta_0$ (°) | |
| $C_1C_2N_1$ | 50 | 116.5 | |
| $C_2N_1N_2$ | 75 | 106.0 | |
| **Bond** | $k$ (kcal/mol) | $b_0$ (Å) | |
| $C_2N_1$ | 300 | 1.415 | |
| $N_1N_2$ | 500 | 1.295 | |

**Table 4.1: a.** Optimised force field parameters of the molecule shown in Figure 4.3.b. **b.** Optimised force field parameters of the azobenzene (Figure 4.3.a).

### 4.1.4 Molecular dynamics simulation method

The temperature was maintained at 295 K using Langevin dynamics parameters with a friction coefficient of 5 $ps^{-1}$. The pressure was kept constant at 1 atm with a Langevin piston that modifies the size of the unit cell to adjust the pressure. The maximum distance of non-bonded interactions was 12 Å. Cubic periodic boundary conditions were used. Electrostatics were treated using the particle-mesh Ewald method[89] with a grid spacing of 1 Å. We used the SETTLE algorithm[90] and the ShakeH algorithm[91] to constrain water molecules and the other bonds involving hydrogen atoms, respectively. I performed two sets of simulations. The first is composed of 40 trajectories where the azobenzene is isomerised in the *cis* form and a second set of 10 trajectories with the *trans* configuration of the azobenzene, which served as a control. Each of the trajectories consisted of 120 ns of production dynamics. In each case, the initial structure was minimized for 200 steps and was equilibrated for 200 ps, which was sufficient based on the convergence of the root-mean-squared deviation (RMSD). The averaged RMSD value of the peptide backbone is plotted as a function of the time in Figure 4.5.

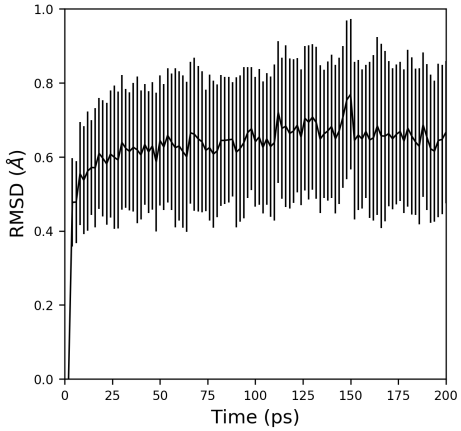


**Figure 4.5:** RMSD variation over time. The error bars width corresponds to one standard deviation. The RMSD calculation is only base on the atoms of the peptide backbone.

RMSD is usually used to determine whether a structure is equilibrated.

It is proportional to the averaged distance between each atom and a reference. The value is calculated with Equation 4.7.

$$RMSD = \sqrt{\frac{1}{N}\sum_{i=1}^{N}\delta_i^2} \tag{4.7}$$

where $\delta$ is the distance between the atom $i$ in a specific time frame and the same atom in a reference structure. $N$ is the number of atoms in the structure.

The reference of the RMSD calculation was the initial conformation of the equilibration simulation. We see that the value of the RMSD increases rapidly over the first 25 ps of the simulation and then stabilises around 0.65 Å. The stabilisation of the value shows that the backbone structures reach stable conformations and that the systems are equilibrated.

There are two methods to trigger the isomerisation of the azo-moiety. One can use a QM approach[67] or a potential energy triggering[92]. I used the second option. The principle of this method is to change the parameters of the dihedral angle responsible of the azobenzene configuration (C-N-N-C). I modified the multiplicity of this dihedral from two to one (see Figure 4.6a). This modification changes the number of minima from two to one. The unique energy minimum is located at 0°, which corresponds to the *cis* configuration of the azobenzene. I performed a 1.5 ps simulation with this modification for each structure starting from the conformation of the last step from the equilibration trajectory. The averaged value of the C-N-N-C angle of the azobenzene over time is plotted in Figure 4.6b. The dihedral angle decreases from 180° to approximately 60° before the first picosecond. The angle passes the potential barriers located at -90° and +90° when $n = 2$ and so the azobenzene will remain in the *cis* conformation even with $n = 2$. I used the conformation of the last step from the 40 isomerisation trajectories for the 120 ns simulations.

For these simulations, the multiplicity parameter of the C-N-N-C dihedral angle was $n = 2$. The results are presented in Section 4.2.

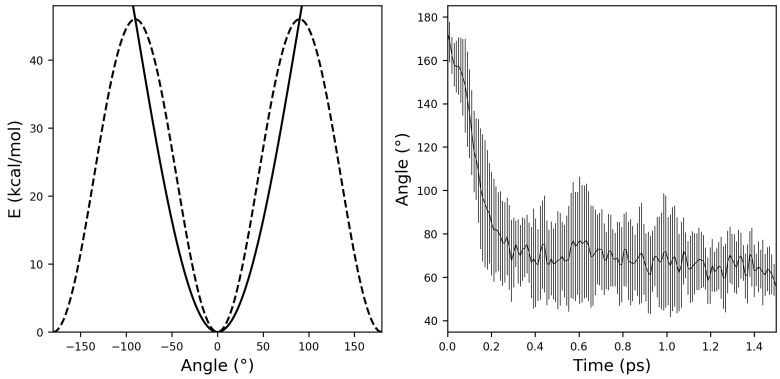


**Figure 4.6: a.** C-N-N-C dihedral angle energy function with multiplicity $n = 1$ (solid line) and $n = 2$ (dashed line). **b.** Averaged C-N-N-C dihedral angle value over the isomerisation trajectories. The error bars correspond to one standard deviation.

## 4.2 Results

### 4.2.1 Unfolding process analysis

By visual inspection, I identified that in approximately 80% of cases, the trajectories are similar. A representative case is shown in Figure 4.7. The peptide starts to unfold within the first 10 to 50 ps. In all these trajectories, the peptide eventually attains the same conformation, which seems stable. In Figure 4.7, this conformation corresponds to the structure at 40 ns. Depending on the trajectory, it takes between 10 and 30 ns to reach this conformation.

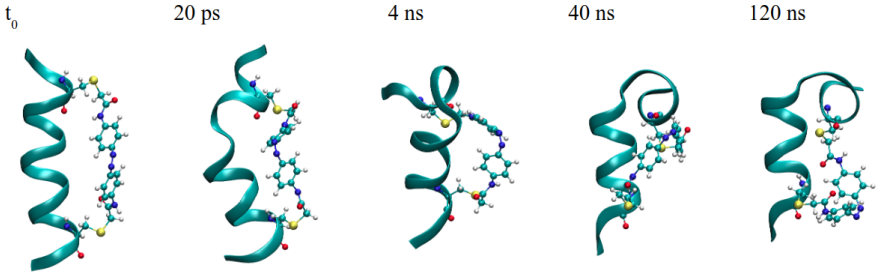


**Figure 4.7:** Typical trajectory from the 40 simulations.

The helical structure that remains is formed by six residues (Ala-Arg-Glu-Ala-Ala-Ala). The three consecutive alanines are localised at the centre of the peptide. Alanine has a propensity to form and stabilise $\alpha$-helix structure[93]. This property and central location likely explain the high stability of this part of the peptide $\alpha$-helix conformation. I also identified other trajectories where the unfolding process is in a more advanced state after 120 ns. One of these trajectories is shown in Figure 4.8. In this case, the peptide is completely unfolded after 80 ns. Although the structure of the $\alpha$-helix is modified after 80 ps, it only starts to unfold after 200 ps. The conformation at 10 ns is similar to the stable conformation we identified in Figure 4.7. However, in this case,

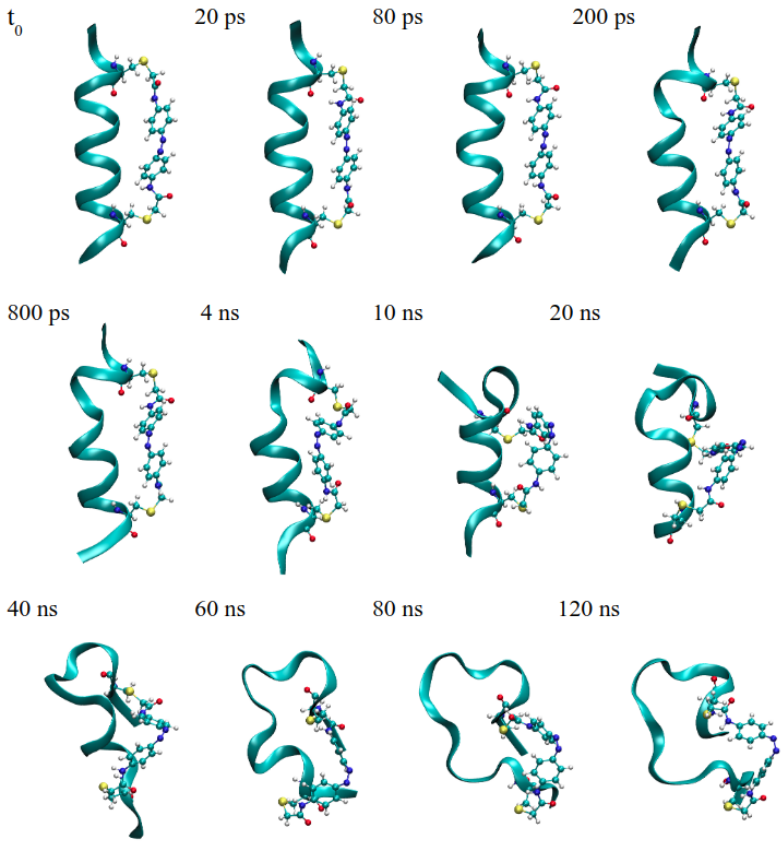


**Figure 4.8:** A trajectory where the peptide is completely unfolded by the end of the simulation.

the peptide continues to unfold and the unfolding process is completed after 80 ns, approximately. The trajectory in Figure 4.8 is less frequent than the type shown in Figure 4.7. It occurs only once in the set of 40 trajectories.

We can gather more detailed information about the unfolding process using a Ramachandran plot representation (Figure 4.9) showing each residue from the trajectory presented in Figure 4.8.

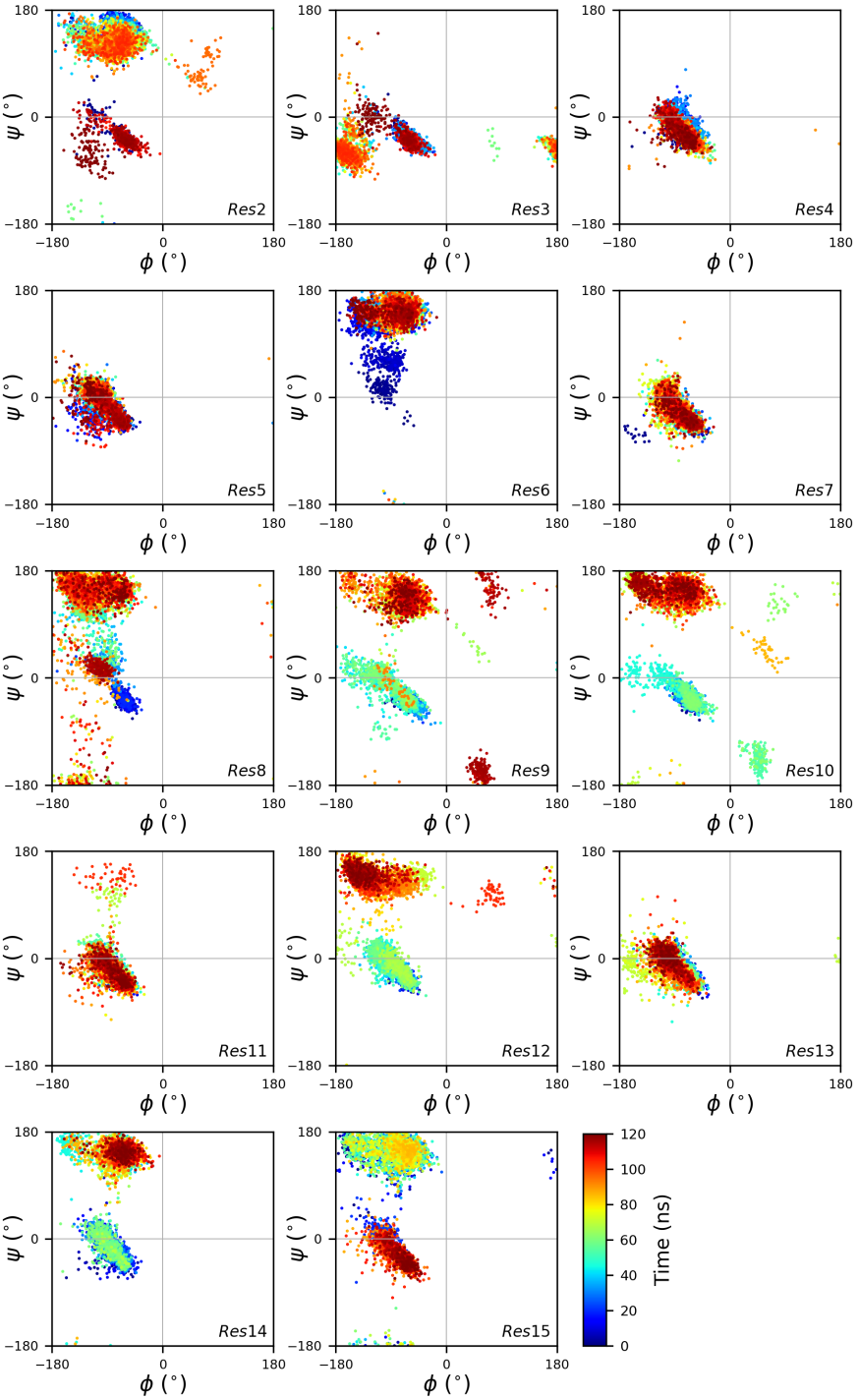


**Figure 4.9:** Ramachandran plots of the trajectory shown in Figure 4.8. The colour of the scatter plot corresponds to the time of the simulation.

Figure 4.9 allows me to obtain information about the secondary structure of each residue[94]. The two most represented secondary structures are the $\alpha$-helix and the $\beta$-strand. They correspond to the cluster of points centered around $\phi = -57°$, $\psi = -47°$ and $\phi = -80°$, $\psi = 150°$, respectively. As expected, all the residues form an $\alpha$-helix structure at the beginning of the simulation. The dihedral angles of the residues Arg2, Glu6, Ala8 and Ala15 are the first to change. They are followed by the residues Ala9, Ala10, Arg12 and Cys14, which switch from the helical region to the extended structure region of the Ramachandran plot. The dihedral angles of the residues Arg2, Cys3, Ala8 and Ala15 return approximately to their initial value at the end of the simulation. The dihedral angles of the residues Arg2, Ala9, Ala10, and Arg12 transiently populate the upper-right quadrant of the Ramachandran plot, which corresponds to the region of the left-handed $\alpha$-helix structure. In Section 4.2.2, I will propose alternatives to facilitate the assessment of the unfolding process.

### 4.2.2 Unfolding dynamics analysis

In order to quantify the rate of the unfolding process I examine some representative quantitative progress coordinates, such as the distance between the two sulfur atoms and the $O_i$-$H_{i+4}$ distances. The S-S distance is directly related to the structure of the azo-moiety. I expect that, once isomerised, the azo-moiety tends to a lower energy conformation with this configuration. I also think that as long as the distance between the two sulfur atoms decreases, the azo-moiety induces a strain on the peptide. The hydrogen bond between $O_i$ and $H_{i+4}$ characterises the $\alpha$-helix structure and the distance between these two atoms allows one to assess the stability of the structure[95]. The averaged $O_i$-$H_{i+4}$ distance of the peptide residues will probably be partially correlated to the distance between the two sulfur atoms but we can expect that the

conformation of the peptide continues to change even after the S-S distance converges. The S-S distance and the $O_i$-$H_{i+4}$ distances are presented in Figures 4.10 and 4.11, respectively.

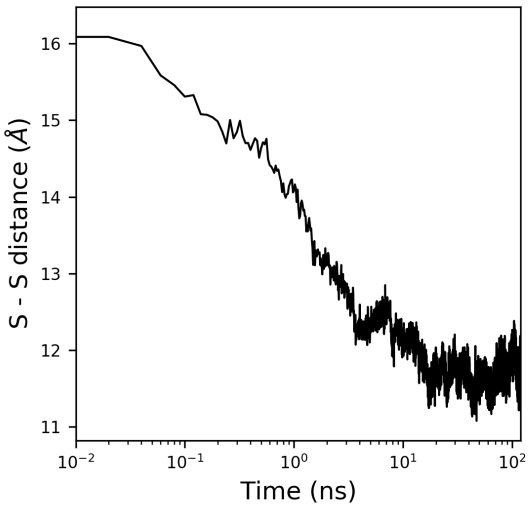


**Figure 4.10:** Distance between the two sulfur atoms of the cysteines over time (logarithmic scale).

In Figure 4.10, the S-S distance decreases from 16 Å to 12 Å within the first 10 ns of the simulation. Then it stabilises between 11 Å and 12 Å until the end of the simulation. We see in Figure 4.11a the heterogeneity in the speed of unfolding over the 40 trajectories. The trajectory in Figure 4.8 is trajectory number 26. Its averaged $O_i$-$H_{i+4}$ distance over time is plotted in Figure 4.11b. The averaged $O_i$-$H_{i+4}$ distance from the 40 trajectories with the *cis* azo-moiety is shown in Figure 4.11c. The abscissa scale is logarithmic so the $O_i$-$H_{i+4}$ distance increases exponentially. The averaged $O_i$-$H_{i+4}$ distance increases after 10 ns even though the S-S distance is constant. Thus, the peptide structure continues to change. In Figure 4.11b we see that the averaged $O_i$-$H_{i+4}$ distance when the peptide is completely unfolded is approximately 7.5 Å. Considering that Figure 4.11c shows that the averaged $O_i$-$H_{i+4}$ distance increases by approximately 1 Å every order of magnitude and reaches 4.5 Å after 100 ns, it suggests that all the peptides should be completely unfolded

after 100 $\mu$s.This extrapolated value does not correspond to values determined experimentally, which range between 100 ns and 1 $\mu$s[68,86]. I will continue this comparison with experimental measurements in the next section. In Figure 4.11d, I plot the averaged $O_i$-$H_{i+4}$ distance for the first 12 residues. This

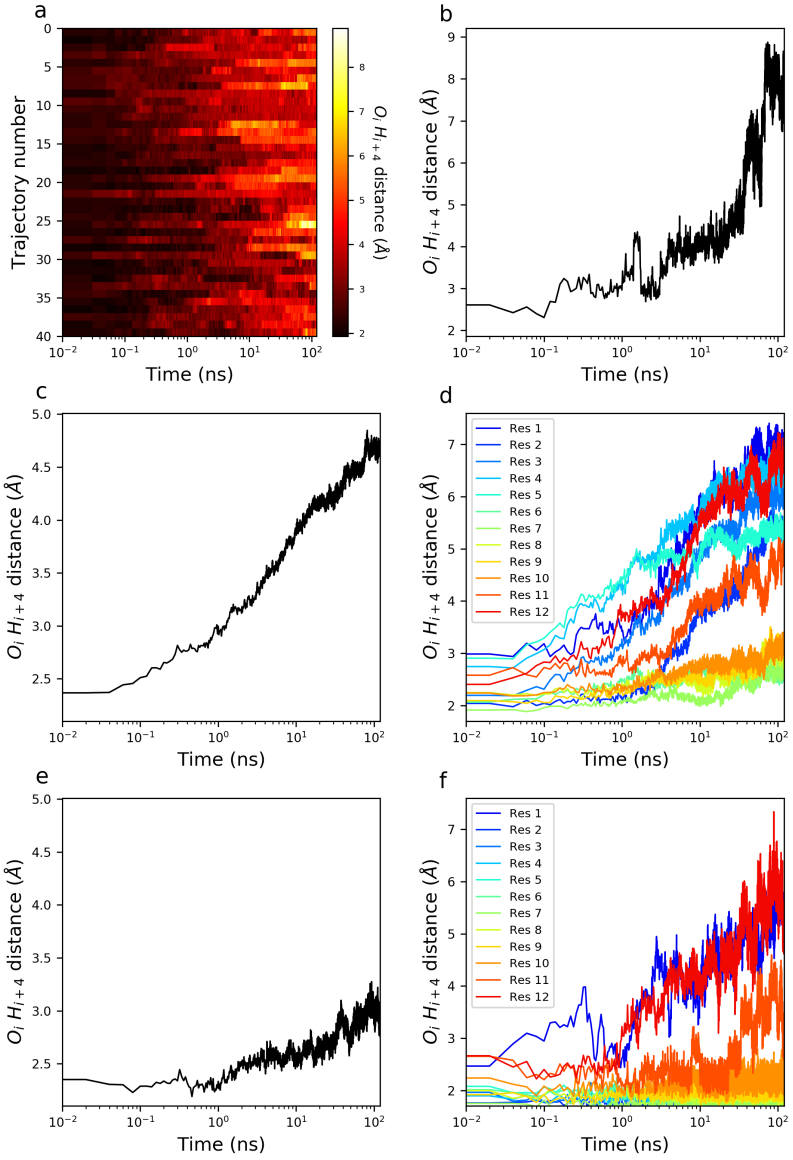


**Figure 4.11: a.** 2D representation of the averaged $O_i$-$H_{i+4}$ distance for each trajectory over time. **b.** Averaged $O_i$-$H_{i+4}$ distance of the trajectory shown in Figure 4.8 over time. **c.** Averaged $O_i$-$H_{i+4}$ distance of the 40 trajectories with the *cis* azo-moiety over time. **d.** Averaged $O_i$-$H_{i+4}$ distance of the 40 trajectories with the *cis* azo-moiety per residue over time. **e.** Averaged $O_i$-$H_{i+4}$ distance of the 10 trajectories with the *trans* azo-moiety over time. **f.** Averaged $O_i$-$H_{i+4}$ distance of the 10 trajectories with the *trans* azo-moiety per residue over time.

representation confirms that the $\alpha$-helix structure of the residues located at the centre of the peptide is more stable than at its termini. Earlier, I presented the hypothesis that the FK-11-X reaches a stable conformation after 40 ns approximately. We see in Figure 4.11d that the $O_i$-$H_{i+4}$ distances of the residues Ala10 to Glu6 continue to increase even after 40 ns. It could mean that the stable conformation shown in Figure 4.7 might be a local minimum and that the peptide will finally unfold completely on a longer time scale. The control simulation is shown in Figures 4.11e and 4.11f, which show the averaged $O_i$-$H_{i+4}$ distances and the averaged $O_i$-$H_{i+4}$ distances, respectively, per residue from the ten trajectories with the *trans* azo-moiety. These two figures show that the termini of the $\alpha$-helix structure are not stable on the nanosecond time scale. However, we see a clear difference between the central residues with the *cis* and with the *trans* azo-moiety, which confirm the impact of the isomerisation of the azo-moiety on the peptide structure.

### 4.2.3 Computed circular dichroism spectra analysis

Here, I will present an analysis based on computed CD spectra. Theoretical CD spectra were calculated using the DichroCalc web interface[96] for individual frames of the simulated trajectories. DichroCalc constructs an exciton Hamiltonian matrix using electronic excitations of the local peptide chromophores. The Hamiltonian models how electronic transitions interact with one another. The sign and magnitude of the interactions depend on the relative orientation and separation of chromophores, which in turn arise from the precise structure of the peptide. For each peptide chromophore two transitions, $n \rightarrow \pi^*$ and $\pi_{nb} \rightarrow \pi^*$, were considered using an ab initio parameter set.[97] Other transitions, such as the $\pi_b \rightarrow \pi^*$ and charge transfer transitions, were not included. The calculated line spectra were convoluted with Gaussian bands of bandwidth 12.5 nm. I calculated the CD spectra of

the structures from MD simulations at 11 different times (0, 0.02, 0.08, 0.2, 0.8, 2, 8, 20, 30, 60, and 120 ns). The spectra of the trajectory illustrated in Figure 4.8 are shown in Figure 4.12.

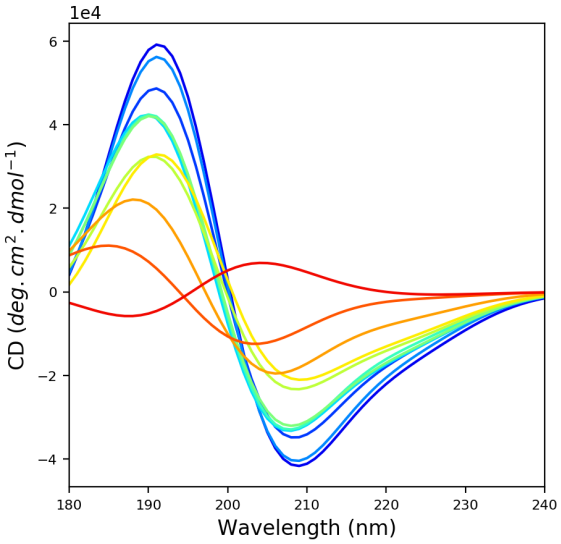


**Figure 4.12:** CD spectra calculated from the trajectory shown in Figure 4.8. The spectra belong to the structures extracted at 0 (blue), 0.02, 0.08, 0.2, 0.8, 2, 8, 20, 30, 60, and 120 ns (red).

The CD spectrum at $t_0$ is close to the spectral signature of an $\alpha$-helix with a positive peak at 190 nm and a negative peak between 200 and 230 nm, centered at 208 nm. Whilst the well-known band at 222 nm appears as a shoulder rather than being more clearly distinct from the 208 nm band, the calculated intensity at 222 nm has been previously shown to be highly correlated with the experimental intensity at that wavelength [97]. The amplitude of the signal decreases progressively over the simulation. I also noticed that the spectrum of the last time frame, at 120 ns, is different. It exhibits a negative peak at 190 nm and a positive peak at 205 nm. This spectrum corresponds to the spectral signature of a random coil. Figure 4.8 shows that the $\alpha$-helix content of the peptide decreases over the simulation and it is completely unfolded after 80 ns. In the literature, the stable conformation of the *cis* FK-11-X peptide has been associated with the conformation at 120 ns in Figure 4.8 [52]. The experimental SRCD spectra of *trans* and the *cis* configuration of FK-11-X

have the same shape but with different amplitudes[98](Figure 4.13b). Thus, the stable conformation of the *cis* FK-11-X is partially helical. If it were not, its CD spectra would correspond to a random coil based structure as the computed CD spectra at 120 ns (Figure 4.12).

In order to analyse results that represent all the trajectories, I averaged the computed CD spectra from the 40 simulations to obtain averaged CD spectra that may be compared to the experimental SRCD spectra in solution. The computed CD spectra at $t = 0$ ns and $t = 120$ ns and the associated averaged spectra are plotted in Figure 4.13a. Approximately 80% of the trajectories populated an ensemble of related structured conformations and the others are between this set of structures and a completely unfolded ensemble. The impact of the helical content on the spectrum is more important than the unfolded structure because the averaged spectrum at 120 ns still corresponds to an $\alpha$-helix.

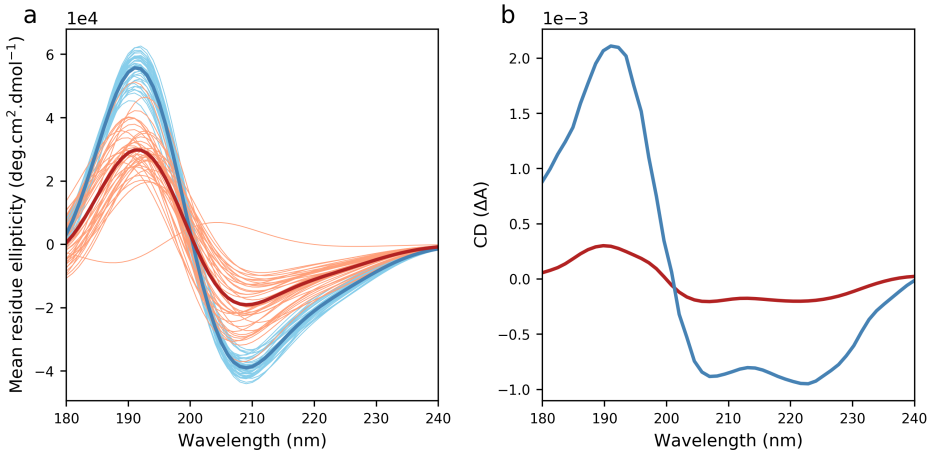


**Figure 4.13: a.** The computed CD spectra of the 40 trajectories from structures extracted at $t = 0$ ns (blue) and $t = 120$ ns (red). The thicker curves correspond to the average spectra. **b.** SRCD spectra of *cis* (red) and *trans* (blue) FK-11-X.[98]

In addition, the SRCD spectra plotted in Figure 4.13b show that the amplitude of the CD signal at 222 nm decreases by 80% when the configuration of the azo-moiety passes from *trans* to *cis*. The same decrease in amplitude of

the averaged CD spectrum computed with the structures at $t = 0$ ns (*trans* configuration) would result in a computed CD spectrum with an amplitude of -3,600 deg cm$^2$ dmol$^{-1}$ at 222 nm. The amplitude of the average of the CD spectra computed with the structures at $t = 120$ ns (*cis* configuration) is -9,800 deg cm$^2$ dmol$^{-1}$ at 222 nm. Thus, it decreases by 46% within the first 120 ns of simulation. The differences may come from either the sampling and could be addressed by increasing the number of trajectories or the duration of the simulation. We observed in Figure 4.11b that the averaged $O_i$-$H_{i+4}$ distance continues to increase at the end of the simulation, so we can expect that the average helical content of the 40 trajectories tends to the value determined experimentally within the next tens of nanoseconds.

In Figure 4.13a we see that in some trajectories, the peptide is in a more advanced unfolding state, in which the CD at 222 nm decreases to -5,000 deg cm$^2$ dmol$^{-1}$, approximately, which corresponds to a decrease of 70%. This estimation is close to the value determined with experimental results and thus the computed structure of the peptide at 120 ns in these trajectories may correspond to the most likely conformation of the FK-11-X in the *cis* configuration. The structures from three of these trajectories are shown in

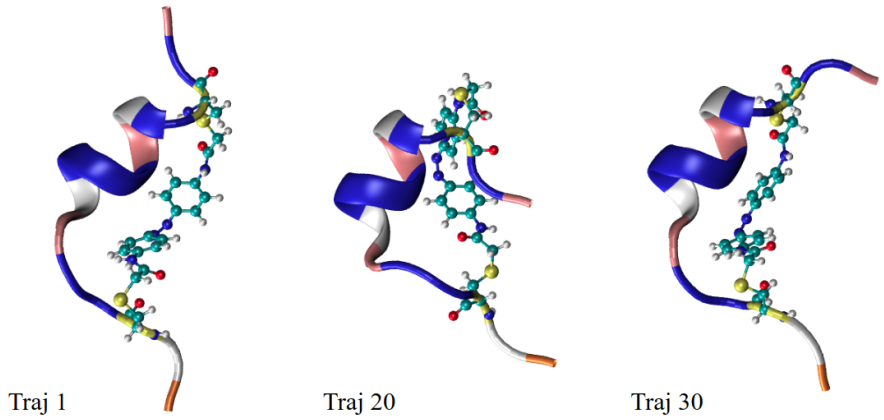


**Figure 4.14:** Structure of the FK-11-X peptide at 120 ns of the trajectories 1, 20 and 30. The colours of the peptide correspond to the amino acid type. Gln, Arg, Cys, Ala and Glu are in orange, white, yellow, blue and pink, respectively.

Figure 4.14. The helical content that remains in these structures is formed by the same residues as the helix shown in Figure 4.7, which include four alanines (Ala-Arg-Glu-Ala-Ala-Ala). Again, it shows the propensity of alanines to stabilise $\alpha$-helix structure.

Chen *et al.*[68] used data from time-resolved ORD experiments to estimate a time constant of $55 \pm 6$ ns (single-exponential decay) for the unfolding process of the FK-11-X peptide. This estimation is based on data points measured from 50 ns to 10 $\mu$s after the trigger of the isomerisation. The lack of information over the first 50 ns leads to a significant over-estimation of the value of the time constant. Based on this time-constant estimation, we can deduce that the dynamics should reach 95% of its total variation after $165 \pm 6$ ns. So, even if this estimation may be too long, it shows that the unfolding process occurs within the first $165 \pm 6$ ns after the isomerisation of the azobenzene. In order to estimate the rate of the unfolding process via the change in CD, I averaged the computed CD spectra from the 40 simulations at 0, 0.02, 0.08, 0.2, 0.8, 2, 8, 20, 30, 60, and 120 ns. The averaged computed CD spectra and the trace of the CD signal at 222 nm are plotted in Figures 4.15a and 4.15b. The average spectra show that the amplitude of the CD signal decreases continuously over the simulation and homogeneously between 180 and 240 nm. In Figure 4.15b, the signal decreases rapidly over the first 20 ns and it starts to stabilise after 20 ns. So we can expect that the signal continues to decrease slightly over the next tens of nanoseconds.

I performed a non-weighted least-squares fitting with a single-exponential decay model of the computed CD signal at 222 nm. The resulting curve is plotted in Figure 4.15b. This fitting allows us to estimate the time-constant of the simulated unfolding process at $\tau$=5.80±0.03 ns. Because we see that the computed CD signal seems to not reach a plateau at the end of the simulation,

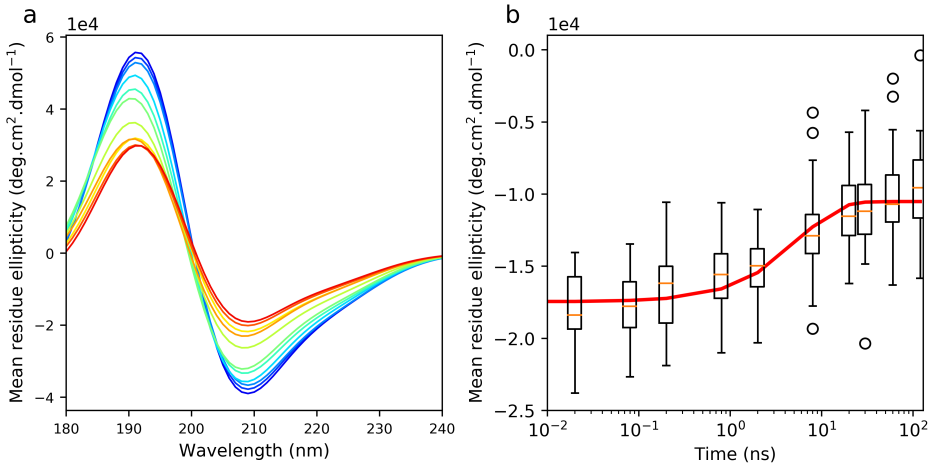


**Figure 4.15: a.** Averaged CD spectra of the 40 trajectories from structures extracted at 0 (blue), 0.02, 0.08, 0.2, 0.8, 2, 8, 20, 30, 60, and 120 ns (red). **b.** Trace of the computed CD signal at 222 nm. The boxes extend from the first to the third quartile values of the data, with a horizontal red line at the median. The whiskers attached to the boxes extend to the extrema of the data. If the whiskers are 50% longer than the difference between the first and the third quartile values, then the outer data points are represented as circles. The red curve is a non-weighted least-squares fitting with a single-exponential decay model with a time constant of $\tau$=5.80±0.03 ns.

this may be an under-estimate and could be refined with longer simulations. The final slower decrease in amplitude expected after 120 ns should make the loss of amplitude at 222 nm approach 80%, the value that I deduced from experimental data. These results show that the rate of the simulated unfolding process is consistent with that provided by time-resolved ORD experiments.

Khuc *et al.*[99] performed quantitative time-resolved CD measurement with a time step of 12 ns at 225 nm. They successfully estimated the variation of the helical fraction of a poly(glutamic acid) peptide over a T-jump experiment using a nanosecond Nd:YAG laser to heat up the solvent and a sub-picosecond source based on a 1 kHz amplified Titanium-Sapphire system for the CD measurement[46]. Dartigalongue *et al.*[46] used this light source to perfom sub-picosecond measurements to assess the change in CD over the photodissociation of carbonmonoxy-myoglobin. Thus, time-resolved pump-probe CD measurements with either sub-picosecond or nanosecond temporal

resolution on the FK-11-X peptide using this approach would bring further information which would complement the model that I propose here.

## 4.3 Conclusion

In this chapter, I investigated the unfolding of the FK-11-X peptide based on a computational approach. I optimised a force field for the azo-moiety to ensure that this part of the FK-11-X peptide is parameterised well and in an internally consistent fashion. Using this force field, I computed 40 MD trajectories of 120 ns simulating the unfolding process of the FK-11-X peptide. Approximately 80% of the trajectories presented a partially unfolded peptide with a similar conformation at the end of the simulation. The remaining 20% were in a more advanced unfolded state and in one trajectory the peptide was completely unfolded. I analysed the dynamics of the process looking at the distance between the two sulfur atoms and the $O_i$-$H_{i+4}$ backbone hydrogen bond distances. The S-S distance decreases progressively during the first 10 ns and then is stable until the end of the simulation. The $O_i$-$H_{i+4}$ distances and the structure of the peptide at 120 ns indicated that the three alanines located between the two cysteines significantly stabilise the $\alpha$-helix. We also see that the termini of the FK-11-X helix are quite labile on the nanosecond timescale, even in the *trans* configuration. The amino acids at the termini unfold progressively over the first 100 ns. An analysis of CD spectra computed from snapshots from the MD simulations allowed us to compare the dynamics of the simulated unfolding process and the experimental data. The calculated CD signal at 222 nm reaches a plateau at the end of the simulation. The $55 \pm 6$ ns time constant proposed by Chen *et al.* allows us to estimate that 95% of the reaction would occur within $165 \pm 6$ ns. This estimate matches well with the rate of the simulated dynamics. I also used the variation of the

CD signal at 222 nm from experimental data and from the calculated spectra to demonstrate that the most likely stable conformation of the *cis* FK-11-X is not the fully unfolded conformation but a conformation close to the structure shown in Figure 4.14.

# 5 Conclusion

This thesis work was partly dedicated to the development of a time-resolved SRCD setup at the DISCO beamline. I proposed a novel approach that uses the natural polarisation of the synchrotron radiation to measure CD signals. I developed a spectrography setup that allows one to measure the intensity of the two parts of the beam simultaneously on a broad spectral range. I developed two configurations of the tr-SRCD setup with two different detection systems. The first configuration uses a CMOS detector, which provides a high SNR but it is limited with respect to the temporal resolution. The second configuration is based on the combination of an image intensifier and a CMOS detector, which allows one to perform real time measurement with sub-microsecond temporal resolution and single pulse measurements. These two configurations are complementary and make the tr-SRCD setup versatile. In Section 2.2.1, I presented the protocols that could be used with the two configurations allowing one to follow dynamics on a wide time range spanning from nanoseconds to minutes. I developed a method to perform polarimetry measurements to assess the circularity of the light incoming on each pixel of the detector. It allowed me to avoid artifacts described in Section 2.2.6.1 by limiting the intensity measurement to pixels that are suitable for CD measurements. In Section 3.1, I presented results based on the enantiomers of the CSA. I demonstrated that one can obtain reliable CD spectra using the natural elliptical polarisation. I shown that the tr-SRCD setup allows one to measure a CD spectrum in only one measurement with a SNR above 3. I also shown that a SNR $> 40$ can be reached by averaging 100 images acquired within 5 seconds. In section 3.1.2, I presented my first time-resolved experiment in which I followed CD variation with a sub-microsecond temporal resolution using the combination of the image intensifier and the camera. I also used this configuration to perform

steady-state single pulse measurements with picosecond temporal resolution. These three results with the CSA allowed me to demonstrate the reliability of the presented acquisition protocols. In section 3.2, I presented my first results on a biological system, the FK-11-X peptide. This molecule is photoswitchable; one can induce changes in the structure of the peptide by isomerisation the azo-benzene cross-linker with an appropriated irradiation. I shown that the tr-SRCD setup allowed me to follow changes in concentration of the two FK-11-X isomers with a 520 $\mu$s temporal resolution and with an acquisition rate of 130 Hz. All the experimental results presented in Section 3.1 and 3.2 are based on relative measurements. I explained in Section 2.2.6 that the use of the natural polarisation indirectly makes the tr-SRCD setup more sensitive to artifacts brought about by the light scattering and by the shifts of the beam optical path. In Section 2.2.7, I propose an alternative approach that aims to substitute the natural polarisation and to remove partly the two main sources of artifact. I used polarising optical components to control the polarisation of the beam. This approach has several advantages. With this method, it is not necessary to filter the beam projection via a selection of pixels, the polarisation is highly circular on the whole spectral range of interest, the polarisation imperfections can be corrected and one can measure a CD spectra without the need of a reference intensity. Because the measurement with this method is much less affected by the artifacts, I expected that it allows one to perform absolute CD measurement. In section 3.3, I compared absolute CD spectra of folded and unfolded DNA structures namely a G-quadruplex recorded with the conventional SRCD setup, the tr-SRCD setup using natural polarisation and the tr-SRCD setup using polarising components. The results show that the absolute CD spectra recorded with the tr-SRCD setup using the natural polarisation are highly convoluted but the relative spectra correspond to the reference measured with the conventional SRCD setup. It shows that the use

of the natural polarisation is only suitable for relative measurements. Despite the presence of a slight baseline, the absolute CD spectra recorded sequentially with the tr-SRCD setup using polarising optical components matches well with the SRCD spectra. These results also show that the amplitude of the CD signal is approximately six times larger using polarising optical components compared to using natural polarisation. This difference would improve significantly the SNR of the measurements as well as the capacity of the tr-SRCD setup to measure smaller signals. To conclude the experimental part of this thesis, I demonstrated that one can use the natural polarisation of the synchrotron to record relative CD spectra with a temporal resolution up to 89 ps. The tr-SRCD also allows one to record steady-state CD spectra with an acceptable SNR between 190 nm and 320 nm in only one measurement with an integration time of 520 $\mu$s. Finally, I proposed an alternative approach that could improve the tr-SRCD by allowing the measurement of absolute CD spectra and by increasing significantly the SNR. The performance of the tr-SRCD setup might represent a breakthrough in SRCD spectroscopy. It is the first time that a picosecond resolution is accessible on this spectral range. In addition, one do not need to combine the tr-SRCD with a microfluidic device to reach this temporal resolution, so the measurement does not have dead time. This improvement is particularly interesting because this high temporal resolution will allow the study of dynamics occurring on the nanosecond time scale. It fills the gap that existed between the time ranges accessible with theoretical approaches and those accessible with experimental approaches. The FK-11-X peptide is a good example. Its unfolding process occurs on the nanosecond time scale. Now, it can be studied with the tr-SRCD setup using an appropriate laser to trigger the dynamics. It can also be studied through MD simulation and computed CD spectra. I presented in Chapter 4 a study of the FK-11-X unfolding process via a theoretical approach. First, I developed an improved

force field for the azo-moiety. I triggered the isomerisation of the azo-benzene via a potential energy approach. I generated 50 MD trajectories of 120 ns, including 10 trajectories used as a control where the azo-benzene was kept in its *trans* configuration. I used several tools to assess the progression of the unfolding process over the trajectory, such as the Ramachandran plot and the quantification of typical distances (S-S and $O_i$-$H_{i+4}$). It appeared that the structure of the peptide starts to unfold after $\approx$ 20 ps and, in $\approx$ 80% of the cases, it reaches a stable conformation partially unfolded after approximately 50 ns. I also found that in some trajectories, the peptide is totally unfolded after 120 ns. I augmented these results with an analysis based on computed spectra (Section 4.2.2). I calculated CD spectra with Dichrocalc using an ab initio parameter set. The CD spectra were calculated from the structures of the MD simulations. I first analysed the spectra of a trajectory in which the peptide is totally unfolded after 120 ns. I noticed that the spectrum corresponding to the unfolded structure did not correspond to the spectra of a solution of *cis* azobenzene presented in the literature. I averaged the spectra of the 40 trajectories to have an estimation of the CD spectra of a solution by taking into account the different pathways. I observed that the difference in CD at 222 nm between the computed spectra of the initial ($t = 0$ ns) and the final structures ($t = 120$ ns) was $\approx$ 80% of the variation found experimentally. I also estimated the time-constant of the simulated unfolding process at  =5.80$\pm$0.03 ns by analysing the trace of the CD signal at 222 nm. This value is is consistent the value of $\approx$ 55 ns determined experimentally via time-resolved ORD spectroscopy. These two results validate the reliability of the optimised force field. This work allowed me to conclude that the unfolded conformation is not the most likely conformation of the *cis* FK-11-X in solution and that the trajectory sampling of MD simulation can be consistent with the observed experimental data. In the near future one might be able to

compare computed CD spectra of MD simulation structures with transient spectra recorded with the tr-SRCD setup. The combination of MD simulation, CD spectra computation and the tr-SRCD setup might allow one to associate structures to transient SRCD spectra.

# 6 Future Work

The results presented in this thesis show that the natural polarisation of the synchrotron radiation makes possible single pulse CD spectra measurements in the UV range. However, I have shown that this approach is limited to relative CD measurements and that it involves several important biases. Thus, I believe that it would be more efficient to use all the other synchrotron radiation features (temporal distribution, pulse width, spectral range, brilliance) coupled to polarising optical components rather than using the natural polarisation. To do this, several modifications of the tr-SRCD setup would be necessary to simultaneously measure the transmitted intensity of two separated beams. The initial beam could be split into two parts with identical intensity with a combination of two rochon polarisers ($MgF_2$). The first polariser polarises linearly the initial beam and the second, oriented at 45° from the first polariser, splits it into two identical parts. The two outgoing beams could be polarised circularly with opposite orientation using two achromatic QWPs ($MgF_2$). The important point is to ensure that the two parts have identical reflections along the optical bench to conserve similar polarisation states. In addition, a second major issue that limits significantly the efficiency of the tr-SRCD setup comes from the response of the detectors. Indeed, the sensitivity of the detectors decreases drastically as the wavelength of the detected photon goes shorter. So, it is not possible to maximize simultaneously the number of photons that are detected at all the wavelengths. The photon flux of the beamline and the sensitivity of the detector determine the wavelength at which the optimisation of the integration time of the camera must be made. The ratio between the number of photon detected at this wavelength and the number of photons detected at 180 nm is comprised between 100 and 1000. This low amount of light detected on the shorter wavelengths range induces a low SNR in the

measurements. It is possible to avoid this issue by flattening the response of the detector. This could be made by using a customized spectral filter or by placing an adapted neutral density filter after the imaging grating of the spectrograph. I think that these two modifications are the priority for the development of this technique and that they should enhance significantly the results obtained with the tr-SRCD setup.

# References

[1] F. Arago. Mémoire sur une modification remarquable qu'éprouvent les rayons lumineux dans leur passage à travers certains corps diaphanes et sur quelques autres nouveaux phénomènes d'optique. *Mémoires de la classe des sciences mathématiques et physiques de l'Institut Impérial de France*, pages 93–134, 1811.

[2] J. B. Biot. Phénomènes de polarisation successive, observés dans des fluides homogènes. *Bull. Soc. Philomath*, (190), 1815.

[3] J. B. Biot. Extrait d'un mémoire sur les rotations que certaines substances impriment aux axes de polarisation des rayons lumineux. *Ann. chem. et phys.*, (2):372–389, 1818.

[4] A. Fresnel. Mémoire sur la double réfraction particulière que présente le cristal de roche dans la direction de son axe. *op. cit. in.*, page 744, 1866.

[5] A. Cotton. Absorption inégale des rayons circulaires droit et gauche dans certains corps actifs. *Comptes Rendus Acad. Sci.*, (120):989–991, 1895.

[6] R. C. Jones. A new calculus for the treatment of optical systemsi. description and discussion of the calculus. *J. Opt. Soc. Am.*, (31):488–493, 1941.

[7] G. G. Stokes. On the composition and resolution of streams of polarized light from different sources. *Trans. Cambridge Philos. Soc.*, (9):399, 1851.

[8] N. J. Greenfield. Using circular dichroism spectra to estimate protein secondary structure. *Nat. Protoc.*, (6):2876, 2006.

[9] S. M. Kelly, T. J. Jess, and N. C. Price. How to study proteins by circular dichroism. *Biochim. Biophys. Acta BBA*, (2):119–139, 2005.

[10] W. C. Johnson Jr. Secondary structure of proteins through circular dichroism spectroscopy. *Annu. Rev. Biophys. Biophys. Chem.*, (1):145–166, 1988.

[11] G. Holzwarth and P. Doty. The ultraviolet circular dichroism of polypeptides. *J. Am. Chem. Soc.*, (2):218–228, 1965.

[12] E. H. Strickland and S. Beychok. Aromatic contributions to circular dichroism spectra of protein. *CRC Crit. Rev. Biochem.*, (1):113–175, 1974.

[13] P. C. Kahn. The interpretation of near-ultraviolet circular dichroism. *Method. Enzymol.*, pages 339–378, 1979.

[14] P. O. Freskgaard, L. G. Maartensson, P. Jonasson, B. H. Jonsson, and U. Carlsson. Assignment of the contribution of the tryptophan residues to the circular dichroism spectrum of human carbonic anhydrase ii. *Biochemistry*, (47):14281–14288, 1994.

[15] S. Vuilleumier, J. Sancho, R. Loewenthal, and A. R. Fersht. Circular dichroism studies of barnase and its mutants: characterization of the

contribution of aromatic side chains. *Biochemistry*, (39):10303–10313, 1993.

[16] F. U. Hartl. Protein misfolding diseases. *Annu. Rev. Biochem.*, (86): 21–26, 2017.

[17] B.A. Wallace and R.W. Janes. Modern techniques for circular dichroism and synchrotron radiation circular dichroism spectroscopy. 2009.

[18] P. A. Snyder and E. M. Rowe. The first use of synchrotron radiation for vacuum ultraviolet circular dichroism measurements. *Nucl. Instrum. Methods*, (172):345–349, 1980.

[19] J. C. Sutherland, E. J. Desmond, and P. Z. Takacs. Versatile spectrometer for experiments using synchrotron radiation at wave-lengths greater than 100 nm. *Nucl. Instrum. Methods*, (172):195–199, 1980.

[20] B. A. Wallace. Protein characterisation by synchrotron radiation circular dichroism spectroscopy. *J. Synchrotron Radiat.*, 7(5):289–295, 2000.

[21] B. A. Wallace. Synchrotron radiation circular-dichroism spectroscopy as a tool for investigating protein structures. *Q. Rev. Biophys*, (42):317–370, 2009.

[22] B. M. Bulheller, A. J. Miles, B. A. Wallace, and J. D. Hirst. Charge-transfer transitions in the vacuum-ultraviolet of protein circular dichroism spectra. *J. Phys. Chem. B*, (112):1866–1874, 2008.

[23] K. Matsuo, R. Yonehara, and K. Gekko. Secondary-structure analysis of proteins by vacuum-ultraviolet circular dichroism spectroscopy. *J. Biochem.*, (135):405–411, 2004.

[24] P. Evans, K. Wyatt, G. J. Wistow, O. A. Bateman, B. A. Wallace, and C. Slingsby. The p23t cataract mutation causes loss of solubility of folded d-crystallin. *J. Mol. Biol.*, (343):435–444, 2004.

[25] L. Day, J. Zhai, M. Xu, N. C. Jones, S. V. Hoffmann, and T. J. Wooster. Conformational changes of globular proteins adsorbed at oil-in-water emulsion interfaces examined by synchrotron radiation circular dichroism. *Food Hydrocoll.*, 34:78–87, 2014.

[26] A. J. Miles and B. A. Wallace. Synchrotron radiation circular dichroism spectroscopy of proteins and applications in structural and functional genomics. *Chem. Soc. Rev.*, (35):39–51, 2006.

[27] K. Pande, C. D. Hutchison, G. Groenhof, A. Aquila, J. S. Robinson, J. Tenboer, ..., and T. A. White. Femtosecond structural dynamics drives the trans/cis isomerization in photoactive yellow protein. *Science*, 352 (6286):725–729, 2016.

[28] K. Lindorff-Larsen, N. Trbovic, P. Maragakis, S. Piana, and D. E. Shaw. Structure and dynamics of an unfolded protein examined by molecular dynamics simulation. *J. Am. Chem. Soc.*, 134(8):3787–3791, 2012.

[29] H. Kim and M. Cho. Infrared probes for studying the structure and dynamics of biomolecules. *Chem. Rev.*, 113(8):5817–5847, 2013.

[30] M. Hong, Y. Zhang, and F. Hu. Membrane protein structure and dynamics from nmr spectroscopy. *Annu. Rev. Phys. Chem.*, 63:1–24, 2012.

[31] J. R. Lewandowski, M. E. Halse, M. Blackledge, and L. Emsley. Direct observation of hierarchical protein dynamics. *Science*, 348(6234):578–581, 2015.

[32] F. A. Ferrone, J. J. Hopfield, and S. E. Schnatterly. The measurement of transient circular dichroism: A new kinetic technique. *Rev. Sci. Instrum.*, (45):1392–1396, 1974.

[33] P. M. Bayley and M. Anson. Stopped-flow circular dichroism: A new fast-kinetic system. *Biopolymers*, (13):401–405, 1974.

[34] M. Anson, S. R. Martin, and P. M. Bayley. Transient cd measurements at submillisecond time resolution—application to studies of temperature-jump relaxation of equilibria of chiral biomolecules. *Rev. Sci. Instrum.*, (48):953–962, 1977.

[35] S. Akiyama, S. Takahashi, K. Ishimori, and I. Morishima. Stepwise formation of -helices during cytochrome c folding. *Nat. Struct. Mol. Biol.*, (7):514, 2000.

[36] J. D. Xie, X.and Simon. Picosecond time-resolved circular dichroism spectroscopy: experimental details and applications. *Rev. Sci. Instrum.*, (60):2614–2627, 1989.

[37] T. Dartigalongue and F. Hache. Precise alignment of a longitudinal pockels cell for time-resolved circular dichroism experiments. *J. Opt. Soc. Am. B*, (20):1780–1787, 2003.

[38] C. Niezborala and F. Hache. Measuring the dynamics of circular dichroism in a pump-probe experiment with a babinet-soleil compensator. *J. Opt. Soc. Am.*, (23):2418–2424, 2006.

[39] F. Hache. Application of time-resolved circular dichroism to the study of conformational changes in photochemical and photobiological processes. *J. Photochem. Photobiol. A*, (204):137–143, 2009.

[40] J. W. Lewis, R. F. Tilton, C. M. Einterz, S. J. Milder, I. D. Kuntz, and D. S. Kliger. New technique for measuring circular dichroism changes on a nanosecond time scale. application to (carbonmonoxy) myoglobin and (carbonmonoxy) hemoglobin. *J. Phy. Chem.*, (89):289–294, 1985.

[41] C. F. Zhang, J. W. Lewis, R. Cerpa, I. D. Kuntz, and D. S. Kliger. Nanosecond circular dichroism spectral measurements: extension to the far-ultraviolet region. *J. Phy. Chem.*, (97):5499–5505, 1993.

[42] Y. X. Wen, E. Chen, J. W. Lewis, and D. S. (1996) Kliger. Nanosecond time-resolved circular dichroism measurements using an upconverted ti: sapphire laser. *Rev. Sci. Instrum.*, (67):3010–3016, 1996.

[43] I. Eom, S. H. Ahn, H. Rhee, and M. Cho. Single-shot electronic optical activity interferometry: power and phase fluctuation-free measurement. *Phys. Rev. Lett.*, (108):103901, 2012.

[44] K. Hiramatsu and T. Nagata. Communication: Broadband and ultrasensitive femtosecond time-resolved circular dichroism spectroscopy. *J. Chem. Phys.*, (143):121102, 2015.

[45] T. Dartigalongue and F. Hache. Observation of sub-100 ps conformational changes in photolyzed carbonmonoxy-myoglobin probed by time-resolved circular dichroism. *Chem. Phys. Lett.*, (415):313–316, 2005.

[46] T. Dartigalongue, C. Niezborala, and F. Hache. Subpicosecond uv spectroscopy of carbonmonoxy-myoglobin: absorption and circular dichroism studies. *Phys. Chem. Chem. Phys.*, (9):1611–1615, 2007.

[47] A. Trifonov, I. Buchvarov, A. Lohr, F. Würthner, and T. Fiebig. Broadband femtosecond circular dichroism spectrometer with white-light polarization control. *Rev. Sci. Instrum.*, (81):043104, 2010.

[48] M. Oppermann, B. Bauer, T. Rossi, F. Zinna, J. Helbing, J. Lacour, and M. Chergui. Ultrafast broadband circular dichroism in the deep ultraviolet. *Optica*, (6):56–60, 2019.

[49] A. S. Kane, A. Hoffmann, P. Baumgartel, R. Seckler, G. Reichardt, B. Horsley, D. A.and Schuler, and O. Bakajin. Microfluidic mixers for the investigation of rapid protein folding kinetics using synchrotron radiation circular dichroism spectroscopy. *Anal. Chem.*, (80):9534–9541, 2008.

[50] D. T. Clarke, A. J. Doig, B. J. Stapley, and G. R. Jones. The $\alpha$-helix folds on the millisecond time scale. *Proc. Natl. Acad. Sci. USA*, (96): 7232–7237, 1999.

[51] U. Heinzmann, B. Osterheld, and F. Schäfers. Measurements and calculations of the circular polarization and of the absolute intensity of synchrotron radiation in the wavelength range from 40 to 100 nm. *Nucl. Instrum. Methods Phys. Res.*, (195):395–398, 1982.

[52] D. G. Flint, J. R. Kumita, O. S. Smart, and G. A. Woolley. Using an azobenzene cross-linker to either increase or decrease peptide helix content upon trans-to-cis photoisomerization. *Chem. Biol.*, (9):391–397, 2002.

[53] X. Xing, X. Wang, L. Xu, Y. Tai, L. Dai, X. Zheng, ..., and X. Zhou. Light-driven conformational regulation of human telomeric g-quadruplex dna in physiological conditions. *Org. Biomol. Chem.*, (9):6639–6645, 2011.

[54] A. Giuliani, F. Jamme, V. Rouam, F. Wien, J. L. Giorgetta, B. Lagarde, ..., and M. Réfrégiers. Disco: a low-energy multipurpose beamline at synchrotron soleil. *J. Synchr. Rad.*, (16):835–841, 2009.

[55] M. Réfrégiers, F. Wien, H. P. Ta, L. Premvardhan, S. Bac, F. Jamme, ..., and A. Giuliani. Disco synchrotron-radiation circular-dichroism endstation at soleil. *J. Synchr. Rad.*, (19):831–835, 2012.

[56] F. Jamme, S. Villette, A. Giuliani, V. Rouam, F. Wien, B. Lagarde, and M. Réfrégiers. Synchrotron uv fluorescence microscopy uncovers new probes in cells and tissues. *Microsc. Microanal.*, (16):507–514, 2010.

[57] A. Giuliani, I. Yao, B. Lagarde, S. Rey, J. P. Duval, P. Rommeluere, ..., and M. Ros. A differential pumping system to deliver windowless vuv photons at atmospheric pressure. *J. Synchr. Rad.*, (18):546–549, 2011.

[58] B. S. Kang, P. Fischer, D. H. Kim, D. Attwood, E. Anderson, and G. Cho. Bending magnet x-ray polarization modulation for magnetic full field soft x-ray transmission microscopy. *Proc. 8th Int. Conf. X-ray Microscopy. IPAP Conf. Series.*, (7):288–290, 2006.

[59] J. W. Lewis, R. A. Goldbeck, D. S. Kliger, X. Xie, R. C. Dunn, and J. D. Simon. Time-resolved circular dichroism spectroscopy: experiment, theory, and applications to biological systems. *J. Phys. Chem.*, (96): 5243–5254, 1992.

[60] A. J. Miles, F. Wien, and B. A. Wallace. Redetermination of the extinction coefficient of camphor-10-sulfonic acid, a calibration standard for circular dichroism spectroscopy. *Anal. Biochem.*, (335):338–339, 2004.

[61] G. A. Woolley. Photocontrolling peptide $\alpha$ helices. *Acc. Chem. Res.*, (38): 486–493, 2005.

[62] J. R. Kumita, O. S. Smart, and G. A. Woolley. Photo-control of helix content in a short peptide. *Proc. Natl. Acad. Sci. USA*, (97):3803–3808, 2000.

[63] A. Nenov, R. Borrego-Varillas, A. Oriana, L. Ganzer, F. Segatta, I. Conti, ..., and C. Manzoni. Uv-light-induced vibrational coherences: the key to understand kasha rule violation in trans-azobenzene. *J. Phys. Chem. Lett.*, (9):1534–1541, 2018.

[64] T. Nägele, R. Hoche, W. Zinth, and J. Wachtveitl. Femtosecond photoisomerization of cis-azobenzene. *Chem. Phys. Lett.*, (272):489–495, 1997.

[65] T. Fujino and T. Tahara. Picosecond time-resolved raman study of trans-azobenzene. *J. Phys. Chem. A*, (104):4203–4210, 2000.

[66] T. Fujino, S. Y. Arzhantsev, and T. Tahara. Femtosecond time-resolved fluorescence study of photoisomerization of trans-azobenzene. *J. Phys. Chem. A*, (105):8123–8129, 2001.

[67] S. H. Xia, G. Cui, W. H. Fang, and W. Thiel. How photoisomerization drives peptide folding and unfolding: Insights from qm/mm and mm dynamics simulations. *Angew. Chem. Int. Ed.*, (55):2067–2072, 2016.

[68] E. Chen, J. R. Kumita, G. A. Woolley, and D. S. Kliger. The kinetics of helix unfolding of an azobenzene cross-linked peptide probed by nanosecond time-resolved optical rotatory dispersion. *J. Am. Chem. Soc.*, (125):12443–12449, 2003.

[69] A. T. Phan, V. Kuryavyi, K. N. Luu, and D. J. Patel. Structure of two intramolecular g-quadruplexes formed by natural human telomere sequences in k+ solution. *Nucleic Acids Res.*, (35):6517–6525, 2007.

[70] K. N. Luu, A. T. Phan, V. Kuryavyi, L. Lacroix, and D. J. Patel. Structure of the human telomere in k+ solution: an intramolecular (3+ 1) g-quadruplex scaffold. *J. Am. Chem. Soc.*, (128):9963–9970, 2006.

[71] G. Biffi, D. Tannahill, J. McCafferty, and S. Balasubramanian. Quantitative visualization of dna g-quadruplex structures in human cells. *Nat. Chem.*, (5):182, 2013.

[72] X. Wang, J. Huang, Y. Zhou, S. Yan, X. Weng, X. Wu, ..., and X. Zhou. Conformational switching of g-quadruplex dna by photoregulation. *Angew. Chem. Int. Ed.*, (49):5305–5309, 2010.

[73] N. Hildebrand, M. Michaelis, N. Wurzler, Z. Li, J. D. Hirst, A. Micsonai, ..., and M. Delle Piane. Atomistic details of chymotrypsin conformational changes upon adsorption on silica. *ACS Biomater. Sci. Eng.*, (4):4036–4050, 2018.

[74] M. Michaelis, N. Hildebrand, R. H. Meißner, N. Wurzler, Z. Li, J. D. Hirst, ..., and L. Colombi Ciacchi. Impact of the conformational variability of oligopeptides on the computational prediction of their cd spectra. *J. Phys. Chem. B*, (123):6694–6704, 2019.

[75] M. D. Hanwell, D. E. Curtis, D. C. Lonie, T. Vandermeersch, E. Zurek, and G. R. Hutchison. Avogadro: an advanced semantic chemical editor, visualization, and analysis platform. *J. Cheminformatics*, (4):17, 2012.

[76] W. Humphrey, A. Dalke, and K. Schulten. Vmd: visual molecular dynamics. *J. Mol. Graph.*, (14):33–38, 1996.

[77] W. L. Jorgensen, J. Chandrasekhar, J. D. Madura, R. W. Impey, and M. L. Klein. Comparison of simple potential functions for simulating liquid water. *J. Chem. Phys.*, (79):926–935, 1983.

[78] J. C. Phillips, R. Braun, W. Wang, J. Gumbart, E. Tajkhorshid, E. Villa, ..., and K. Schulten. Scalable molecular dynamics with namd. *J. Comput. Chem.*, (26):1781–1802, 2005.

[79] A. D. MacKerell Jr, D. Bashford, M. L. D. R. Bellott, R. L. Dunbrack Jr, J. D. Evanseck, M. J. Field, ..., and D. Joseph-McCarthy. All-atom empirical potential for molecular modeling and dynamics studies of proteins. *J. Phys. Chem.*, (102):3586–3616, 1998.

[80] A. D. MacKerell Jr, M. Feig, and C. L. Brooks. Improved treatment of the protein backbone in empirical force fields. *J. Am. Chem. Soc.*, (126): 698–699, 2003.

[81] R. B. Best, X. Zhu, J. Shim, P. E. Lopes, J. Mittal, M. Feig, and A. D. MacKerell Jr. Optimization of the additive charmm all-atom protein force field targeting improved sampling of the backbone $\phi$, $\psi$ and side-chain $\chi^1$ and $\chi^2$ dihedral angles. *J. Chem. Theory Comput.*, (8):3257–3273, 2012.

[82] H. Carstens. Konformationsdynamik lichtschaltbarer peptide: Molekulardynamiksimulationen und datengetriebene modellbildung [conformational dynamics of photoswitchable peptides: Molecular dynamics and data-driven model building]. phd thesis (ludwig maximilians universität münchen, munich). available at: http://edoc.ub.uni-muenchen.de/2268. 2004. URL http://edoc.ub.uni-muenchen.de/2268.

[83] M. Böckmann, C. Peter, L. D. Site, N. L. Doltsinis, K. Kremer, and D. Marx. Atomistic force field for azobenzene compounds adapted for qm/mm simulations with applications to liquids and liquid crystals. *J. Chem. Theory Comput.*, (3):1789–1802, 2007.

[84] K. Vanommeslaeghe and A. D. MacKerell Jr. Automation of the charmm general force field (cgenff) i: bond perception and atom typing. *J. Chem. Inf. Model.*, (52):3144–3154, 2012.

[85] K. Vanommeslaeghe, E. Hatcher, C. Acharya, S. Kundu, S. Zhong, J. Shim, ..., and A. D. MacKerell Jr. Charmm general force field: A force field for drug-like molecules compatible with the charmm all-atom additive biological force fields. *J. Comput. Chem.*, (31):671–690, 2010.

[86] J. Bredenbeck, J. Helbing, J. R. Kumita, G. A. Woolley, and P. Hamm. $\alpha$-helix formation in a photoswitchable peptide tracked from picoseconds to microseconds by time-resolved ir spectroscopy. *Proc. Natl. Acad. Sci. USA*, (102):2379–2384, 2005.

[87] J. A. Ihalainen, J. Bredenbeck, R. Pfister, J. Helbing, L. Chi, I. H. van Stokkum, ..., and P. Hamm. Folding and unfolding of a photoswitchable peptide from picoseconds to microseconds. *Proc. Natl. Acad. Sci. USA*, (104):5383–5388, 2007.

[88] Y. Shao, Z. Gan, E. Epifanovsky, A. T. Gilbert, M. Wormit, J. Kussmann, ..., and D. Ghosh. Advances in molecular quantum chemistry contained in the q-chem 4 program package. *Mol. Phys.*, (113):184–215, 2015.

[89] S. E. Feller, R. W. Pastor, A. Rojnuckarin, S. Bogusz, and B. R. Brooks. Effect of electrostatic force truncation on interfacial and transport properties of water. *J. Phys. Chem.*, 100(42):17011–17020, 1996.

[90] S. Miyamoto and P. A. Kollman. Settle: An analytical version of the shake and rattle algorithm for rigid water models. *J. Comput. Chem.*, 13 (8):952–962, 1992.

[91] J. P. Ryckaert, G. Ciccotti, and H. J. Berendsen. Numerical integration of the cartesian equations of motion of a system with constraints: molecular dynamics of n-alkanes. *J. Comput. Phys.*, 23(3):327–341, 1977.

[92] B. Paoli, M. Seeber, E. H. Backus, J. A. Ihalainen, P. Hamm, and A. Caflisch. Bulky side chains and non-native salt bridges slow down the folding of a cross-linked helical peptide: a combined molecular dynamics and time-resolved infrared spectroscopy study. *J. Phys. Chem. B*, (113): 4435–4442, 2009.

[93] E. J. Spek, C. A. Olson, Z. Shi, and N. R. Kallenbach. Alanine is an intrinsic $\alpha$-helix stabilizing amino acid. *J. Am. Chem. Soc.*, (121): 5571–5572, 1999.

[94] S. A. Hollingsworth and P. A. Karplus. A fresh look at the ramachandran plot and the occurrence of standard structures in proteins. *Biomol. Concepts*, (1):271–283, 2010.

[95] J. D. Hirst and C. L. Brooks III. Molecular dynamics simulations of isolated helixes of myoglobin. *Biochemistry*, (34):7614–7621, 1995.

[96] B. M. Bulheller and J. D. Hirst. Dichrocalc—circular and linear dichroism online. *Bioinformatics*, (25):539–540, 2009.

[97] N. A. Besley and J. D. Hirst. Theoretical studies toward quantitative protein circular dichroism calculations. *J. Am. Chem. Soc.*, (121):9636–9644, 1999.

[98] F. Auvray, D. Dennetiere, A. Giuliani, F. Jamme, F. Wien, B. Nay, S. Zirah, F. Polack, C. Menneglier, B. Lagarde, J. D. Hirst, and M. Réfrégiers. Time resolved transient circular dichroism spectroscopy using synchrotron natural polarization. *Struct. Dynam.*, 6(5):054307, 2019.

[99] M. T. Khuc, L. Mendonca, S. Sharma, X. Solinas, M. Volk, and F. Hache. Measurement of circular dichroism dynamics in a nanosecond temperature-jump experiment. *Rev. Sci. Instrum.*, 82(5):054302, 2011.

# Appendix

## A1 Purification procedure of FK-11-X

FK-11-X was purified by reversed-phase HPLC on a Ultimate 3000 chromatographic system (Thermo Scientific) using a Luna C18(2) column (250 × 4.6 mm, 5 µm, 100 Å, Phenomenex). The separation was performed at 40°C using the following gradient of water + 0.1% formic acid (mobile phase A) and acetonitrile + 0.08% formic acid (mobile phase B) at a flow rate of 1 mL $min^{-1}$: linear increase from 15% B to 32% B within 12 min followed by linear increase to 100% B in 3 min. The peptide purity was checked by LC-MS on an Ultimate 3000 Micro-HPLC system (Thermo Scientific) connected to an ESI-Q-TOF mass spectrometer (Q-STAR Pulsar, AB Sciex) equipped with an IonSpray source. The separation was achieved on a C18 column (Uptisphere® WTF, 5 m, 150 × 1.0 mm, Interchim) using the following gradient of mobile phases A:B at 40°C and 40 µL $min^{-1}$: linear increase from 10% B to 60% B within 30 min followed by linear increase to 100% B in 5 min. The purified FX-11-X was dried under vacuum and conserved at -20°C until use. FX-11-X was dissolved at in phosphate buffer, 70 mM, pH 7. The peptide concentration was determined from absorbance measurements at 365 nm, using the extinction coefficient provided at 367 nm for the dark-adapted azo group, $\epsilon$ = 28 000 $M^{-1}cm^{-1}$.

# A2 Optimized force field parameters

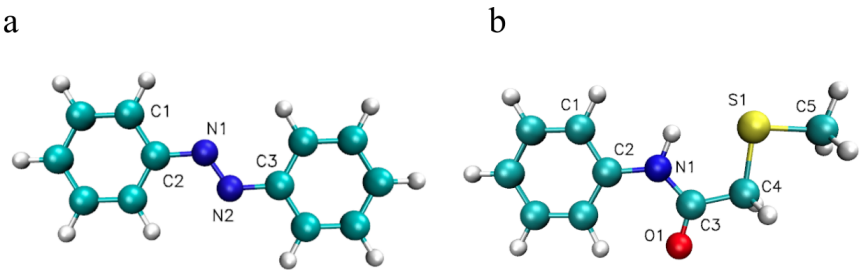


**Figure A2.1: a.** Azobenzene **b.** Structures used for the force field parameter optimisation of the linker between the azobenzene and the peptide.

| **Dihedral angle** | $k$ (kcal/mol) | $n$ | $\delta$ (°) |
|---|---|---|---|
| $C_1C_2N_1N_2$ | 2.5 | 2 | 180 |
| $C_2N_1N_2C_3$ | 23.0 | 2 | 180 |
| **Angle** | $k$ (kcal/mol) | $\theta_0$ (°) | |
| $C_1C_2N_1$ | 50 | 116.5 | |
| $C_2N_1N_2$ | 75 | 106.0 | |
| **Bond** | $k$ (kcal/mol) | $b_0$ (Å) | |
| $C_2N_1$ | 300 | 1.415 | |
| $N_1N_2$ | 500 | 1.295 | |

**Table A2.1:** Optimised force field parameters of the azobenzene (Figure A2.1a.)

| **Dihedral angle** | $k$ (kcal/mol) | $n$ | $\delta$ (°) |
|---|---|---|---|
| $C_1C_2N_1N_2$ | 1.43 | 2 | 180 |
| $C_2N_1N_2C_3$ | 16.70 | 2 | 180 |
| **Angle** | $k$ (kcal/mol) | $\theta_0$ (°) | |
| $C_1C_2N_1$ | 134 | 120.0 | |
| $C_2N_1N_2$ | 155 | 116.5 | |
| **Bond** | $k$ (kcal/mol) | $b_0$ (Å) | |
| $C_2N_1$ | 172 | 1.432 | |
| $N_1N_2$ | 335 | 1.262 | |

**Table A2.2:** Optimised force field parameters of the azobenzene (Figure A2.1a) proposed by Böckmann *et al.*[83].